A novel macroelement to assess the vulnerability of reinforced concrete frame stuctures under severe dynamic loadings

Androniki-Anna Doulgeroglou

▶ **To cite this version:**

Androniki-Anna Doulgeroglou. A novel macroelement to assess the vulnerability of reinforced concrete frame stuctures under severe dynamic loadings. Civil Engineering. École centrale de Nantes, 2022. English. NNT : 2022ECDN0042 . tel-03952840

HAL Id: tel-03952840
https://theses.hal.science/tel-03952840

Submitted on 23 Jan 2023

HAL is a multi-disciplinary open access archive for the deposit and dissemination of scientific research documents, whether they are published or not. The documents may come from teaching and research institutions in France or abroad, or from public or private research centers.

L'archive ouverte pluridisciplinaire **HAL**, est destinée au dépôt et à la diffusion de documents scientifiques de niveau recherche, publiés ou non, émanant des établissements d'enseignement et de recherche français ou étrangers, des laboratoires publics ou privés.

CENTRALE NANTES

THÈSE DE DOCTORAT DE

L'ÉCOLE CENTRALE DE NANTES

ÉCOLE DOCTORALE N° 602
Sciences pour l'Ingénieur
Spécialité : *Génie Civil*

Par
Androniki-Anna DOULGEROGLOU

A novel macroelement to assess the vulnerability of reinforced concrete frame structures under severe dynamic loadings

Thèse présentée et soutenue à l'Ecole Centrale de Nantes, le 13 Octobre 2022
Unité de recherche : UMR 6183, Institut de Recherche en Génie Civil et Mécanique (GeM)

Rapporteurs avant soutenance :

Delphine BRANCHERIE	Professeure des Universités, Université de technologie de Compiègne
Stéphane GRANGE	Professeur des Universités, Institut National des Sciences Appliquées de Lyon

Composition du Jury :

Président :	Claudio TAMAGNINI	Full Professor, Universita degli Studi di Perugia, Italie
Examinateur :	Silvano ERLICHER	Directeur technique, Egis Nucléaire, Groupe EGIS, Montreuil
Dir. de thèse :	Panagiotis KOTRONIS	Professeur des Universités, Ecole Centrale de Nantes
Co-dir. de thèse :	Giulio SCIARRA	Professeur des Universités, Ecole Centrale de Nantes

Invitée :

Catherine BOUILLON	Responsable Recherche et Innovation, Groupe ESSOR, Lons

ACKNOWLEDGEMENTS

I take advantage of this space to express verbally my thankful sentiments, even though words are limited for this purpose, to all the people that believed in me, even more than I did, and supported me during my PhD journey.

Firstly, I would like to express my gratitude to the Supervisors of my PhD. I wish to express my heartfelt thanks to the Director of my thesis, Professor Panagiotis Kotronis for trusting me this project, for his scientific guidance and his support throughout all the difficulties including changing industrial partner of the thesis. I would also like to thank the Co-Director of my thesis, Professor Giulio Sciarra who accompanied my PhD journey with his assistance and his valuable suggestions. A big thanks is dedicated to their kind tolerance during the most stressful periods I passed through during my PhD.

I would like to thank all my colleagues from Groupe Essor, the industrial partner, for their encouragements, but most importantly, I would like to express my deep gratitude to the people who most closely supervised my work, Catherine Bouillon and Yves Jaboin, for their trust, their support throughout all the funding difficulties because of liquidation of the previous industrial partner and their precious advice during all the periods of my PhD. They accompanied me since before the beginning of my PhD and they stood up for me as a family in France. I would also like to thank the industrial partner for providing the funding of my PhD and also a big thanks to Professor Abed Soubra for his help to find funding at the very early beginning of my thesis and for accompanying my supervising team during the first years of my PhD.

I am also thankful for all the members of the jury who accepted to play this role and being present at this very important to me day. I will always remember their kindness and the fruitful discussions that we had during my PhD defense.

Additioanally, I would like to express my gratitude to every researcher who offered me significant scientific support during my PhD without knowing me personally: Doctor Stephen Suryasentana, that generously provided me with useful scientific material during my work. He is an example of researcher who shares his knowledge regardless of any potential profit. I would also like to express my gratitude to Professor Michel Arrigoni who provided me with precious references during the beginning of my PhD. A big thanks to

Doctor Benjamin Richard for the productive scientific discussion we had and to Professor Stathis Bousias for the experimental data that he provided.

To all my colleagues from Ecole Centrale, I would like to express my gratitude, especially to my office colleagues and also to the employees of Ecole Centrale that helped me during my PhD and in particular, the responsibles of the library, the technical support of the Liger and the technical support of GeM laboratory.

I would like to thank all my close friends from France and abroad for their ethical support during all these years. Thank you Kosta, Vassili, Evi, Maria, Renia, Danae, Tonia, Christiana, Pano, Solona, Dora, Luc, Polina, Valentin, Mojtaba, Tijana, Simone, Guillaume, Davide, Timo, Alex and all the ones that would be too many to name. A special thanks is dedicated to Kostas, who appart from a friend was also family for me and I wish to express my deep gratitude for all the scientific discussions we had together and all the helpful advice and tips he provided me since the first moment I met him.

Last but not least, I wish to express my thankful sentiments to my family that regardless of the distance they offered me significant support in every possible way during my PhD.

Table of Contents

Introduction **9**

1 Literature review **13**

1.1 Material behavior . . . 13

1.1.1 Concrete . . . 13

1.1.2 Steel . . . 18

1.2 Structural behavior of RC beams and columns . . . 22

1.2.1 Failure modes . . . 22

1.2.2 Monotonic loading . . . 22

1.2.3 Cyclic loading . . . 24

1.3 Interaction diagrams for combined axial, shear and flexural loads . . . 26

1.4 Modeling approaches for RC beams and columns . . . 28

1.4.1 2D/3D finite elements . . . 29

1.4.2 Beam finite elements . . . 30

1.5 Localization phenomenon . . . 31

1.6 Regularization techniques . . . 33

1.6.1 Crack band approach . . . 34

1.6.2 Non-local methods . . . 34

1.6.3 Higher order Micromorphic continuum theory . . . 35

1.6.4 Kinematically enhanced formulations by discontinuities . . . 36

1.7 Cohesive models . . . 36

2 Interaction diagrams for symmetrically RC square sections **41**

2.1 3D finite element modeling strategy . . . 41

2.1.1 Constitutive model for concrete and steel . . . 41

2.1.2 Experimental campaign chosen for validation of the numerical model 48

2.1.3 Finite element mesh & boundary conditions and load control . . . 49

2.1.4 Material parameters . . . 51

2.1.5 Validation . . . 54

2.2 Characteristic states 60
2.3 Loading program 61
2.4 Interaction diagrams N,M,V 63
2.5 Comparison with Eurocode 66
2.6 Analytical convex expressions 68
2.6.1 Background 68
2.6.2 Analytical expressions at failure (3^d characteristic state) 68
2.6.3 Comparison of the different analytical expressions at failure (3^d characteristic state) 73
2.6.4 Analytical expressions at 2^{nd} characteristic state 75
2.6.5 Analytical expressions at 1^{st} characteristic state 77
2.6.6 Summary of the steps for the calculation of the analytical expressions of the three characteristic states 79
2.7 Summary 81

3 Macroelement modelling 83
3.1 Different types of macroelements 83
3.2 A novel macroelement for RC beam-columns 87
3.2.1 A Timoshenko finite element beam 87
3.2.2 Stress-resultant plasticity model (macroelement) 91
3.3 Parameter identification 95
3.4 Integration algorithm 99
3.5 Adjustment for cyclic loading conditions 102
3.6 Convergence rate 106
3.7 Summary of macroelement parameters 107

4 Modeling up to failure 109
4.1 Introduction 109
4.2 Enhanced formulation 111
4.3 Global cohesive model 116
4.3.1 Activation and behavior 116
4.3.2 Parameter identification 119
4.3.3 Integration algorithm 122

5 Numerical applications **125**
5.1 Case studies . . . 125
5.1.1 RC cantilever columns . . . 125
5.1.2 RC plane frames . . . 138
5.1.3 RC simply supported beam . . . 143
5.2 Conclusions . . . 146

Conclusions and perspectives **149**

Annex **153**
A. Tests S2, S3, S4, S5, S7, S9 . . . 153
B. M1, M2 and M4 sections . . . 160

Bibliography **163**

INTRODUCTION

This thesis has been carried out in collaboration with Ecole Centrale Nantes and Groupe-ESSOR (*thèse CIFRE*) and aims to numerically study the vulnerability of Reinforced Concrete (RC) structures subjected to severe dynamic loads. These loads can be characterized as slow (e.g. earthquake) or fast (e.g. explosion) leading to different types of failure depending on the loading magnitude and direction. In this work only slow dynamic loads are considered.

Only frame (beam-column) systems of symmetrically reinforced sections are studied hereafter and geometrical non-linearity is neglected. The complexity of the problem is strongly increased because of the material behavior. During the last 50 years, significant developments in constitutive description of concrete and steel have led to a more realistic representation of the behavior of civil engineering structures. Numerical simulations are nowadays a powerful tool which allows to conduct numerical experiments and predict the behavior of RC structures. This is essential for the design of a new structure, but also for evaluating the response of an existing one. In particular, the classical Finite Element Method (FEM) and enriched formulations such as the eXtended Finite Element Method (X-FEM), the Embedded Finite Element Method (E-FEM) and the Discrete Element Method (DEM) allow to reproduce different aspects of the response of a composite specimen, structural member or structure i.e. RC structure. At a local scale, crack initiation, propagation and closing, sliding between reinforcing steel and concrete and the increase of the concrete strength due to confinement influence the behavior at global scale resulting in loss of the initial elastic stiffness, hardening (when compression is predominant), softening, inelastic deformations and stiffness recovery. Numerical simulations are constantly gaining ground versus experimental procedures as they are less expensive. Nevertheless, they may exhibit prohibitive calculation times and therefore they are not suitable for common industrial design applications.

The purpose of this thesis is to overcome this drawback, by providing the industrial partner with a simplified, fast, accurate and robust numerical tool exploiting the classical FEM within the continuum mechanics theoretical framework based on a phenomenological approach. For this, a 3D finite element model of a RC structural element is first

built and suitable constitutive laws are adopted. Numerical simulations considering various 3D loading combinations of axial, shear and flexural loads allow to validate the model with experimental results and to deduce the behavior of a RC section in a global scale. Given the constitutive description of the section and considering three characteristic states, interaction diagrams are obtained and a novel macroelement is proposed. In this approach, called macroelement modeling, the global behavior of the composite RC section is "lumped" into a single, integral, constitutive equation linking the evolution of the stress-resultant loads/moments on the sectional gravity center to the corresponding strains histories, by adopting the kinematical assumptions of the Timoshenko beam theory. The proposed macroelement is subsequently implemented in a Timoshenko beam finite element as this permits to significantly reduce the computational cost. Finally, the softening behavior til complete failure is reproduced by coupling the macroelement to a cohesive model, which describes the response in terms of generalized force-generalized displacement jumps, dominated by flexural mode of failure, within the framework of the E-FEM. More specifically, the structure of the manuscript is the following:

In Chapter 1, the main aspects of the behavior of concrete and steel and of RC beam-column member are explained. A literature review regarding the methods for the construction of interaction diagrams is presented and different numerical modeling approaches for RC beam-columns are outlined. Localization phenomenon is described and the most common remedies for the mesh-dependency problem due to localization are cited.

In Chapter 2, suitable 3D constitutive models for concrete and steel are chosen and the behavior of RC cantilever - type columns is numerically reproduced. The proposed modeling strategy is validated using experimental results. Interaction diagrams are then numerically derived considering different reinforcement ratios and original analytical convex expressions are proposed. Finally, a comparison with existing interaction diagrams from the literature is performed.

In Chapter 3, the macroelement concept is introduced and a global stress-resultant model is built within the plasticity framework. The Full Linear Independent (FLI) Timoshenko beam finite element is described and the integration algorithm of the global constitutive model (i.e. macroelement) is detailed. Modifications on the original constitutive description are proposed for cyclic loading with or without change of sign. The novel macroelement for RC beam-columns is implemented in the research finite element code GemLab (based on Matlab) of Ecole Centrale Nantes. Numerical aspects of the

convergence procedure are finally discussed.

In Chapter 4, the enriched finite element formulation is presented for the FLI Timoshenko beam. The macroelement is coupled to the global cohesive model. The implementation procedure is provided and the necessary adjustments to capture the cyclic behavior are adduced.

Case studies are finally presented in Chapter 5 as well as comparisons with experimental results in order to validate the numerical implementation and to illustrate the performance of the novel macroelement coupled to the global cohesive model. The case studies concern static monotonic and cyclic loads (constant or alternate sign) and dynamic loading (earthquake). Simulations are presented till the complete failure of the structure.

Chapter 1

Literature review

As the purpose of this thesis is the development of a simplified numerical tool that takes into account multiaxial loading conditions and the dynamic nature of loads by exploiting the Finite Element Method (FEM) based on a phenomenological approach within the continuum mechanics theory, this Chapter begins by introducing the main aspects of the behavior of concrete and steel at a Representative Elementary Volume (REV) scale. Subsequently, the behavior at a structural level of a RC member is given, as it results from the description of the behavior of the different ingredients by which it is composed (concrete and steel). To consider mutliaxial loading conditions, a literature review regarding the methods for the construction of interaction diagrams is presented as well as several approaches for the modeling of RC beam-columns. Localization phenomenon is explained as it is appears at the defective material points due to high level of loadings. Finally, when numerical methods are employed, localization results in pathological mesh-dependency and the most common approaches to remedy this problem are presented.

1.1 Material behavior

1.1.1 Concrete

Concrete is composed by a number of components such as cement, aggregates, water, admixtures, the proportion of which is responsible for its mechanical properties. In particular, even before submitted to any load, there exist numerous microcracks between coarser aggregates and mortar resulting from the incompatibility of their elastic moduli. Concrete exhibits a strong asymmetry between monotonic uniaxial traction and uniaxial compression; its resistance in tension is about 10%-15% of the resistance in compression. This property is attributed to the weakest links of its composition, the aggregate-mortar interfaces, which present significantly lower tensile strength than mortar (Chen 2007).

The response in compression is ductile, while in tension concrete shows a fragile be-

havior and the post-peak behavior presents softening. This can be explained by the different cracking patterns presented at the damaged material. Specifically, during tension, micro-cracks develop, the coalescence of which results in localized cracking. The above mentioned behavior of concrete under tension was experimentally investigated in some early studied among which those of Hughes and Chapman 1966, Terrien 1980 and Petersson 1981 can be cited.

On the other hand, under compression, for low stresses up to 30% of concrete compressive strength, the existing cracks before loading do not show considerable evolution and the behavior of concrete in a REV is characterized as elastic (Kotsovos and Newman 1977). Diffuse cracking is observed after this stage and mortar cracks start to bridge together. When concrete reaches the 70% of its strength, a network of interconnected micro-cracks develops resulting in the form of macro-cracks until material failure. After reaching its maximum strength, concrete behavior presents softening, a significant reduction of its elastic modulus and inelastic deformations. Experimental investigation that gave light to these observations can be found in representative works of Hsu et al. 1963 Benouniche 1979 and Ramtani 1990.

First experimental investigations dating since the beginning of 20^{th} century have been conducted to deduce the behavior of concrete under the following biaxial stress combinations: biaxial compression (Föppl 1899, Wästlund 1937 Kupfer and Gerstle 1973), compression-tension (Bresler and Pister 1958, McHenry and Karni 1958, Kupfer and Gerstle 1973) and biaxial tension (Kupfer and Gerstle 1973). Under different biaxial stress combinations, different failure modes are observed (Figure 1.1) and the ultimate strength (peak stress) varies according to the load combination, as shown in Figure 1.2. In biaxial compression, the ultimate concrete strength is higher that under uniaxial compression, increased up to 25% (Chen 2007). In biaxial tension, the ultimate strength is equal to the one under uniaxial tension.

Another important aspect is the volumetric behavior of concrete during uniaxial and biaxial compression. For low levels of stress up to 30% of concrete strength, concrete experiences volume reduction and the volumetric strain is proportional to the applied stress. For higher levels of stress, the rate of the volume reduction increases until a point of inflection, at which the direction of the volume change is reversed resulting in an inelastic volumetric expansion (dilatancy). This point of inflection corresponds to 75% of the concrete strength (for uniaxial compression) and is denoted as critical stress (Figure 1.3). This phenomenon is due to progressive growth of major microcracks in concrete.

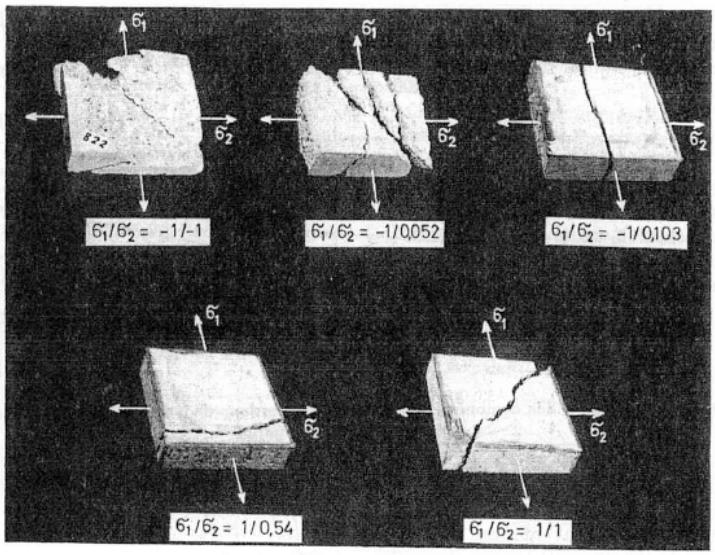

Figure 1.1: Failure modes of specimens subjected to biaxial stresses (Kupfer and Gerstle 1973).

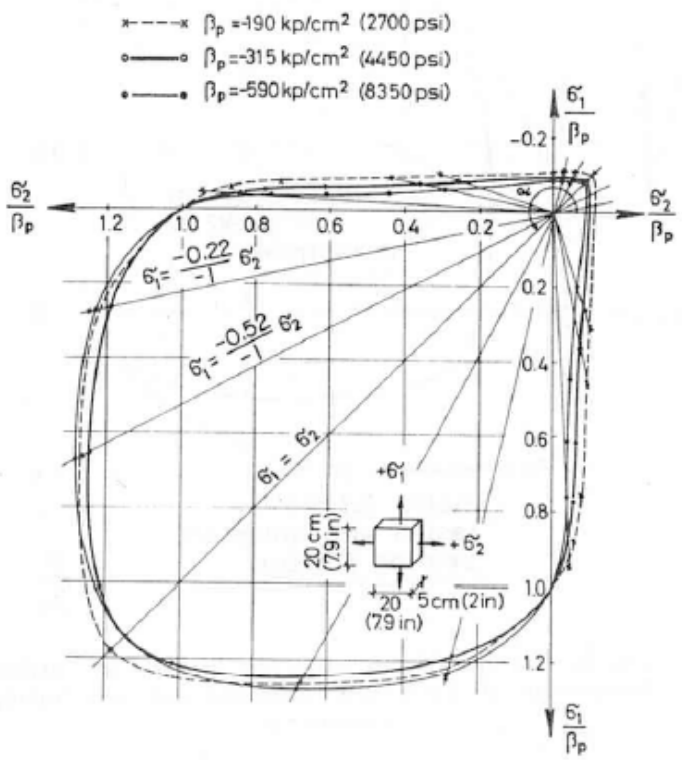

Figure 1.2: Biaxial strength of concrete: results of experimental investigation (Kupfer and Gerstle 1973).

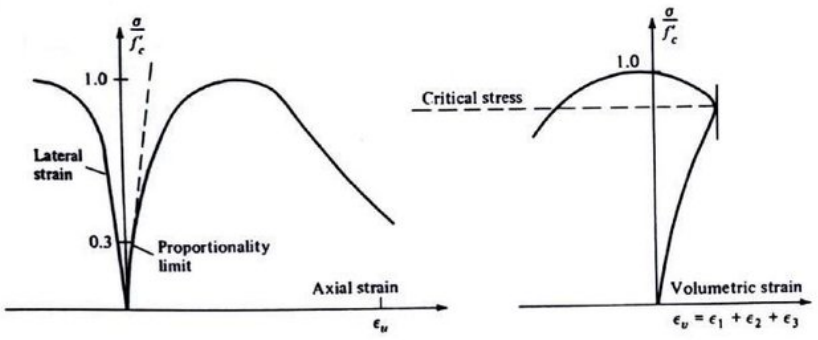

Figure 1.3: Concrete behavior during compression (Chen 2007).

Under triaxial loading conditions, concrete presents different behavior depending on the confining stress level; quasi-brittle, hardening or softening as it has been reported in the experimental findings of Richart et al. 1928, Kotsovos and Newman 1977, Imran and Pantazopoulou 1996, Li and Ansari 1999. Under high confining stresses, the failure mode switches from cracking to crushing of the cement paste. Generally, increasing the confining pressure results to the increase of the axial strength as it is shown in Figure 1.4.

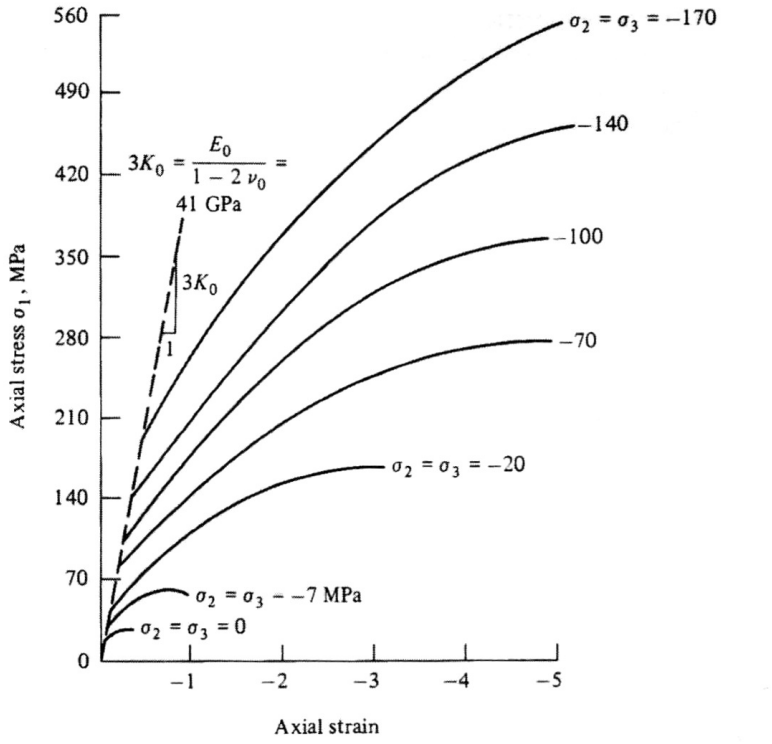

Figure 1.4: Triaxial stress-strain relationship for concrete (Balmer 1949).

The behavior of concrete under alternate cyclic loading (change of loading sign) has been studied by Ramtani 1990 and is presented in Figure 1.5. During tension and when the elastic limit is achieved, the concrete is damaged and during unloading permanent inelastic strains are observed. Switching from tension to compression, the so-called unilateral effect takes place; a full recovery of the elastic undamaged stiffness happens progressively, as the cracks close. With further loading during compression, concrete undergoes damage due to microcracking, strain hardening and then softening. If unloading appears during compression, cracks reopen. During cycling loading, hysteretic loops are also observed, due to the local friction (sliding mechanism) occurring between the crack lips.

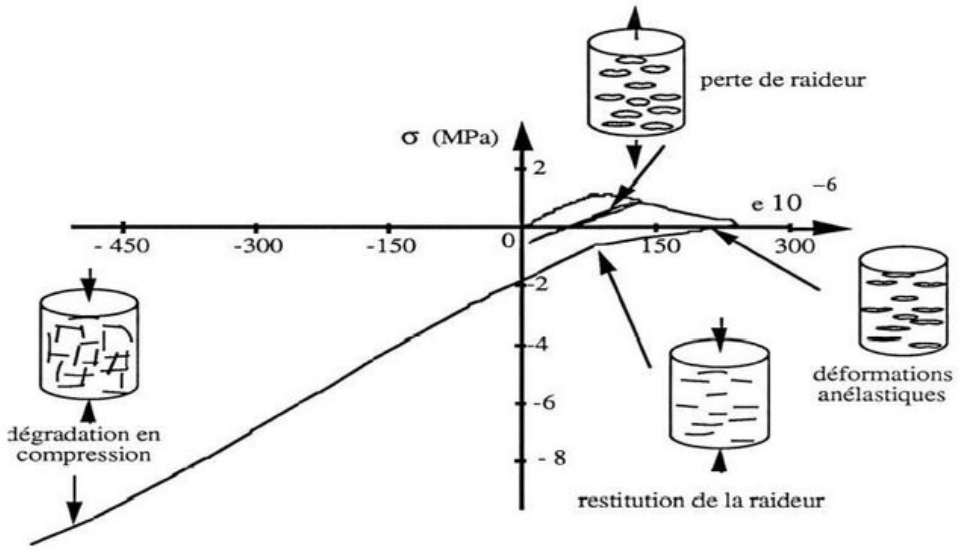

Figure 1.5: Uniaxial concrete behavior under cyclic loading (Ramtani 1990).

In fast dynamic loading conditions, concrete behavior is controlled by the loading rate. The strain rate effect results in the increase of concrete strength, both in compression and tension as shown in Figure 1.6 and Figure 1.7 respectively, by which it is concluded that the dynamic increase of concrete strength is more rate-sensitive in tension than in compression. The strain rate dependence is more intense for concretes with lower strengths (Daudeville and Malécot 2011).

The influence of the parameters ratio water/cement (W/C), boundary conditions and presence of free water on the strain rate effect has been studied (Rossi et al. 1994, Bischoff and Perry 1995, Gopalaratnam et al. 1996) and W/C and boundary conditions are characterized as secondary parameters with an insignificant impact. The presence of free water is the key factor for the increase of the ductility of concrete (Rouquand et al. 2007). This

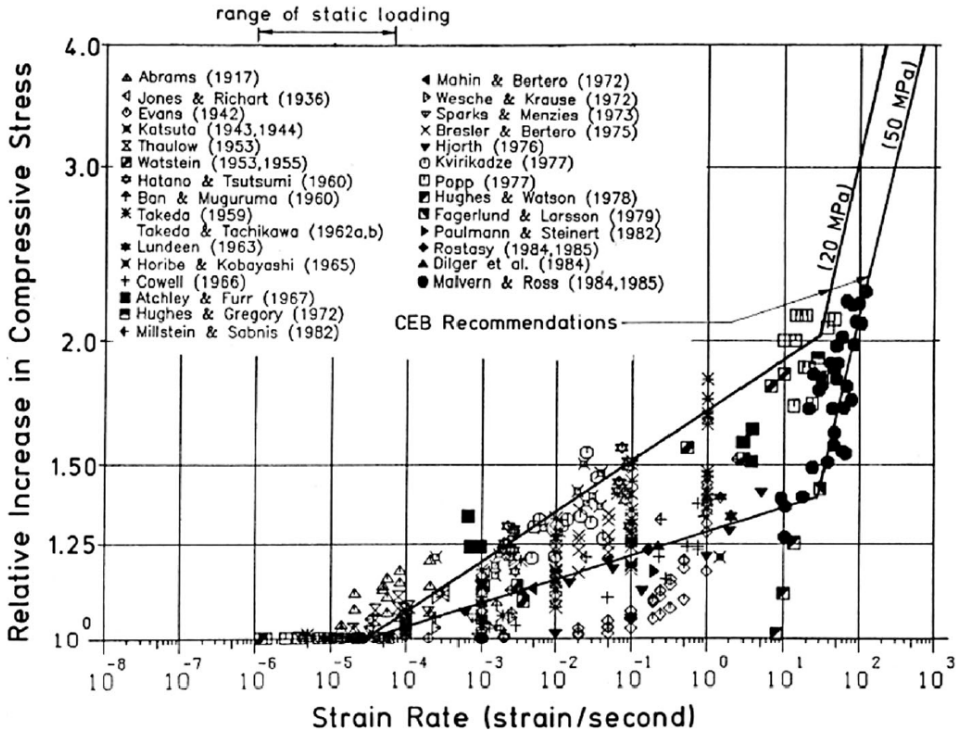

Figure 1.6: Increase of concrete strength in uniaxial compression under dynamic loads (Bischoff and Perry 1991).

can be explained by the fact that concrete has an open porous structure, composed by the solid part and the voids that can be empty, full or partially filled of water. For high dynamic loads, the time scale is very low (few milliseconds or less) so the water has no time to move inside the material and therefore undrained conditions can be considered.

1.1.2 Steel

Steel belongs to the category of ductile materials. At early stages of loading its behavior is linear elastic. At higher levels of loading, inelastic deformation typically happens by plastic slip along crystallographic planes. Thus, plastic deformation is mainly a sequence of permanent shear strains and plastic change of volume may be neglected together with the effect of hydrostatic pressure (the behavior is independent of the invariant $I1$). As a consequence, yielding of steel is due to shear stresses and is governed by the second invariant of the deviatoric stress tensor ($J2$). The above conclusions are based on very early experiments on yielding of metals, conducted by many researchers such as Ros and Eichinger 1929, Lessells and MacGregor 1940, Davis 1945, Marin and Hu 1956 and Maxey

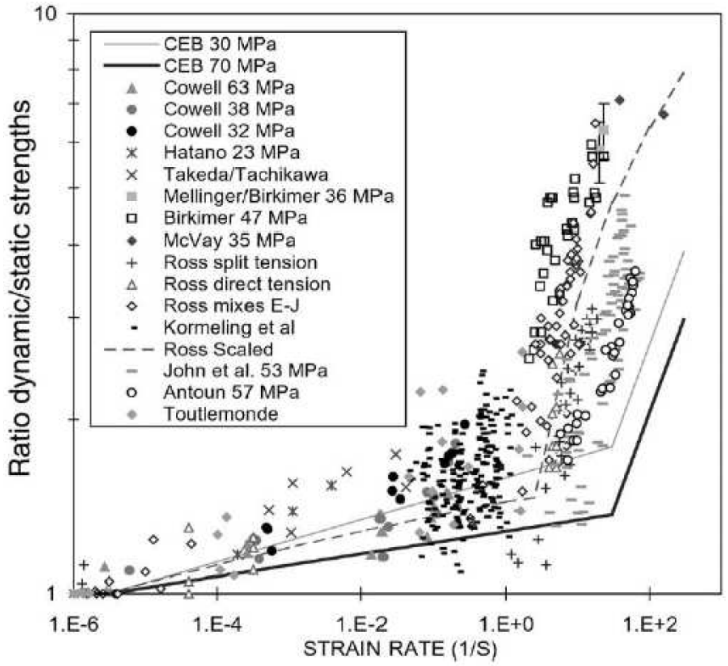

Figure 1.7: Increase of concrete strength in uniaxial tension under dynamic loads (Malvar, Ross, et al. 1998).

1986, following the work of Tresca 1864 and on more recent works (see for example Chen et al. 2012).

As a structural component of RC members, longitudinal steel bars and transverse stirrups are conceived to mainly sustain axial loads. During monotonic loading, the behavior is initially linear elastic until the yield point, after which the response is represented by a yielding plateau, followed by a hardening part til the maximum strength and a post-peak response characterized by softening till rupture (see Figure 2.4a).

Steel presents a symmetrical response under tension and compression. However, according to geometrical properties of the steel (slenderness of the rebars) buckling can occur under compression and thus the behavior of the reinforcing steel rebars is no longer symmetrical under tension and compression, as it can be observed in Figure 1.10. Buckling is prevented during the design of RC structures by sufficient amount and distribution of transversal hoops. Thus, in the constitutive description of the steel rebars of the numerical model built in Chapter 2, its behavior is assumed symmetrical in tension and compression.

Under cyclic loading conditions, after reaching its elastic limit, plastic deformations are developed and steel experiences increase of the yield strength in the direction of plastic

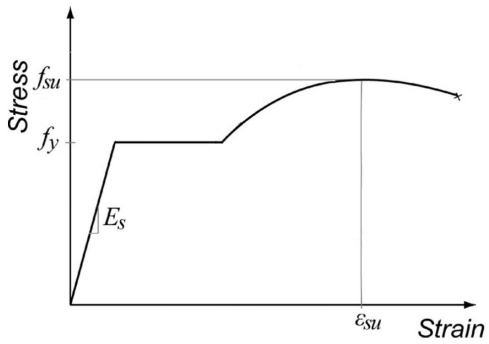

(a) Uniaxial steel behavior under monotonic loading. Modified Figure: its original version is found in Kunnath et al. 2009

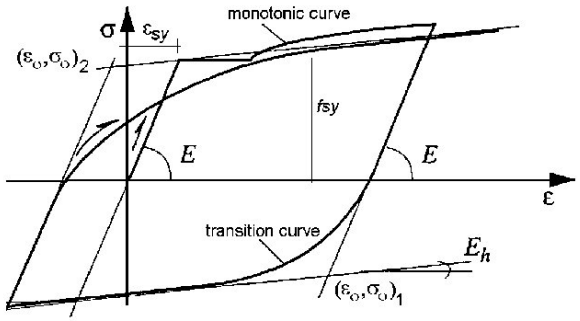

(b) Uniaxial steel behavior under cyclic loading (Menegotto and Pinto 1973)

Figure 1.8: Uniaxial steel behavior under (a) monotonic and (b) cyclic loading.

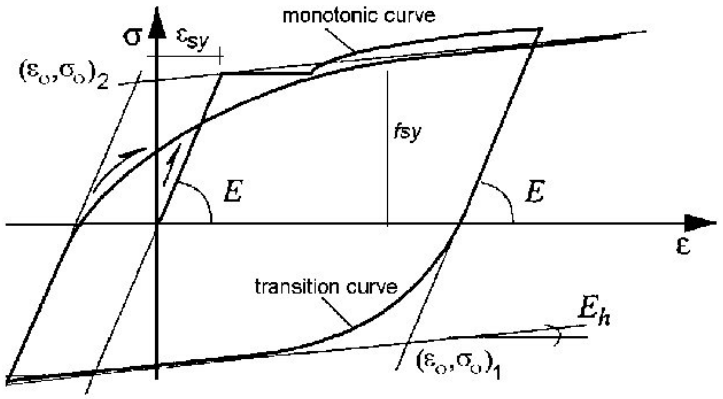

Figure 1.9: Uniaxial steel behavior under cyclic loading (Menegotto and Pinto 1973).

flow and decrease of the yield strength in the opposite direction. This phenomenon is known as the Bauschinger effect (Bauschinger 1879). The basic mechanism responsible for the Bauschinger effect is related to the dislocation structure in a cold-worked metal and to a particular kind of residual stresses that form on the grain boundaries of polycrystals and assist the movement of dislocations in the reverse direction (Borja 2013). As in many metals it is experimentally observed that in the stress space, the center of the yield surface moves as a rigid body (without significant expansion) in the direction of the plastic flow depending on the loading history. This property is described by a kinematic hardening rule. Kinematic hardening leads to a translation of the loading surface i.e. a shift of the origin of the initial yield surface. Figure 2.4b shows the typical uniaxial behavior of steel

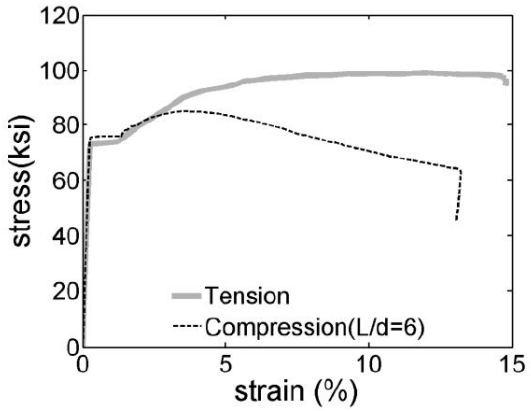

Figure 1.10: Monotonic response in tension and compression of reinforcing steel for an aspect ratio of $L/d = 6$ (Heo et al. 2009).

under cyclic alternate loading. The behavior during unloading stages is elastic.

Under fast dynamic excitations, steel exhibits show low strain rate dependency (see for example Figure 1.11) and thus the strain rate effect can be neglected.

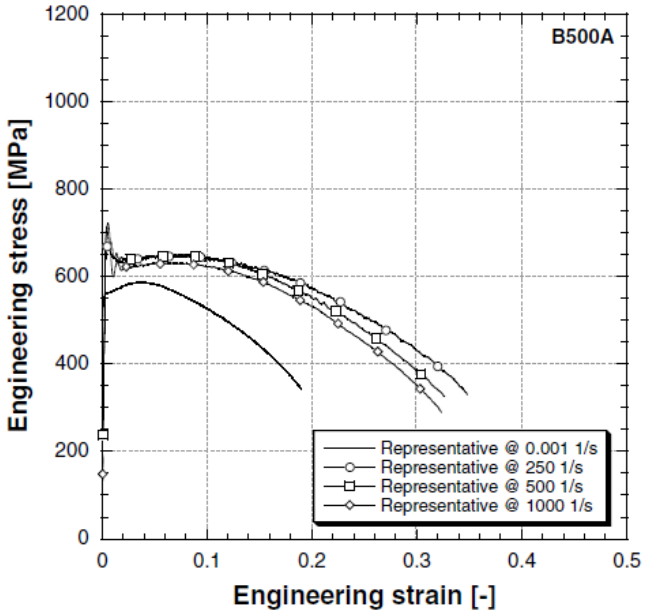

Figure 1.11: Mechanical properties trend versus strain-rate for B500A reinforcing steel bars of $12mm$ diameter (Cadoni and Forni 2015).

The above aspects that characterize concrete and steel behavior are taken into consideration for the constitutive description of the materials in the numerical model presented in Chapter 2, built to deduce the gloabal behavior of RC sections within the framework

of slow dynamics.

1.2 Structural behavior of RC beams and columns

The different failure modes of RC beams and columns and the phenomena that take place under monotonic and cyclic loading are analyzed hereafter.

1.2.1 Failure modes

RC beams and columns present two principal modes of failure: flexural and shear. The former describes a failure during which:

- flexural loads are higher than the flexural strength of the element and
- the shear capacity of the element is more significant than the flexural,

while the latter represents a failure during which:

- shear loads are higher than the shear capacity of the element and
- the flexural capacity of the element exceeds the shear.

For RC beam and column elements without shear reinforcement the shear failure mechanism is expressed by sliding along a crack in the beam, while for RC elements with shear reinforcement by yielding of the transverse reinforcement. In general, flexural failure is preferred than shear failure, as the latter is more abrupt and brittle. However, for over-reinforced elements flexural failure may occur due to concrete crushing at the compression layer of the section and this failure is also brittle.

1.2.2 Monotonic loading

RC beams are mainly designed to resist flexural loads. Under monotonic loading, their response can be divided in the following phases (Figure 1.12):

- linear elastic behavior until concrete cracking: the behavior is reversible until the first concrete layer of the beam section under tension reaches its tensile strength (point P1).

- nonlinear hardening behavior until the peak response: a reduction of the stiffness takes place and the response exhibits irreversible behavior due to two different types of hardening: structural and material. The former is related to the dimensions and the shape of the beam section. Successive layers along the height of the section reach their tensile limit during the structural hardening. The latter is related to the material behavior. During this loading phase, two characteristic points can be identified: yielding of the longitudinal steel (point P2) and peak of the response (point P3) corresponding to the ultimate beam strength. Between these two points, stiffness degradation is significant. Point P3 corresponds to either concrete crushing due compression or to the point where steel rebars reach their ultimate strength. Until the point P3, it is considered that nonlinearities tend to localize at specific parts of the beam and form the plastic hinges.

- nonlinear softening behavior until failure: at this stage, after the peak, the stresses are constantly reduced until zero inside the plastic hinges. The beam has no capacity to resist further loading and is driven to complete failure. In Figure 1.12, the continuous line corresponds to a brittle behavior, while the dotted line to a more ductile post-peak behavior.

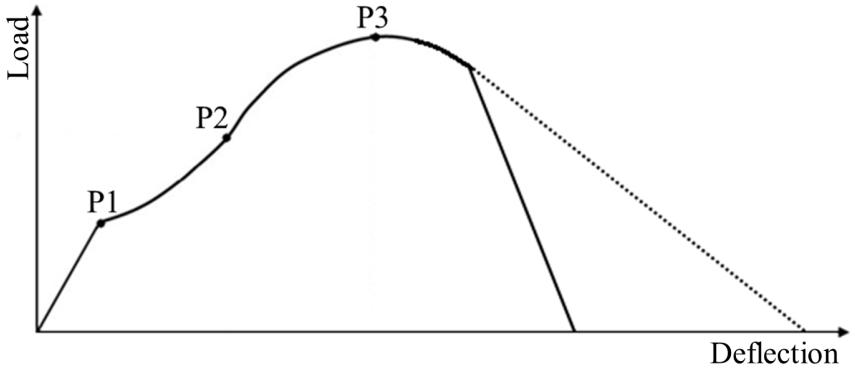

Figure 1.12: Typical load-deflection relationship for reinforced concrete elements.

RC columns are designed to resist higher levels of axial compressive loads (due to the dead loads of the structure). The (static) axial loads being however often lower than the ultimate axial load of the columns, results to an increase the flexural and shear capacities of the element and provides greater ductility due to the concrete confinement inside the ties which introduces a triaxial compression stress state.

Shear forces act perpendicular to the longitudinal axis of the structural element and their magnitude is higher at the supports. They are dominant in squat elements leading to brittle type of failure. Both RC beams and columns are designed to resist shear forces and their shear capacity is a combination of the strength of the concrete and the strength provided by the transverse reinforcement.

1.2.3 Cyclic loading

In Figure 1.13, a typical shear force-column tip displacement response is presented for a RC column subjected to transversal alternate displacements under a constant axial load. It can be observed that the response exhibits hysteresis loops during every inelastic cycle related to the path-dependence of the structure's restoring force versus displacement. These curves delimit a surface whose area is proportional to the amount of energy dissipated per cycle.

Another important aspect of the response during alternate loads is the pinching effect. The term describes the shapes of hysteresis loops that tend to be pinched in the middle. In other words, pinching is the stiffness degradation of the hysteretic curves during the loading and unloading cycles and it is mainly due to the bond slippage between steel and concrete, the opening and closing of cracks and the shear locking mechanism.

During alternate loading and after a certain number of cycles, concrete cover spalling may occur. The concrete core inside the ties laterally expands and can be significantly damaged. In RC columns, the longitudinal steel bars are submitted to combined axial and bending loads and they can buckle. In terms of the RC member response, this is identified as a sudden and progressive decrease in its load-bearing capacity. Buckling mainly depends on the slenderness of the rebars (ratio between the length over the diameter) but also on the stiffness and the rigidity of the hoops and the strain hardening of steel. Early buckling between two consecutive ties can be avoided with suitable arrangement of the longitudinal and transverse reinforcement at the expected plastic hinges of the member.

Dynamic excitations

When a RC structure is subjected to dynamic loadings, its response is time-dependent. There arise two types of additional forces that must be taken into account in the equilibrium of the structure: the inertia forces that resist the mass acceleration and the damping (or dissipative) forces which are proportional to velocity. The former are more significant

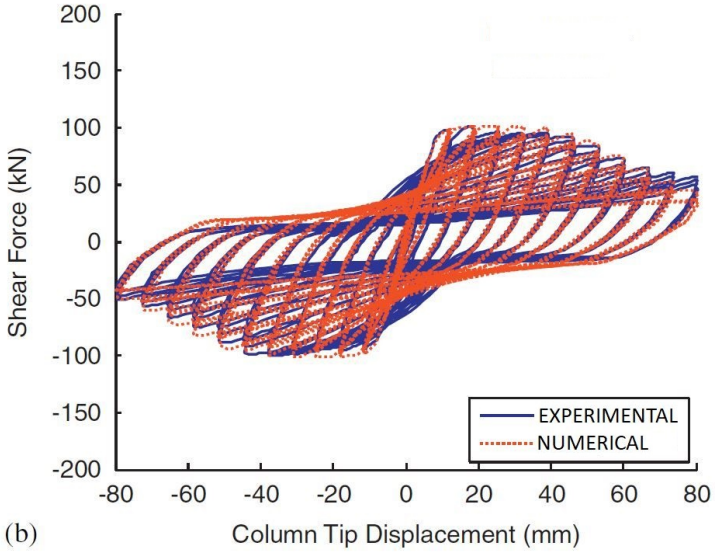

Figure 1.13: Shear force-column tip displacement: cyclic response (Xu and Zhang 2011). The experimental results are taken from Sakai and Kawashima 2000.

than the latter.

As far as the material behavior is concerned, in case of an earthquake, the strain rate is in the range that does not influence concrete and steel constitutive description (see Figure 1.14). Therefore, the material time-dependency is judged inconsiderable.

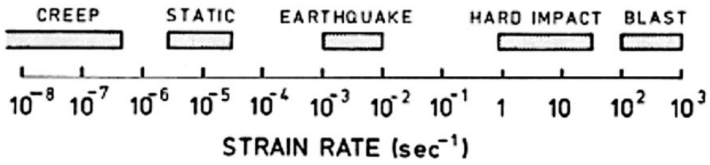

Figure 1.14: Typical strain rates for various types of loading (Bischoff and Perry 1991).

As far as numerical aspects are concerned, for the case of the earthquake, the excitation lasts some seconds which demands a fine time discretization. For this reason, the nature of the dynamic loadings leads to highly increased computational time.

The above principal features that RC structures exhibit during monotonic and cyclic loadings are taken into consideration for the construction of a stress-resultant model (macroelement), concieved for typical RC slender beams and columns, dominated by flexion, in Chapter 3.

1.3 Interaction diagrams for combined axial, shear and flexural loads

Interaction diagrams are functions that define the acceptable combinations of generalized forces' components (i.e. moment, shear force and axial force) of a structural member. Of particular interest in RC design, they are often constructed using limit analysis. To characterize the combination of axial force and bending moment limit states, a suitable set of admissible loading is identified for a given RC member and a convex hull is constructed adopting the so-called lower bound approach in Eurocode 2, CEN 2004. More specifically, steel is described by an elastic perfectly plastic constitutive law, symmetric in traction and compression, while concrete has zero tension resistance and follows a parabolic curve in compression. A rectangular distribution of the normal stress is assumed, multiplied by a correction factor. Eurocode 2 (CEN 2004) provides also interaction diagrams for biaxial bending and axial loading and for shear force and torsion but not for axial force, shear force and bending moment.

In the framework of limit analysis, the upper bound approach is also frequently used which provides an upper bound of a combination of the limit loading, see e.g. (Salençon 1983). The definition of limit loading in this case is based on a global energetic criterion which compares the power dissipated along a plastic process to the power of external forces. It is typically used introducing kinematically admissible velocity fields exhibiting a jump through the body which is therefore separated into two blocks having a relative motion one with respect to the other. If a kinematic admissible mechanism can be found for which the work of the external loads exceeds the dissipated power, then the structure collapses and the load computed on the basis of the assumed mechanism is greater than or equal to the true failure load. The limit load is determined by searching for the least upper bound for loads inducing collapse. In the literature, this method is used to study failure of beams and plates. Kœchlin 2007 introduced a global failure criterion for RC beams considering coupled loading of axial force and bending moment. Concrete is considered zero tension resistant, but with a compressive strength limit, while steel has the same resistance in tension and compression. This criterion was extended to plates by accounting for combination of membrane forces and bending moments. In a subsequent work, Koechlin et al. 2008 derived a failure criterion for beams submitted to a combination of axial force, shear force and bending moment. A 3D criterion is used for concrete (Drucker-Prager) and the behavior of steel is again assumed the same in tension

and compression. The criterion is extended to plates, where numerical solving is however required.

It is also possible to construct interaction diagrams by numerical methods or combining analytical and numerical methods. Elachachi 1992 used a multi-fiber beam finite element model to reproduce the bending moment - axial force interaction diagram for a reinforced concrete structure (for zero shear force), showed the influence of the shear force and constructed the moment - shear force diagram for zero axial force.

Vecchio and Collins 1988 combined analytical and numerical approaches. The analytical framework is based on the Modified Compression Field Theory (MCFT), formulated for in-plane stress conditions (Vecchio and Collins 1986) that relates average stress to average strains in a cracked RC element, satisfying compatibility and equilibrium requirements. The beam section is numerically reproduced with a layered model. Using iterative methods where the longitudinal strains and the shear stresses are updated until the section equilibrium is satisfied the authors present interaction diagrams for shear force and bending moment for different axial loads and interaction diagrams for shear force and axial force.

Rahal 2000a proposed a simplification of the MCFT assuming a parabolic stress-strain relationship for concrete in compression and provided a graphical method to compute the ultimate shear strength of members, which depends on the amount of transverse and longitudinal reinforcement and the concrete strength. In a subsequent work Rahal 2000b, the author extended the method to beams under combined shear, bending and axial load, by assuming that the longitudinal reinforcement required to resist bending moment and axial load can be superimposed on that required for shear.

Nguyen 2019 constructed interaction diagrams for the following loading combinations: bending moment and torsion, bending moment and shear force, coupled shear force - bending moment - torsion. The author developed a 3D multi-fiber beam element that takes into account warping. The cross-section is divided into three zones (named 1D, 2D and 3D) according to the direction of transversal reinforcement and the stress state. These zones are presented in Figure 1.15. The constitutive model of the 1D zone is a uniaxial bilinear elasto-plastic stress-strain relationship, the behavior of the RC section in the 2D zone is described within the MCFT and an extension of the MCFT is adopted in the 3D zone.

Carpinteri et al. 2012 studied the influence of size scale effects on the moment - axial force interaction diagrams using a numerical step-by-step approach based on the inte-

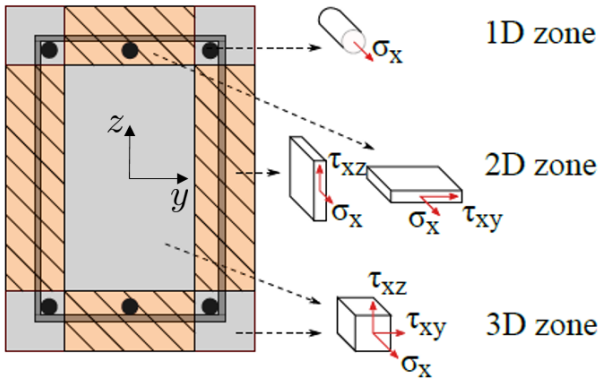

Figure 1.15: Discretization of cross-section following the material stress state in the model of Gregori et al. 2007 (figure from Nguyen 2019).

grated Cohesive/Overlapping Crack Model. Constitutive modeling of concrete is different in compression (Overlapping Crack Model with fictitious interpenetration) and tension (Cohesive Crack Model with fictitious crack) and is described within the nonlinear fracture mechanics framework. Stress-displacement relationships are adopted for the post-peak behavior to avoid scale dependency. Bond slip is taken into account and concrete confinement is considered in the crushing energy expression as a function of the yield strength and the volumetric content of the stirrups.

In this thesis, an exclusively numerical approach, based on the classical finite element method, is adopted for the construction of 3D interaction diagrams (in terms of generalized forces: axial force, bending moment and shear force) in Chapter 2. This approach takes into account an accurate 3D constitutive description of concrete and steel materials and their exact geometrical representation.

1.4 Modeling approaches for RC beams and columns

In order to evaluate the nonlinear response of RC beams, RC columns (or RC frame structures) up to failure, 2D/3D or beam finite elements are often employed. This method includes two main approaches; the classical (2D/3D finite elements) and the simplified approach (beam finite elements). An illustrative example of a 2D multi-story frame modeled by the classical (3D finite elements) and the simplified approach is presented in Figure 1.16.

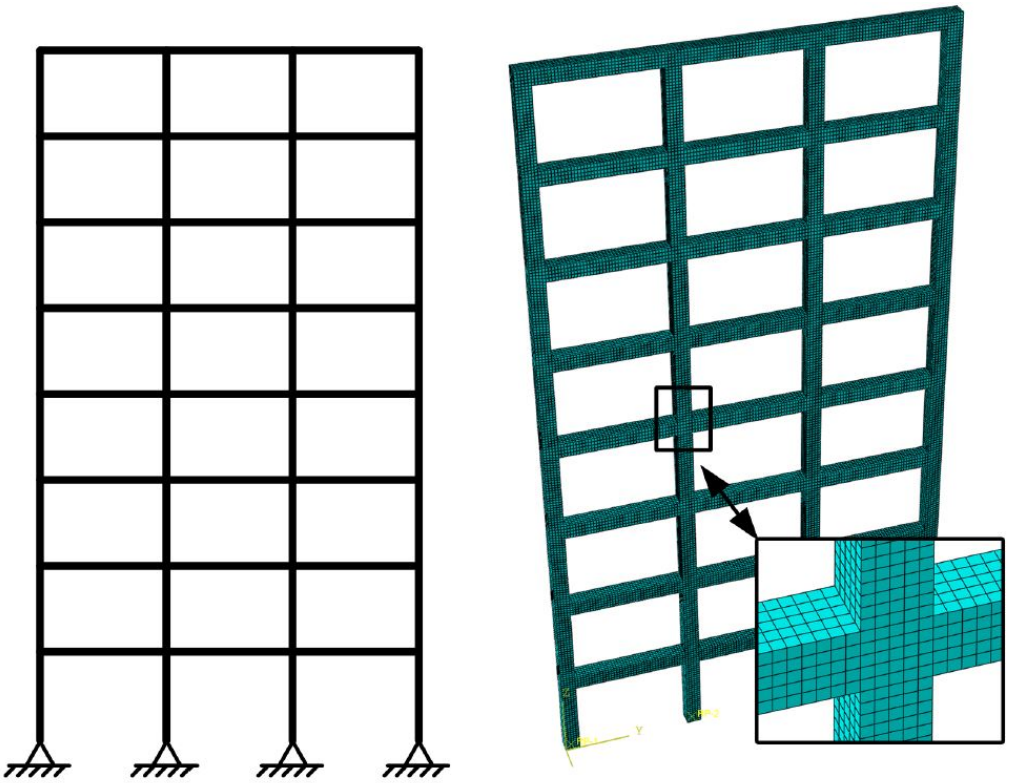

Figure 1.16: 2D frame composed of: beam elements (left) and 3D finite elements (right) (Mai et al. 2020).

1.4.1 2D/3D finite elements

2D and especially 3D finite elements combined with the appropriate constitutive models allow to reproduce the different aspects of the response of a RC structure in the most accurate way. One can thus represent the exact dimensions of the structure, the different materials (concrete, longitudinal and transversal reinforcing steel) and their exact spatial distribution. The 3D nonlinear behavior of the materials can be taken into account including phenomena such as crack initiation in concrete, yielding of the reinforcement steel bars and sliding between concrete and steel.

This approach adopts local constitutive models that describe the material behavior in terms of stresses and strains. Being a quasi-brittle material, concrete is often described using a damage mechanics framework or a combination of damage mechanics and elasto-plasticity. Being a ductile material, steel is almost always described by an elasto-plastic constitutive model. In this way 1D, 2D and 3D phenomena under monotonic and cyclic loading can be reproduced. Furthermore, complex indirect phenomena such as the con-

finement of concrete inside the stirrups can be also taken into account.

Unfortunately, the 3D finite element approach often leads to prohibitive computational costs and necessitates highly qualified engineers to prepare the finite element model and to do the post-processing of the results. Alternative modeling strategies are therefore necessary for practitioners.

However, as the classical 3D finite element approach is judged as the most accurate numerical modeling approach, in Chapter 2, numerical simulations are conducted with this method in order to deduce the 3D sectional behavior of RC beams-columns.

1.4.2 Beam finite elements

Alternatively, simplified approaches, which are by no means simplistic, can be exploited to reduce the computational cost, while maintaining a sufficient accuracy of the numerical calculations. Beam finite elements adopt kinematic assumptions to reduce the degrees of freedom and subsequently the computational cost. The Euler-Bernoulli beam considers that the cross-section of the beam is infinitely rigid in its own plane and perpendicular to the deformed axis of the beam, while the Timoshenko beam considers that the cross-section of the beam remains again plane but not necessarily perpendicular to the deformed axis of the beam (see Figure 1.17).

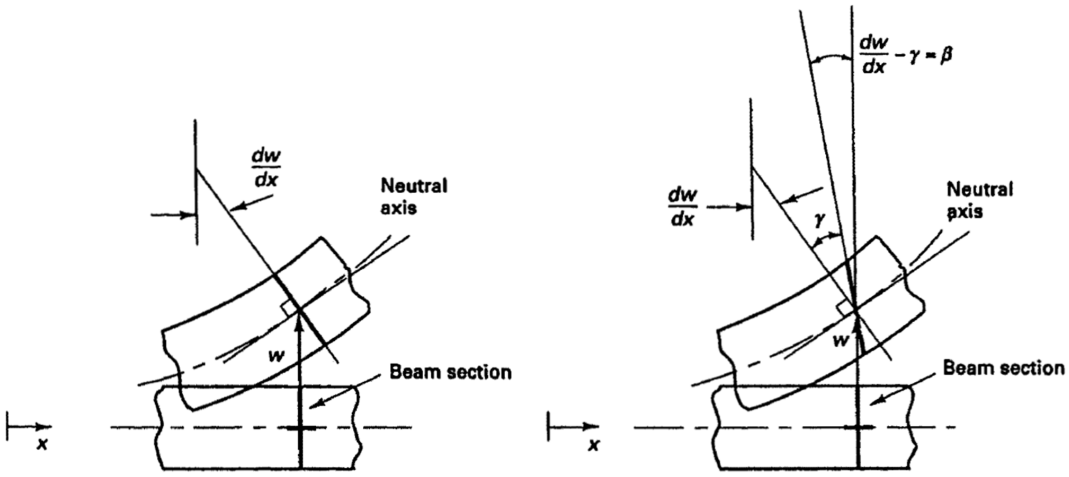

Figure 1.17: Kinematic assumptions for (a) Euler-Bernoulli and (b) Timoshenko beam (Bathe 2006).

Two choices are often made to model the cross-section, the generalized approach (global scale) and the multi-fiber approach (semi-global, local scale) described briefly hereafter:

Generalized approach

The generalized approach considers that a unique material is assigned to the RC section. Global constitutive laws (or stress-resultant models) describe therefore the behavior having the form of generalized forces-generalized strains. The main drawback of this method is that the global behavior of the section is not known. Therefore, the geleralized approach is rarely used together with beam finite elements to simulate the response of RC frame structures. There can be found some recent works though, at which the above mentioned method is used, such as those of Pham et al. 2010, Pham et al. 2013, Jukić et al. 2013, Bui et al. 2014 and Bitar et al. 2018b.

Nevertheless, this approach is adopted hereafter (Chapters 3-5) in this manuscript as it presents two main advantages; fast calculation speed and the possibility to represent the behavior until failure when coupled with strong discontinuities.

Multi-fiber approach

The multi-fiber approach considers the division of the beam section into fibers, the behavior of which can be separately modeled by local constitutive laws, in terms of stress-strain (Scordelis 1984). This method has been also implemented in the finite element code Cast3M (Cast3M 2019) for Timoshenko beams (Guedes et al. 1994). Spacone et al. 1996a developed a multi-fiber Euler-Bernoulli beam and presented numerical applications in Spacone et al. 1996b. A numerous works that adopt the multi-fiber approach for the representation of RC structural behavior can be found, among which those of Kotronis and Mazars 2005, Mazars et al. 2006, Grange et al. 2009b, Grange et al. 2011, Desprez et al. 2013, Desprez et al. 2015 and Bitar et al. 2019.

A brief (qualitative) comparison of the above mentioned approaches concerning the modeling of beam sections is presented in the following Table 1.1.

1.5 Localization phenomenon

Modeling of RC structures until failure requires the consideration of the behavior of each material component: concrete and steel. As already stated in Section 1.1.1, concrete presents asymmetric behavior during tensile and compressive loads and is characterized as a quasibrittle material. Under tension, the response of the concrete is brittle and this is due to a macroscopic stress-free crack (perpendiular to the loading direction) arising

Table 1.1: Generalized vs. multi-fiber approach

	Generalized	Multi-fiber
Global behavior	+	-
Local behavior	-	+
Simplicity	++	+
Speed of calculation	++	+
Parameter's calibration	-	+
Arbitrary sections	+	+
Choice of constitutive models	-	+

from the coalescence of the development of micro-cracks. The response after cracking presents strain softening. During compression the response is more ductile. After the linear elastic phase, concrete presents strain hardening and afterwards strain softening. The mechanism resulting to this beahvior is the diffused micro-cracking, which is parallel to the loading direction. When subjected to high levels of loading, in both cases (tension and compression) the behavior is characterized by strain and damage localization. This phenomenon appears at the 'weak' points of the material volume (the points at which the material presents defects) just before failure and is concentrated in narrow zones. On the other hand, steel is a ductile material and localization appears in zones of high level of shearing (shear bands).

Modeling of materials which present softening response, as the above mentioned, becomes complicated due to the localization phenomenon. Mathematically, localization results in loss of ellipticity of the governing differential equations and in an ill-posed boundary value problem. The reason for this is the lack of a characteristic length (which is geometrically related to the zone at which during strain softening the energy is dissipated) in the consitutive modeling formulation. Subsequently, in numerical simulations, when the finite element method is used, it is observed a pathological sensitivity to the size of finite elements. In particular, localization appears to a band of finite elements and increasing the number of the elements ensues a finer mesh size and thus the dissipated energy reduces and tends to zero (Bažant and Belytschko 1985). In terms of mechanics, this means that failure happens with null energy dissipation and expresses a physically meaningless solution.

During the last two decades, there has been a significant evolution, including many approaches, about the constitutive description of the behavior of materials that present strain softening and the computational remedy of the localization. However, modeling of

structural response until failure still remains a challenging issue of solid mechanics.

1.6 Regularization techniques

In the literature, various approaches that deal with accurate modeling of localization can be found. They can be categorized according to:

- The adopted theory of constitutive description of the material, including two main theories: classic phenomenological approach and micromorphic continuum theory.
    - o Classic phenomenological approach. Two main theories belong to this approach: theory of plasticity and damage mechanics.
    - o Micromorphic continuum theory. This family of theories is based on the constitutive description of the micro-structure. Additional terms are used for the kinematical description of the media. The virtual power method is involved, by including the second grade terms (Germain 1973).
- If continuity of the media is satisfied. There can be found the continuum and discrete approach. The continuum approach considers the continuity of the media, while the discrete approach is formed by the assumptions that the localization appears in a priori defined zones and that two constitutive models are assigned: one discrete model for the localzation zone and a continuous model for the material outside of the localzation zone (Dvorkin et al. 1990).
- The local or non-local character of the formulation used.
- The kinematical assumptions. It is possible to adopt kinematically enhanced formulations by discontinuities.

The most common remedies for mesh-dependency problems are the crack band approach, which is a continuum local approach and the continuum non-local methods by using in both cases classic phenomenological constitutive models. Higher order micromorphic continuum theories are mostly applied to regularize localization problems in soils. Kinematically enriched formulations constantly gain ground as well for the resolution of problems related to localization and mesh-sensitivity. These remedies will be further explained hereafter, with most of the attention paid at the last one, as it is the one adopted in this work for modeling RC structures from the peak until failure.

1.6.1 Crack band approach

The principle of the crack band approach, also known as fracture energy trick or mesh-adjusted softening modulus consists in the suitable modification of model parameters that control softening by considering an internal geometrical length related to the mesh size (Bažant and Oh 1983; Hillerborg et al. 1976). In particular and most commonly the volumetric fracture energy is adjusted for every finite element. The advantage of this method is that it results in no additional numerical cost, as the algorithmic structure of the finite element code remains intact and the only modifications concern the assigned values to the input material parameters of each finite element. This approach requires the analytical calculation of the dissipated volumetric energy and the possibility to relate a parameter of the model that controls softening to this energy. This method is already used in many finite element codes both research and commercial and is effecient for practical engineering simulations.

1.6.2 Non-local methods

Non-local methods (Pijaudier-Cabot and Bažant 1987) are more sophisticated but more systematic (Jirasek 1998) and belong to the family of localization limiters, named after their role to spread the localized strain or damage to a zone of finite elements. The principle of non-local methods of integral type is to average the chosen variable (usually being the strain or damage) nearby the Gauss point. Subsequently, the rest of the variables (e.g. stress) are calculated with respect to this averaged quantity. The width of the localized zone is defined by a new parameter known as the characteristic length. Thus, the localized zone corresponds no longer to the width of one finite element, but to a width defined by the characteristic length (the width of the zone at which the averaging is applied). For concrete material, the characteristic length can be computed as 2.7 times the largest heterogeneity, which is the maximum aggregate size, as proposed by Bažant and Pijaudier-Cabot 1989. Another practical rule, widely used, is to define the characteristic length as 3–4 times the average finite element length. Non-local techniques are elaborated for various types of models, such as plasticity models with softening (Bažant and Lin 1988a; Strömberg and Ristinmaa 1996), smeared crack models (Bažant and Lin 1988b; Jirásek and Zimmermann 1997) or microplane models (Bažant and Ožbolt 1990; Ožbolt and Bažant 1996). The non-local methods are easy and simple for the user, as the only extra parameter that needs to be defined is the characteristic length. Non-local methods

overcome the drawbacks of the crack band approach (see previous section), but they are numerically costly, as further iterations are needed between the global equilibrium and the resolution of the equations of the local constitutive model. In addition to this, for the case of RC structures, this type of method exhibits the disadvantage of having an impact on the numerical results, as stated by Richard et al. 2010. According to the authors, the steel reinforcement component is taken into account for the global equilibrium of the structure and consequently the reinforcement stresses and strains are affected by the use of the nonlocal technique.

1.6.3 Higher order Micromorphic continuum theory

Higher order Micromorphic continuum theory takes into account the micro-structure of granular materials by considering that the material consists of particles and each particle can be described as a continuum media of lower scale. At each particle kinematic properties are assigned in a more exhaustive way. In this theory the most popular approaches (1^{st} order) are based on the Cosserat (also known as micropolar) model and the second gradient models. The former (Cosserat 1909) considers an additional rotational degree of freedom at each material point, which is taken into account as a rigid particle. The latter (see for example Chambon et al. 2001) also considers the micro-structure of the media and consists in adding the 1^{st} and 2^{nd} order gradients at the definition of a given variable, often being the strain (sometimes this variable can be the damage variable depending on the selected constitutive model). Both approaches consist in enriching the media description by introducing characteristic internal lengths. Thus, the thickness of the localization band is defined as a function of these lengths and mesh-dependency problems are avoided. However, methods that take into account the micro-structure for the constitutive description of the material are proved to be numerically expensive.

Crack band approach is used as a regularization technique (in tension), concerning the constitutive model for concrete, for the 3D numerical simulations, conducted for the construction of the 3D interaction diagrams in Chapter 2. The chosen constitutive model for concrete includes certain parameters that allow for calibrating the post-peak response based on the fracture energy.

1.6.4 Kinematically enhanced formulations by discontinuities

Kinematically enhanced formulations by discontinuities are based on the introduction of a new variable representing a discontinuity in the strain field (weak discontinuity) or the displacement field (strong discontinuity) of the finite element (Jirásek 2002). These methods consider a mutli-scale framework such that the discontinuity inserted in the small scale is related to the large-scale problem. The constitutive description of the material at the discontinuity is represented by a cohesive law, which allows to capture the energy dissipation in the large-scale. Hence, mesh-dependency problems are overcomed. Models with weak discontinuities (Belytschko et al. 1988) maintain the continuity of the displacement field but not of the strain field and thus numerical issues appear, since continuum constitutive models are applied (Wells and Sluys 2000). The strong discontinuity formulation (Oliver 2000) consists in the enrichment of the dispacement field with additional discontinuous shape functions associated to the discontinuity component. In this work, this approach is chosen in order to simulate the response of RC structures until failure.

In order to implement the enhanced formulations by strong discontinuities, two main methods exist: the extended finite element method (X-FEM) and the embedded finite element method (E-FEM). The former is based on the Partition of Unity Method (PUM) (Wells and Sluys 2001) and the additional discontinuity variables (displacement jumps) are assigned to the nodes of the structure, and thus they are considered global variables, resulting to additional numerical cost. The latter considers the additional discontinuity variables as elementary variables, assigned to the Gauss points of the element. In this method, the additional equations are solved in a local level, by static condensation. Therefore, the E-FEM preserves the algorithmic structure of the finite element code.

In Chapter 4, the E-FEM is chosen for the development of the numerical tool, to reproduce RC structural behavior til failure, due to the above mentioned advantages that it presents.

1.7 Cohesive models

The concept of cohesive zone was initially concieved by Dugdale (Dugdale 1960) and Barenblatt (Barenblatt 1962). It considers the fracture process zone as a cohesive zone constituted by two virtual surfaces formed at the crack tip and between these surfaces there is traction which decreases with increasing separation of the surfaces. Once traction vanishes, these virtual surfaces correspond to real cracks. The behavior of the cohesive

zone is described by a traction-separation law (TSL). The area under the TSL is equal to the necessary energy for the opening of the surfaces. Approaches that use cohesive models are efficient for dealing with problems the geometry of which includes or not initial cracks. They have been successfully applied to a variety of different materials and loading scenarios.

A lot of research has been conducted for the development of TSLs as they control the cohesive zone model behavior. All the TSLs have the following features in common:

- The area under the TSL represents the critical energy release rate.
- The maximum traction represents the maximum tensile or shear strength of the material.

What differentiates the several existing TSLs is their shape. The most usual shapes are bilinear, exponential and trapezoidal (see for example Camanho et al. 2003, Xu and Needleman 1994 and Tvergaard and Hutchinson 1993, respectively). Shet and Candra (Shet and Chandra 2002) presented in a brief way an anthology of some well-known cohesive models found in the literature (see Table 1.2 and Table 1.3).

In Chapter 4, a linear global cohesive model is proposed (in terms of cohesive moment-rotation jump), and is coupled to the continuous stress-resultant model (macroelement developed in Chapter 3) following the same principle of TSL: moment decreases with increasing development of the plastic hinge.

Table 1.2: Various cohesive models and their parameters (Shet and Chandra 2002). Corresponding references: (1): Barenblatt 1959; Barenblatt 1962, (2): Dugdale 1960, (3): Needleman 1987, (4): Rice and Wang 1989, (5): Needleman 1990b, (6): Needleman 1990a.

Year and author	Proposed Model	Model parameters	Problem solved	Model constants	Comments
(1) 1959, 1962 Barenblatt	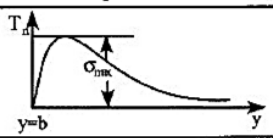	$K = \int_0^{t'} \frac{G_1(t)dt}{\sqrt{t}} = \sqrt{\frac{\pi E T}{1-\nu^2}}$ (ductile) $= \sqrt{\frac{\pi E T_0}{1-\nu^2}}$ (brittle) $T = T_0 + T_1$ T_0 = work of separation for britt. mater. T_1 = work of plastic deformation	Perfectly brittle materials.		The first to propose the cohesive zone concept.
(2) 1960 Dugdale	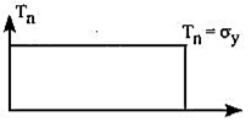	$\frac{s}{a} = 2 \sin^2\left(\frac{\pi}{4}\frac{T}{\sigma_y}\right)$ For small value of T/σ_y $\frac{s}{l} = 1.23\left(\frac{T}{\sigma_y}\right)^2$	Yielding of thin ideal elastic-plastic steel sheets containing slits.	Plastic zone ranges from 0.042 to 0.448 (in.)	Cohesive stress equated to yield stress of material.
(3) 1987 Needleman	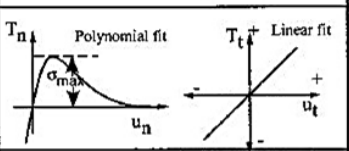	ϕ_{sep} = work of separation δ = normalizing parameters σ_{max} = cohesive strength	Particle-matrix decohesion.	$\delta = 10^{-9}$ to 10^{-8}m Cohesive Energy 1 to 10 J/m 2 $\sigma_{max} = 1000 - 1400$MPa $\sigma_y = 350 - 450$MPa	Phenomenological model. predicts normal separation
(4) 1989 Rice & Wang	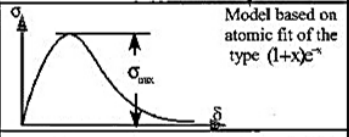	E_0 = initial Young's modulus h = normalizing parameter σ_{max} = maximum stress α = constant $(\frac{\pi h}{\alpha^2} = 2\gamma)$	Solute segregation.		Ascending part is equated to E_0 considers normal separation and ignores shear separation.
(5) 1990 Needleman	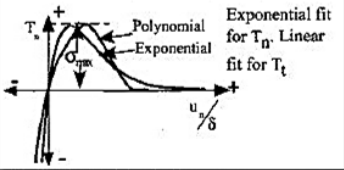	ϕ_{sep} = work of Separation δ = normalizing parameters σ_{max} = cohesive strength	Particle-matrix decohesion.	$\delta = 10^{-9}$ to 10^{-8}m	Predicts normal separation.
(6) 1990 Needleman	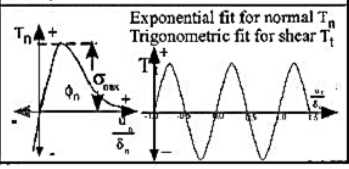	ϕ_n, ϕ_t = work of normal and shear separation δ_n, δ_t = critical displacements σ_{max} = cohesive strength	Decohesion of interface under hydrostatic tension.	$\delta_n = \delta_t = 2 \times 10^{-10}$ to 2×10^{-9} m $J_{1C}/\phi_n = 0.57 \sim 2.59$ $\sigma_{max}/\sigma_0 = 2,3$	Periodic shear traction to model Pierlels shear stress due to slip.

Table 1.3: Various cohesive models and their parameters, Continued (Shet and Chandra 2002). Corresponding references: (7): Tvergaard 1990, (8): Tvergaard and Hutchinson 1992, (9): Xu and Needleman 1993, (10): Camacho and Ortiz 1996, (11): Geubelle and Baylor 1998.

Year and author	Proposed Model	Model parameters	Problem solved	model constants	Comments
(7) 1990 Tvergaard	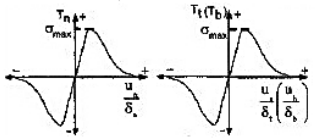	δ_n, δ_t = critical displacements σ_{max} = cohesive strength	Interfaces of whisker reinforced metal matrix composites	$\delta_n = \delta_t = 1\times10^{-3}$m. E = 60GPa (Young's mod) $\sigma_y/E = 0.005$ $\sigma_{max}/\sigma_y = 5\sim9$	Quadratic Model.
(8) 1992 Tvergaard & Hutchinson	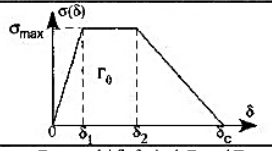	Γ_0 = work of separation. δ_0 = critical displacement σ_{max} = peak normal traction/interface strength δ_1, δ_2 = factors governing shape	Crack growth in elasto-plastic material, peeling of adhesive joints	$\Gamma_u/\Gamma_0 = 0\sim10$. ($\Gamma_0$ = Pl wk.), $\delta_t^*/\delta_n^* = 1$ $\sigma_{max}/\sigma_y = 0\sim14$ $\delta_1, \delta_2 = 0.15, 0.5$ $\sigma_y/E = 1/300$	Claims shape of separation law are relatively unimportant.
(9) 1993 Xu & Needleman	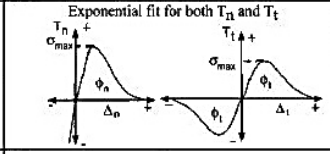	ϕ_n = work of normal separation ϕ_t = work of shear separation δ_n, δ_t = critical displacements σ_{max} = cohesive strength	Particle-matrix decohesion	$\delta_n = \delta_t = 2\times10^{-10}$ to 2×10^{-9} m	Predicts shear and normal separation.
(10) 1996 Camacho and Ortiz	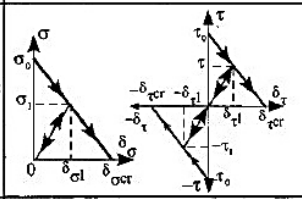	σ_0, τ_0 = normal and shear stress at fracture initiation $\delta_{\sigma cr}, \delta_{\tau cr}$ = critical normal and shrear opening displacement G_c = fracture energy	impact	Alumina: σ_0= 400 MPa $\delta_{cr} = 1.7\times10^{-3}$m Steel: σ_0 = 1500MPa $\delta_{\sigma cr} = 5.43\times10^{-6}$m	Uses additional fracture criterion. Predicts failure by both shear and normal separation in tension and by shear separation in compression.
(11) 1997 Geubelle & Bayler	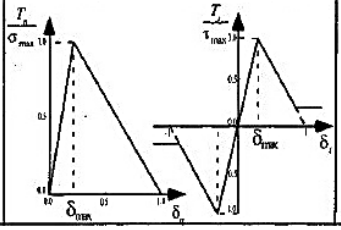	ϕ_n, ϕ_t = work of normal and tangential separation Δ_n, Δ_t = normal and tangential displacement jump δ_n, δ_t = normal and tangential interface characteristic length	Delamination by low-velocity impact	σ_{max}= E/100 to E/10 critical normal displacement jump $\Delta_n^c = 10^{-3}\sim10^{-4}$m	Bilinear model. Ascending curve can be matched to initial stiffness of the material.

Chapter 2

Interaction diagrams for symmetrically RC square sections

3D interactions diagrams for symmetrically RC square sections with various reinforcement ratios are constructed using 3D nonlinear finite element simulations. The interaction diagrams are expressed in terms of generalized forces (axial force, bending moment and shear force) and allow to identify three characteristic states: the first characteristic state corresponds the elastic limit of concrete, the second to the elastic limit of the reinforcement bars and the third characteristic state to the peak values of the generalized forces – generalized displacements curves. 3D nonlinear finite element simulations of RC cantilever - type columns are presented and validated with experimental results. Numerical interaction envelopes are then derived and analytical convex expressions are provided. A comparison with existing interaction diagrams from the literature is finally proposed.

2.1 3D finite element modeling strategy

The 3D finite element modeling strategy used for the construction of the interaction diagrams is presented and validated hereafter. Suitable constitutive models for concrete and steel are first chosen and the 3D finite element model is validated with the experimental data of reinforced concrete columns submitted to cyclic loading.

2.1.1 Constitutive model for concrete and steel

Three widely used 3D constitutive model for concrete, already implemented in the finite element code Cast3M (Cast3M 2019), are studied hereafter in order to choose the most appropriate one for constructing the interaction diagrams. Based on damage mechanics they can reproduce the main phenomena controlling the nonlinear behavior of concrete. They are briefly described hereafter.

Mazars model (Mazars 1984)

Mazars model is a 3D model based on damage mechanics, uses a unique scalar damage variable and reproduces the dissymmetry in traction and compression. The damage criterion is written in terms of the equivalent deformation that allows to rephrase a triaxial state as an equivalent in uniaxial one. The Mazars model implemented in Cast3M can be coupled with a non-local integral regularization formulation to avoid mesh dependency issues related to strain localization (Pijaudier-Cabot and Bažant 1987). The model is not suitable for cyclic loading as it can not reproduce inelastic (permanent) strains neither the crack closure effect.

RicRag model (Richard et al. 2010)

This 3D model adopts a decomposition of the elastic free energy into hydrostatic and deviatoric parts. Accordingly, it is assumed that the cracked behavior is separated into two independent ones; the hydrostatic part which controls the cracks opening and closure and the deviatoric one that controls the frictional sliding. A single damage variable is used and the dissymmetry in compression and tension is taken into account. The yielding surface is written in terms of the damage energy released rate, which is decomposed into direct extension mechanism (tension) and induced extension mechanism (compression). Hysteretic effects are considered only in compression as they are considered dominating. The unilateral effect is taken into account partially, because of the scalar nature of the unique damage variable. This model is implemented in Cast3M and the previously cited non-local integral regularization technique can be adopted.

Faria et al. model (Faria et al. 1998)

This 3D model is built within the damage mechanics framework and is coupled with plasticity to consider inelastic (permanent) strains during unloading in compression. Even though it does not account for permanent strains during tension unloading, during compression unloading the modulus is not elastic. The model accounts for the dissymmetry in tension and compression by using two scalar damage variables assumed to correspond to two independent processes. Two damage criteria are written in terms of equivalent stress, a tensile and a compressive one. As for the Mazars model, this formulation permits a mapping from the 3D stress tensor to a single equivalent 1D stress. Furthermore, it accounts for the increase of the concrete strength when biaxial or triaxial compressive

loading conditions are considered. This model accounts in a simplified way for the unilateral effect (no permanent strains during tensile unloading and no progressive stiffness recovery). Mesh objectivity is taken into account via a Hilleborg type approach (Hillerborg et al. 1976) (calibration of the tension softening branch according to the tensile fracture energy and a geometrical characteristic length).

Choosing the appropriate constitutive model

The response of the above models, already implemented in the official version of Cast3M, is numerically tested hereafter. For this, the biaxial behavior has been reproduced and compared to the classical experiments of Kupfer et al. 1969 using 2D or 3D finite element simulations (plane stress conditions were supposed for the 2D simulations, while in the 3D simulations the geometry of the specimen corresponds to a plate and thus the out of plane principal stress was supposed negligible). The 2D and 3D simulations provided similar results. For each region of stress combinations, different stress ratios σ_1/σ_2 were chosen and maintained constant. Force control was adopted to apply the loading.

Figure 2.1 illustrates the results of the biaxial behavior for the three constitutive models. The constitutive models of Mazars and Richard et al. underestimate the concrete strength under bi-compression, the second one also overestimates the concrete strength under combined tension-compression loading conditions. On the contrary, there is a good agreement between numerical and experimental results with the model of Faria et al. It can be observed that the model realistically reproduces the biaxial concrete strength and this for all loading conditions.

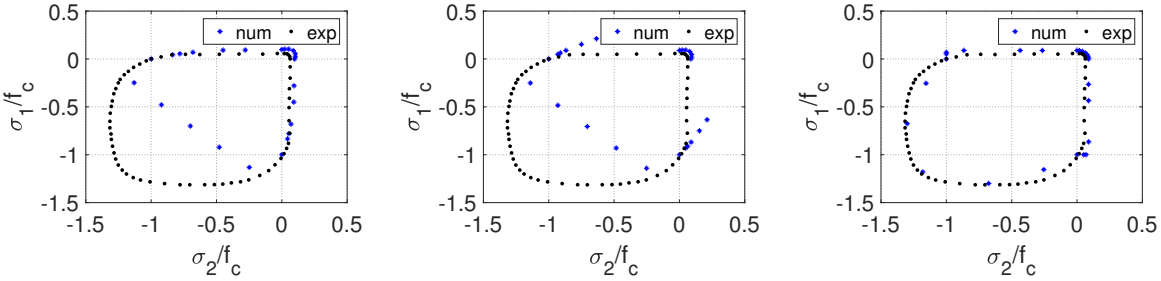

(a) Mazars model (b) Richard et al. model (c) Faria et al. model

Figure 2.1: Comparisons of the numerical and experimental biaxial strengths of concrete normalized by the uniaxial concrete compressive strength f_c for the three constitutive models.

In addition to these, in Figure 2.2, the principal stress-strain curves of the experiments

of Kupfer et al. 1969 under bi-compression are satisfactorily reproduced by the model of Faria et al. (Faria et al. 1998) and thus the volumetric behavior (including volume reduction and dilatancy) under bi-compression is assumed to be adequately represented by the Faria et al. model.

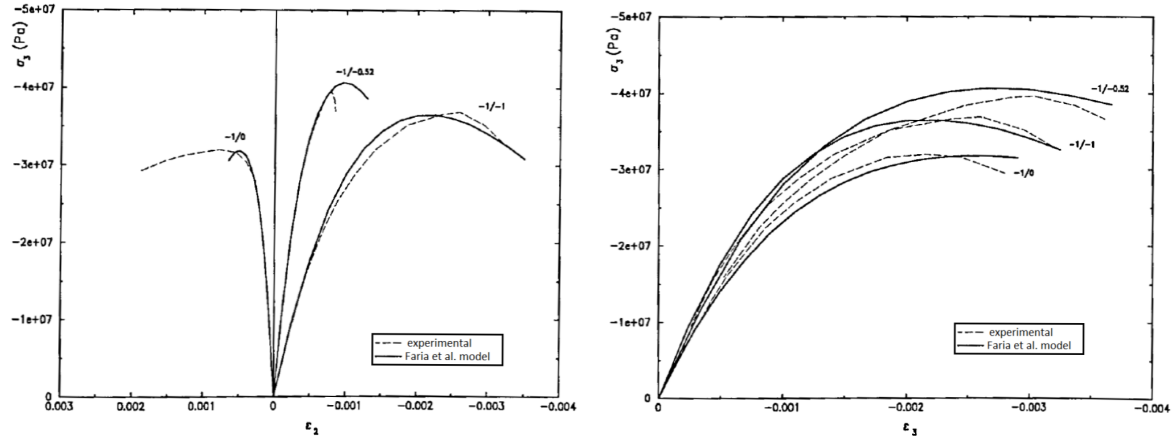

(a) σ_3-ϵ_2 in bi-compression. (b) σ_3-ϵ_3 in bi-compression.

Figure 2.2: Comparisons of the numerical predictions (Faria 1994) with experimental results (Kupfer et al. 1969) for concrete under bi-compression ($\sigma_1 = 0$) for $\sigma_3/\sigma_2 = -1/0$, $\sigma_3/\sigma_2 = -1/-1$ and $\sigma_3/\sigma_2 = -1/-0.52$.

Finally, the model of Faria et al. is taking into account the increase if concrete strength due to 3D confinement as it is shown in Figure 2.3, with some deviations from the experimental results which are considered acceptable according to the authors (Faria et al. 1998), given the scope of applications of the model.

The model of Faria et al. is therefore chosen in the following for the construction of the interaction diagrams. Its formulation is detailed hereafter.

Formulation of the Faria et al. model (Faria et al. 1998)

The model follows the damage mechanics framework and is coupled with plasticity to consider inelastic permanent strains in compression. The 3D (effective) stress tensor is defined by:

$$\bar{\sigma}(\epsilon, \epsilon^p) = D_0 : (\epsilon - \epsilon^p) \tag{2.1}$$

where D_0 is the fourth-order isotropic linear elastic constitutive matrix, ϵ is the strain tensor and ϵ^p is the plastic strain tensor. Stress contributions due to tension or compression are expressed by spliting the effective stress tensor into tensile $\bar{\sigma}^+$ and compressive

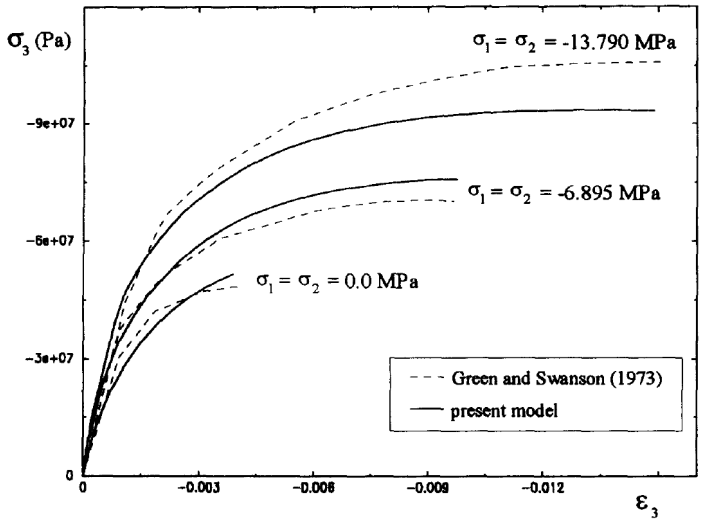

Figure 2.3: Comparisons of the numerical predictions (Faria et al. 1998) with experimental results (Green and Swanson 1973) for concrete under 3D compression: increasing normal stress for three different levels of confining stress.

$\bar{\sigma}^-$ components:

$$\bar{\sigma}^+ = \sum_i \langle \bar{\sigma}_i \rangle p_i \otimes p_i \tag{2.2}$$

$$\bar{\sigma}^- = \bar{\sigma} - \bar{\sigma}^+ \tag{2.3}$$

where $\bar{\sigma}_i$ is the i_{th} principal stress, p_i is the unit vector corresponding to the i_{th} principal direction, $\langle \cdot \rangle$ are the Macaulay brackets (ramp function) that return the value of the enclosed expression if positive, setting a zero value if negative and indices $(+)$ and $(-)$ correspond to tensile and compressive entities, respectively.

Even though it does not account for permanent strains during tension, the model is able to reproduce the differences between tension and compression using two scalar damage variables which are assumed to correspond to two independent processes. Two damage criteria g^+ and g^- are considered:

$$g^+(\bar{\tau}^+, r^+) = \bar{\tau}^+ - r^+ \leq 0 \tag{2.4}$$

$$g^-(\bar{\tau}^-, r^-) = \bar{\tau}^- - r^- \leq 0 \tag{2.5}$$

with r^+ and r^- being the current damage thresholds, while $\bar{\tau}^+$ and $\bar{\tau}^-$ are defined as:

$$\bar{\tau}^+ = \sqrt{\bar{\sigma}^+ : D_0^{-1} : \bar{\sigma}^+} \tag{2.6}$$

$$\bar{\tau}^- = \sqrt{\frac{\sqrt{3}}{3} K I_1 + \sqrt{2 J_2}} \tag{2.7}$$

where $\bar{\tau}^+$ and $\bar{\tau}^-$ are the tensile and compressive equivalent stress respectively, I_1 and J_2 are the first invariant of the compressive stress tensor and the second invariant of the deviatoric compressive stress tensor respectively and K is a material parameter conceived to fit the ratio of 2D and 1D compressive strengths (the former corresponding to equal bi-compression and the latter to uniaxial compression) $\sigma_{c,2D}/\sigma_{c,1D}$ in experimentally observed values between $1.16 - 1.2$ (Kupfer et al. 1969). The model accounts for the increase of concrete strength when biaxial or triaxial compressive loading conditions are considered.

The unilateral effect, also known as stiffness recovery, which takes place as the load changes sign and results in tensile cracks' closure and gradual compressive stiffness recovery, is taken into account in a simplified way (no permanent strains during tensile unloading and no progressive stiffness recovery).

The evolution laws for the damage variables in tension and in compression are given by:

$$d^+ = G^+(r^+) = 1 - \frac{r_0^+}{r^+} e^{A^+(1 - r^+/r_0^+)} \tag{2.8}$$

$$d^- = G^-(r^-) = 1 - \frac{r_0^-}{r^-}(1 - A^-) - A^- e^{B^-(1 - r^-/r_0^-)} \tag{2.9}$$

where r^+ and r^- are the current damage thresholds as already stated, r_0^+ and r_0^- are the elastic thresholds, A^+ controls the softening response in tension and A^- and B^- define the nonlinear part of the response in compression.

The plastic strain tensor rate in compression is given by:

$$\dot{\epsilon}^p = \beta E H(\dot{d}^-) \frac{\langle \bar{\sigma} : \dot{\epsilon} \rangle}{\bar{\sigma} : \bar{\sigma}} D_0^{-1} : \bar{\sigma} \tag{2.10}$$

where $\beta \geq 0$ is a material parameter which controls the rate intensity of plastic deformation and H is the Heaviside function. The consideration of plastic strains during compression and of the unilateral effect makes the constitutive model appropriate for cyclic loading.

Mesh objectivity (in tension but not in compression) is taken into account via an energy type approach (Hillerborg et al. 1976) that requires that the tension softening branch (parameter A^+) is calibrated according to the tensile fracture energy and a geometrical characteristic length:

$$A^+ = \left(\frac{G_f E}{l_{ch}(f_0^+)^2} - \frac{1}{2} \right)^{-1} \geq 0 \tag{2.11}$$

where G_f is the tensile fracture energy, E is the Young's modulus, f_0^+ is the tensile elastic limit, l_{ch} is a geometrical characteristic length computed as $\sqrt[3]{\Delta V}$ with ΔV the finite element volume in 3D simulations. Although this approach is not able to regularize the results in the local level, results in terms of forces and displacements are less sensitive to the finite element mesh discretization (Bažant and Oh 1983). It is important to mention that the rule of selecting the characteristic length as the element area (2D finite elements) or volume (3D finite elements) should be carefully used, as it can lead to errors for elongated and distorted elements; errors can be also obtained for square or cube elements if the crack band is not aligned with the mesh, as demonstrated in the work of Jirásek and Bauer 2012. This type of regularization can therefore provide results that may depend on the mesh orientation.

As for the constitutive description of the steel, the classical 3D Von Mises elastoplastic law is considered for the reinforcement bars and the stirrups. A linear kinematic hardening is adopted to capture the Bauschinger effect observed during cyclic loading. Figure 2.4 depicts the behavior of the steel, represented by the adopted constitutive model, during a uniaxial cyclic test.

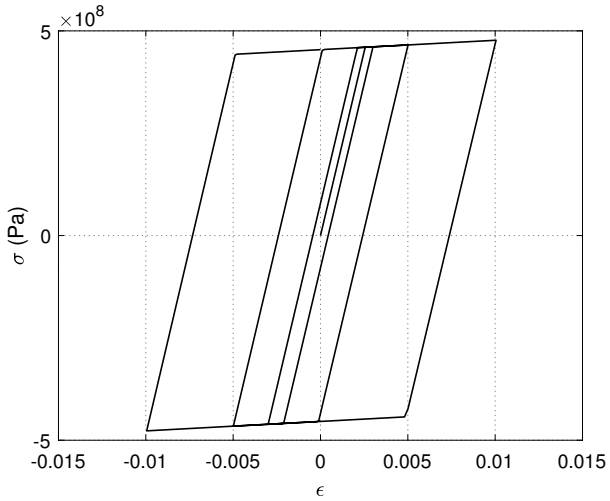

Figure 2.4: Steel cyclic behavior during 1D cyclic test.

2.1.2 Experimental campaign chosen for validation of the numerical model

In order to validate the 3D finite element modeling strategy that will be used in section 2.4 to construct the interaction diagrams, nine out of twelve reinforced concrete cantilever - type columns, studied experimentally by Bousias et al. (Bousias et al. 1995) under various loading combinations, are simulated hereafter. During this campaign Bousias et al. studied the behavior of identical columns under cyclic uniaxial or biaxial flexure with constant or time varying axial load. The only test variables were the load path and the concrete compressive strength. The loading program of the experimental campaign is schematically presented in Table 2.1.

Test Specimen	f_c' (MPa)	$N/A_c f_c'$	Load Path
S1	29.0	0.12	δx δy
S2	31.1	0.15	δy δx
S3	29.9	0.17	δx Fy
S4	27.7	0.15	δx Fy
S5	33.1	0.12	δy δx
S6	25.7	0.10	δy δx
S7	28.1	0.12	Expanding
S8	25.4	0.11	Shrinking
S9	23.9	0.03/0.15	δy Circle δx

Table 2.1: Test specimens, compressive strength, applied axial load and transversal load schematically represented (Bousias et al. 1995).

The geometry of the specimens is represented in Figure 2.5 (Gutierrez et al. 1993).

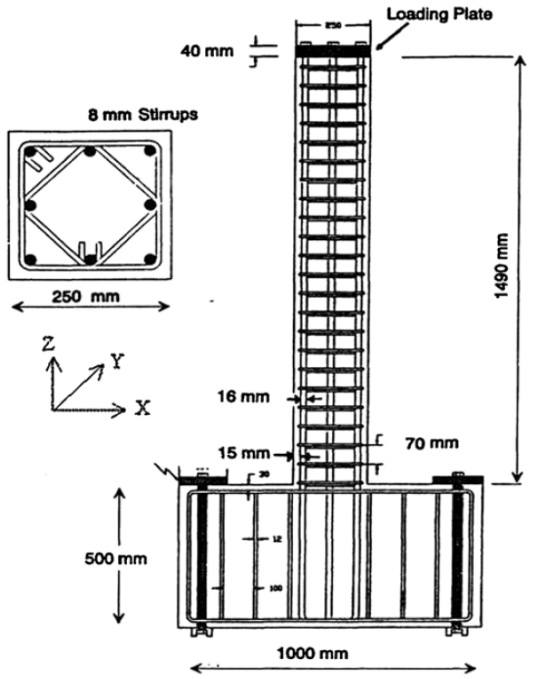

Figure 2.5: RC columns: geometry (Gutierrez et al. 1993).

2.1.3 Finite element mesh & boundary conditions and load control

3D volumetric finite elements of eight Gauss integration points with linear shape functions and the finite element code Cast3M are used to reproduce the behavior of the RC columns. All the components of the reinforced concrete column are discretized; concrete, longitudinal reinforcing steel bars and stirrups. Perfect bonding is assumed between concrete and steel. The finite element mesh of each component is constructed independently. In order to optimize the computational study and to see the influence of the mesh size, a coarse mesh with 10560 finite elements (Figure 2.6) and a fine mesh with 31560 finite elements (Figure 2.7) are prepared. At the section level, the characteristic size of the finite elements is 0.025m for the coarse mesh and 0.0125m for the fine mesh. The RC columns were cast in a heavily RC foundation. Accordingly, displacements are considered fixed at the bottom of the numerical model. Load control follows the experimental procedure defined in Table 2.1 (see also section 2.1.5). The Newton-Raphson algorithm is adopted at the global level for the resolution of the nonlinear system of equations. The radial return algorithm and the backward-Euler scheme is used for the integration of the constitutive law.

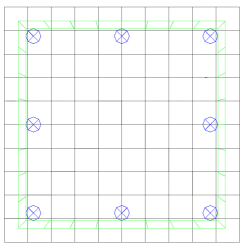

(a) section of the column

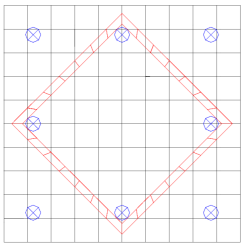

(b) section of the column

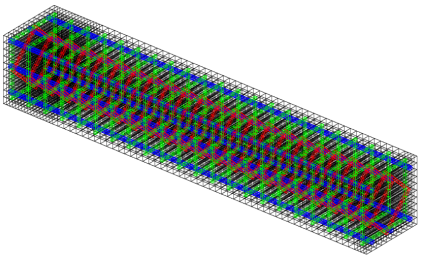

(c) 3D mesh

Figure 2.6: Coarse mesh.

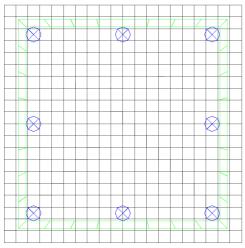

(a) section of the column

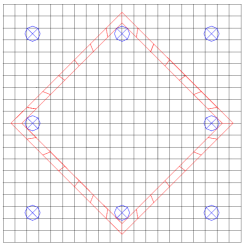

(b) section of the column

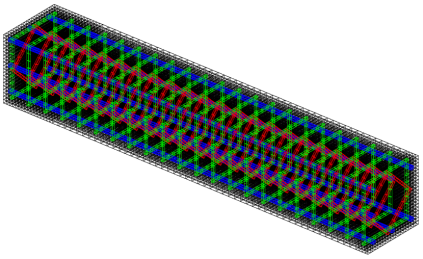

(c) 3D mesh

Figure 2.7: Fine mesh.

For convenience purposes, the nodes of the concrete and steel meshes do not necessarily coincide. Displacement compatibility is however ensured by forcing the mesh of the steel reinforcement to hang on the mesh of the concrete. More specifically, every nodal displacement of the reinforcing steel mesh follows a linear combination of the nodal displacements of the finite element of concrete mesh in which it is located.

About the additional stiffness

The above meshing technique of embedding the mesh of the steel into the mesh of the concrete and imposing displacement compatibility results to an additional structural stiffness. To quantify its influence on the global response, another finite element model is considered and two different meshing techniques are applied: one by adopting the above mentioned method (AS) and another method (discrete) where the nodes of the concrete and steel meshes coincide (NC). Figure 2.8 show the global response in terms of moment - rotation for the two meshes, for the case of a reinforced concrete beam under flexion. More specifically, the beam is 0.2m x 0.2m x 2m and has four longitudinal reinforcing steel bars with a diameter of 10mm. Transversal reinforcing steel stirrups with 10mm diameter

are distributed every 100mm of beam length. The concrete cover is 20mm. The beam is considered fixed on its left edge while a displacement controlled flexural load (i.e. bending rotation) is applied on the right as a linear distribution of axial displacements, varying according to the distance of each node from the centroid of the section. It can be clearly observed in Figure 2.8 that the influence of this additional stiffness on the global response is negligible, as it has been similarly concluded in the work of Llau 2016.

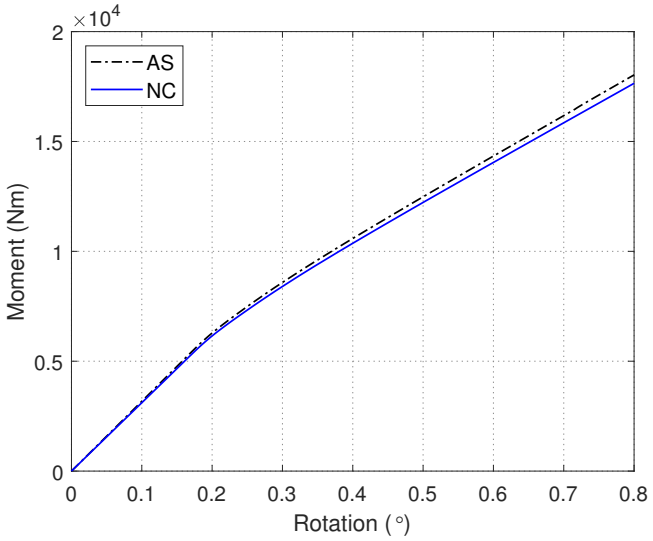

Figure 2.8: Comparison of global responses; AS: every point of the steel mesh follows a linear combination of the nodal displacements of the concrete mesh and NC: meshing technique where the nodes of different components coincide.

2.1.4 Material parameters

The parameters for 3D the concrete constitutive model (Faria et al. 1998) are listed in Table 2.2 and Table 2.3. More specifically, Table 2.2 contains the constant parameters for all the tests and Table 2.3 the varying ones.

Calibration of the nonlinear concrete compression response is done by selecting two points of the curve representing the uniaxial response in compression; point 1 (ϵ_{c1},σ_{c1}) and point 2 (ϵ_{c2},σ_{c2}). The choice of these points is fixed after applying a 'trial and error' method until concrete reaches its maximum strength at the predefined axial strain equal to 0.0035. The selected points vary for every test resulting to different resistances in compression according to the experimental values, see Table 2.1. An example of the calibration is presented in Figure 2.9 for the S2 and S9 tests.

Parameter	**Description**	**SI Unit**	**Value**
E_b	Young Modulus	GPa	15
ν_b	Poisson's ratio	-	0.2
f_t	Elastic stress limit in tension	MPa	2
G_f	Tensile fracture energy	J/m^2	100
l_{car}	Characteristic length	m	$\sqrt[3]{jaco}$
f_{c0}	Elastic stress limit in compression	MPa	-20
rt_{45}	Biaxial ratio in compression	-	1.18
f_{cu}	Ultimate stress limit in compression	MPa	-35
ϵ_{cu}	Ultimate deformation in compression	-	-0.0035
σ_{cp}	Reference stress in compression	MPa	-33
ϵ_{cp}	Reference strain in compression	-	-0.0044
ϵ_{c1}	Deformation of point 1	-	-0.002
ϵ_{c2}	Deformation of point 2	-	-0.005

Table 2.2: RC columns: concrete parameters (constant for all the tests).

Parameter	σ_{c1}	σ_{c2}
Description	Stress of point 1	Stress of point 2
SI Unit	MPa	MPa
S1	-25.4	-24.4
S2	-26.5	-25.5
S3	-26.0	-25.0
S4	-24.8	-23.8
S5	-27.5	-26.5
S6	-23.6	-22.6
S7	-24.8	-23.8
S8	-23.0	-22.0
S9	-22.5	-21.5

Table 2.3: RC columns: concrete parameters.

The reference stress σ_{cp} and strain ϵ_{cp} are used for the determination of the material parameter β. As stated in section 2.1.1, β is a material parameter which controls the rate intensity of plastic deformation and is given by Equation 2.12 (Faria 1994):

$$\beta = \frac{(E\epsilon_{cp} - \sigma_{cp})f_{cu}}{(E\epsilon_{cp} - f_{c0})(\sigma_{cp} + f_{cu})} \tag{2.12}$$

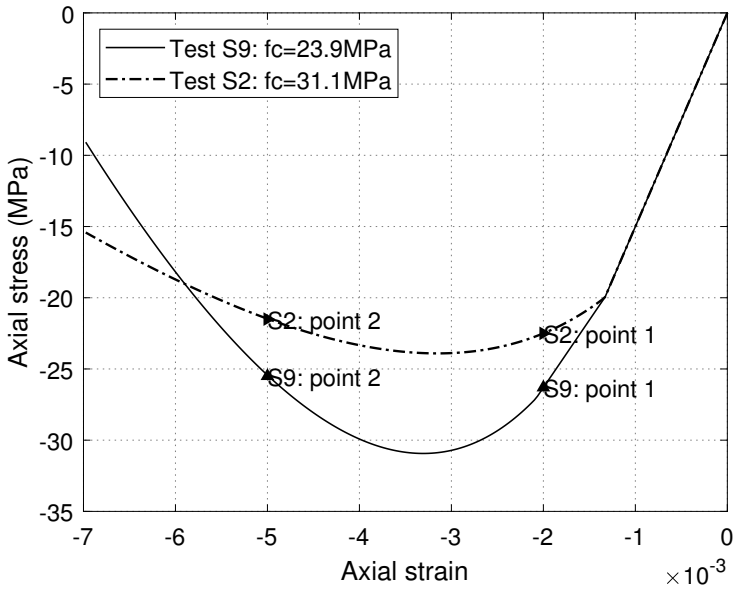

Figure 2.9: Calibration of the response in uniaxial compression: representation of points 1, 2.

The parameter β is not explicitly user-defined in Cast3M. By applying a 'trial and error' method, it has been shown that the ratio $\sigma_{cp}/\epsilon_{cp}$ is critical for the determination of β. As the ratio $\sigma_{cp}/\epsilon_{cp}$ increases, β decreases and the permanent plastic strains during unloading are less important. Conversely, as the ratio $\sigma_{cp}/\epsilon_{cp}$ decreases, β increases and the permanent plastic strains during unloading are more significant. An example of the influence of the parameter β on the permanent plastic strains is illustrated in Figure 2.10. When β tends to zero the model turns to a purely damage model in compression and the coupling with plasticity vanishes.

The parameters for the 3D steel constitutive model (Von Mises with linear kinematic hardening) are listed in Table 2.4.

Parameter	**Description**	**SI Unit**	**Value**
E_a	Young Modulus	GPa	180
ν_a	Poisson's ratio	-	0.3
f_y	Elastic stress limit	MPa	460
H_a	Kinematic hardening modulus	GPa	2.3

Table 2.4: RC columns: parameters for steel.

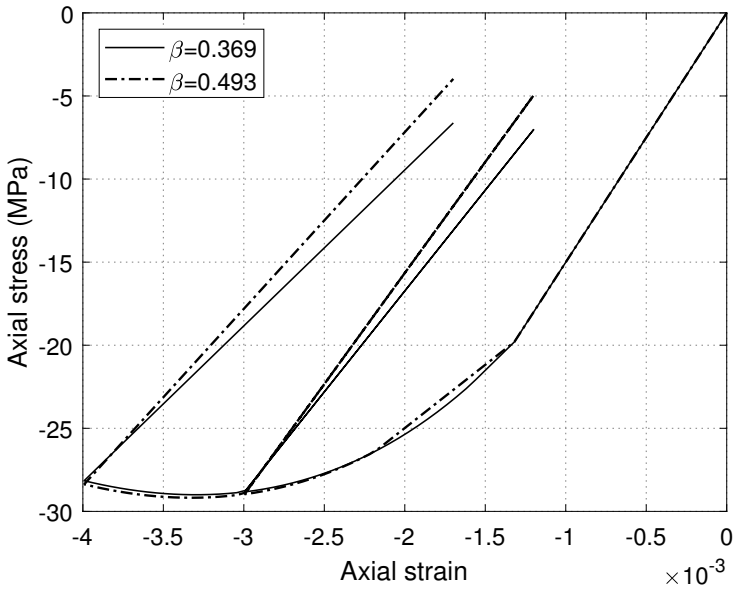

Figure 2.10: Cyclic response in uniaxial compression: influence of parameter β on the permanent plastic strains.

2.1.5 Validation

Optimisation of the computational time and mesh dependency

In order to optimize the computational time and to see the influence of the mesh size a comparison of the numerical results obtained with the coarse (Figure 2.6) and fine mesh (Figure 2.7) and the experimental data is shown hereafter for the S1 test. Loading is applied on the top of the column in two steps (see also Table 2.1); firstly, the axial compressive load is applied as a force of negative sign in the z direction and it is equally distributed to all the nodes of the section. Secondly, the transversal load along x, y is applied as a displacement homogeneous for all the nodes of the top section at the top or as a force equally distributed to all its nodes, according to the loading conditions of the test. It can be observed that the two meshes provide similar results. In the following, all calculations are therefore conducted with the coarse mesh.

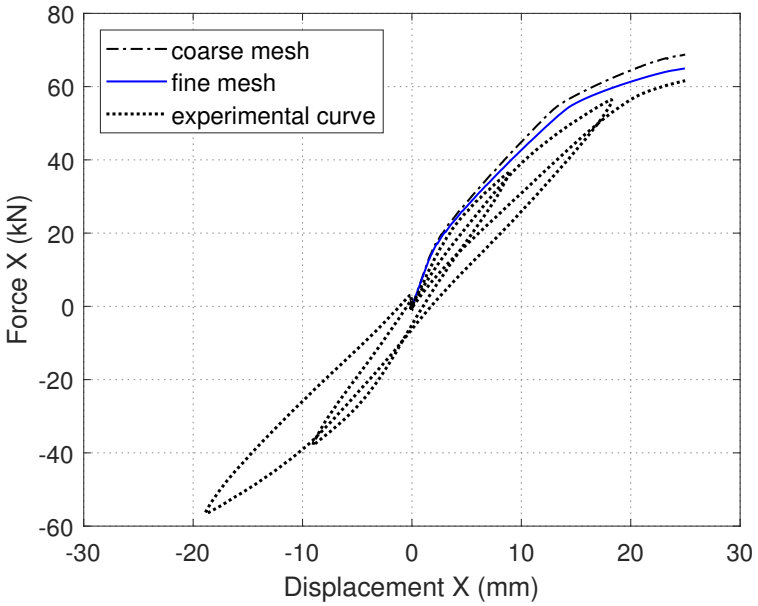

Figure 2.11: Test S1: comparison of the responses of the coarse and fine meshes with the experimental results.

Numerical vs. experimental results

S1 test

For the S1 test, loading is applied on the top of the column in two steps according to Table 2.1. Figure 2.12 presents the loading history and the numerical versus the experimental results. After concrete cracking and during alternate loads, the global response is mainly controlled by the reinforcement steel bars. For this calculation, the steel hardening modulus is taken equal to $H_a = 2.3GPa$ as reported in Bousias et al. 1995, see also Table 2.4. It can be clearly seen that global behavior in both directions is correctly reproduced, although the peak values are underestimated.

In order to improve the results and to investigate the influence of the steel hardening modulus on the global response, a parametric analysis has been carried out. In Figure 2.13 the results of the numerical simulations, conducted with a steel hardening modulus of $H_a = 20GPa$ are presented. As it can be observed, simulation results are improved, especially the peak values but also the unloading and reloading stages.

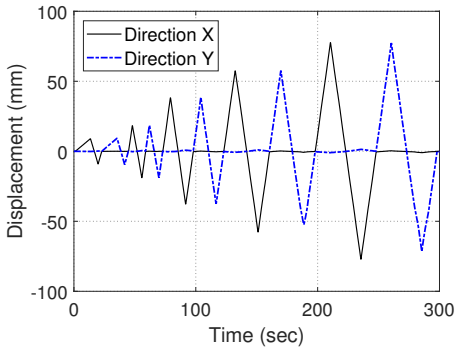

(a) Loading history

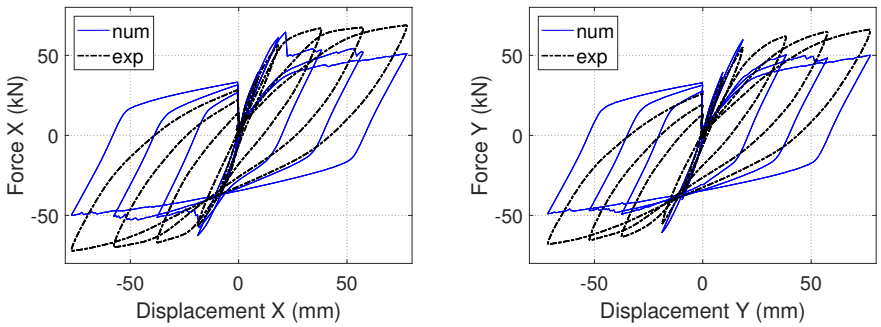

(b) Force-displacement, X direction (c) Force-displacement, Y direction

Figure 2.12: Test S1: Numerical vs. experimental results: $H_a = 2.3GPa$.

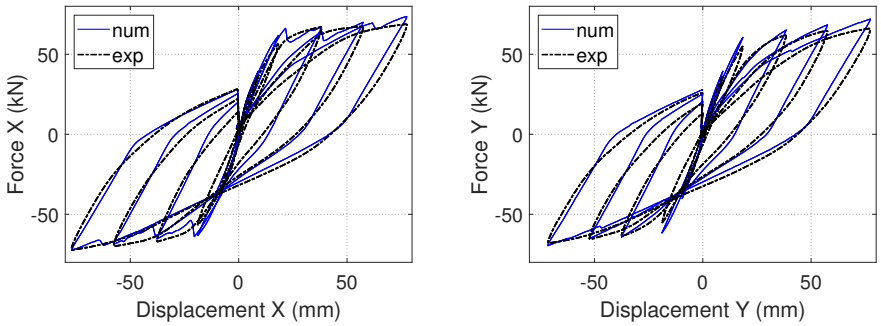

(a) Force-displacement, X direction (b) Force-displacement, Y direction

Figure 2.13: Test S1: Numerical vs. experimental results: $H_a = 20GPa$.

S2-S9 tests

The numerical versus the experimental results for the S6 and S8 tests are also presented in Figures 2.14-2.19, while for the rest of the tests the corresponding Figures can be found in the Annex. As for the S1 test, several figures are produced for each test:

- numerical results with $H_a = 2.3GPa$ (Bousias et al. 1995);
- numerical results with $H_a = 20GPa$;
- numerical results with a better fitting of the hardening modulus, see Table 2.5 for tests S6 and S8 (for the rest of the tests the corresponding Table can be found in the Annex).

Parameter	H_a		
Description	Kinematic hardening modulus		
	Reference value	**Calibration according to test S1**	**Best fit**
SI Unit	GPa	GPa	GPa
S6	2.3	20	5
S8	2.3	20	5

Table 2.5: RC columns: parametric study of the steel hardening: tests S6 and S8.

It can be observed for all the test that a better fit of the steel hardening modulus can significanlty improve the numerical results.

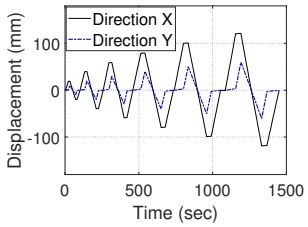

(a) Loading history

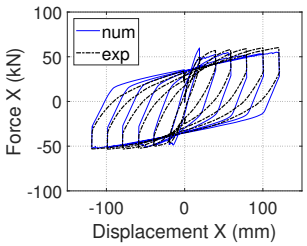

(b) Force-displacement, X direction

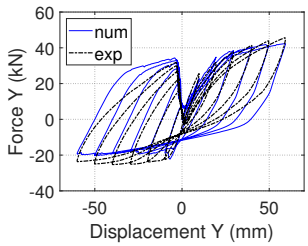

(c) Force-displacement, Y direction

Figure 2.14: Test S6: Numerical vs. experimental results: $H_a = 2.3GPa$.

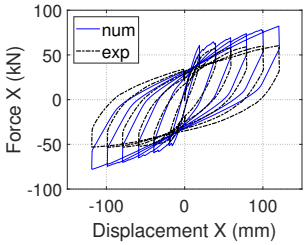

(a) Force-displacement, X direction

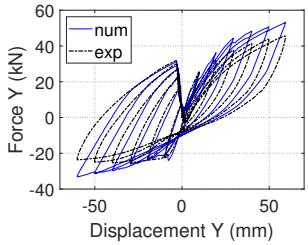

(b) Force-displacement, Y direction

Figure 2.15: Test S6: Numerical vs. experimental results: $H_a = 20GPa$.

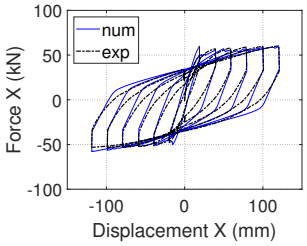

(a) Force-displacement, X direction

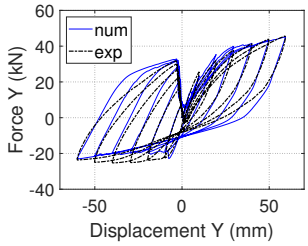

(b) Force-displacement, Y direction

Figure 2.16: Test S6: Numerical vs. experimental results: $H_a = 5GPa$.

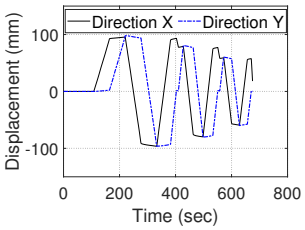

(a) Loading history

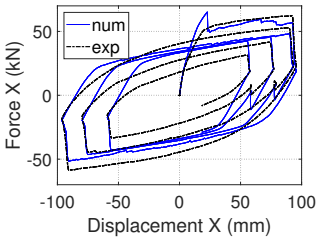

(b) Force-displacement, X direction

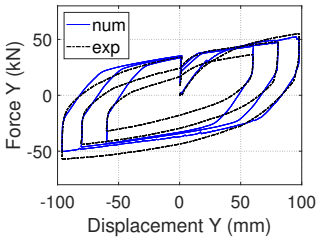

(c) Force-displacement, Y direction

Figure 2.17: Test S8: Numerical vs. experimental results: $H_a = 2.3GPa$.

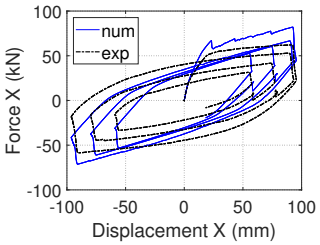

(a) Force-displacement, X direction

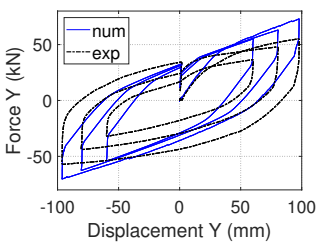

(b) Force-displacement, Y direction

Figure 2.18: Test S8: Numerical vs. experimental results: $H_a = 20GPa$.

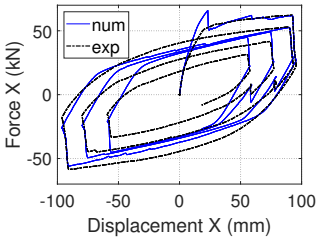

(a) Force-displacement, X direction

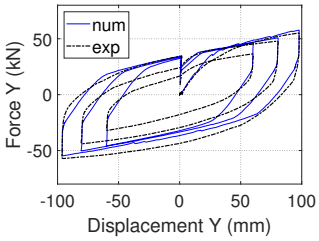

(b) Force-displacement, Y direction

Figure 2.19: Test S8: Numerical vs. experimental results: $H_a = 5GPa$.

The previous results (Figures 2.11 to 2.19) validate the 3D modelling strategy. For all the simulated tests, it is observed that a correctly calibrated steel hardening modulus can provide better approximations of the experimental curves. The obtained prediction accuracy can also improved using a non linear kinematic hardening or by taking into account steel - concrete interfaces (Richard 2010). The purpose of this PhD being however the numerical computation of 3D interaction diagrams up to failure and not the cyclic behavior, the level of accuracy, as far as the peak of the response is concerned, is judged adequate; the 3D chosen finite element modeling strategy reproduces satisfactorily the global behavior of the columns in terms of forces - displacements up to the peak and this for all the loading combinations and tests of the considered experimental campaign.

2.2 Characteristic states

The 3D finite element modeling strategy validated in section 2.1 is adopted for the construction of the interaction diagrams. In order to find them, the column is again considered fixed at the bottom and specific displacement loading combinations are applied on its free top surface. Interaction diagrams are presented for three characteristic states, defined hereafter:

- 1^{st} characteristic state: corresponds to the domain of elasticity.
- 2^{nd} characteristic state: corresponds to the elastic domain of the reinforcement steel bars (identical in tension and compression) fixed to $460MPa$.
- 3^{d} characteristic state (termed hereafter 'failure'): corresponds to the peak values of the generalized forces-generalized displacement curves. More specifically, for the combined flexion to tension area, the failure criterion, is given in terms of maximum longitudinal steel strain equal to 7.5%, following the Eurocode (CEN 2004). This criterion is applied in the numerical simulations by verifying that all the finite elements of the cross-section in one steel bar have reached this limit of longitudinal strain. For the combined flexion to compression region, failure is reached at the maximum axial force (absolute value). This choice is made because imposing a criterion in terms of concrete maximum compression stress leads to very conservative estimations, as the maximum axial force is reached after several material points have attained their ultimate resistance.

The driving idea behind the choice of the two last characteristic states is that steel controls the behavior of the reinforced concrete section when tension is predominant, while in compression, concrete crushing is considered which limits the buckling risk.

2.3 Loading program

In order to construct the interaction diagrams the following displacement controlled loading program is applied, based on the swipe and radial tests commonly used in geotechnical engineering, see for example Faccioli et al. 1999, Grange et al. 2008:

- 1D loading: pure tension and pure compression in order to obtain the uniaxial section resistance (Fig. 2.20).

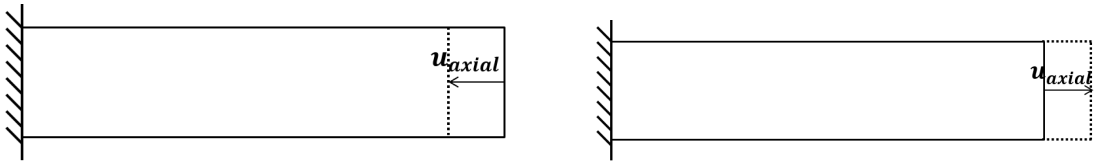

(a) applied tensile displacements (b) applied compressive displacements

Figure 2.20: Uniaxial loading.

- 2D loading: combined flexion with axial loading. The procedure is repeated in two ways; for the 2D swipe tests, an axial load is first applied followed by a flexure load (Fig. 2.21). The same procedure is repeated for different levels of axial loading. The axial load is applied similarly to the case of 1D loading, while the flexural load is applied as a linear distribution of axial displacements, see Fig. 2.21. For the radial

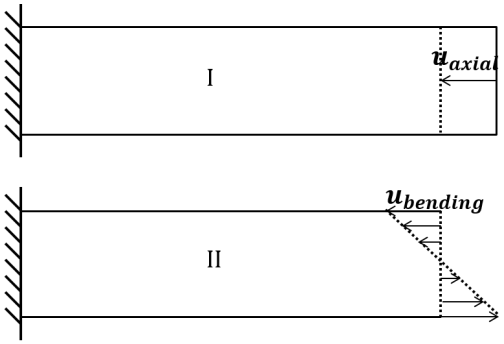

Figure 2.21: 2D swipe test: I: axial loading, II: radial bending loading.

displacemet controlled tests, the axial and flexural loads are applied simultaneously

(Fig. 2.22) by keeping their ratio constant. The procedure is repeated for different

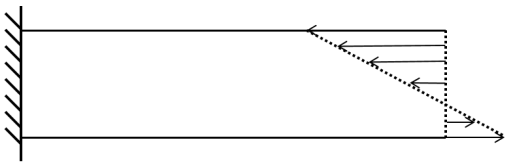

Figure 2.22: 2D radial test: coupled bending - axial loading.

ratios. The moment - axial force interaction diagram is obtained by both procedures and the results are compared in Figure 2.23 to verify the influence of the loading path, which is found negligible.

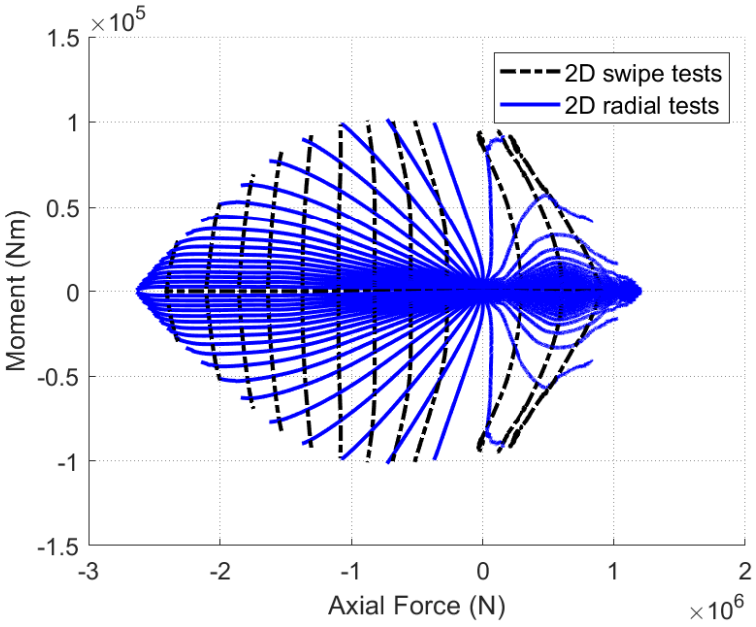

Figure 2.23: Mmoment - axial force interaction diagram obtained by 2D swipe tests and 2D radial tests.

- 3D loading: for different levels of axial loading, flexural and transversal loads (controlled in displacements) are simultaneously applied in a radial way (constant ratio), as presented in Fig. 2.24. Thus, the complete moment – axial force – shear force diagram is obtained. Additional radial tests (all loads are applied simultaneously) are also performed for selected cases to verify the influence of the loading path. It is again found that the interaction diagrams are not significantly affected by the loading path

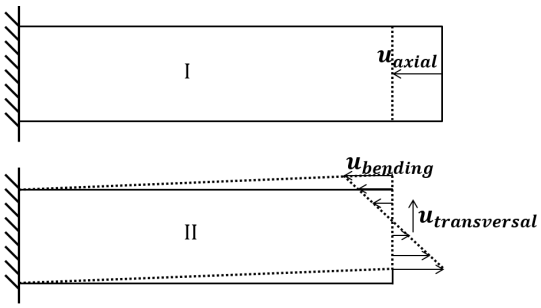

Figure 2.24: 3D loading: I: axial loading, II: radial bending and shear loading by keeping constant the ratio $u_{bending}/u_{transversal}$.

2.4 Interaction diagrams N,M,V

By the application of uniaxial, 2D and 3D loading conditions the moment - axial force - shear force interaction diagrams are produced and correspond to the inner section of the column, at $0.3m$ from the fixed edge. This section is found to be the most charged, is sufficiently far from the fixed edge (its distance from the fixed edge is greater than the largest cross-sectional dimension, following the Saint-Venant's Principle) and its planeness is verified. Numerical simulations of this member under pure flexion have also shown that after this length ($0.3m$) the results in terms of moment - curvature are practically homogeneous for all the sections, as shown in Figure 2.25.

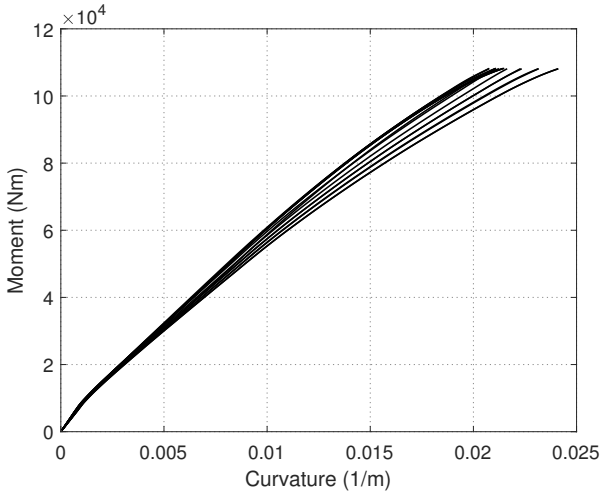

Figure 2.25: Moment - curvature diagrams at inner sections of the RC column, located at different distances varying from $0.2625m$ to $1.3625m$ from the fixed edge.

The discrete data obtained by numerical simulations corresponding the 2^{nd} and 3^d

characteristic states are respectively given in Figure 2.26 and Figure 2.27.

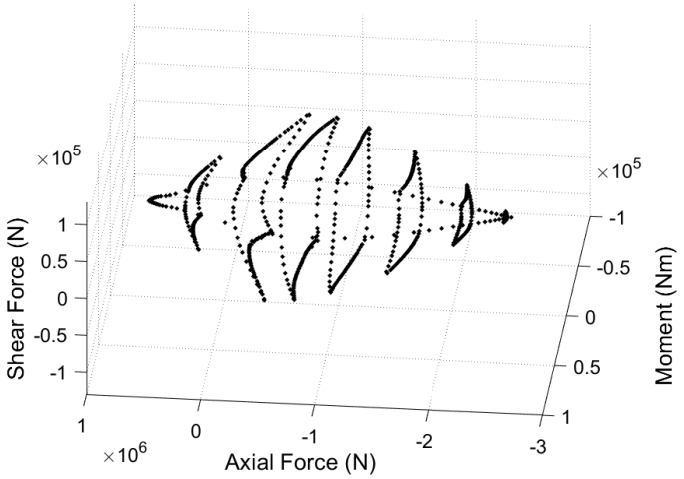

(a) 3D view

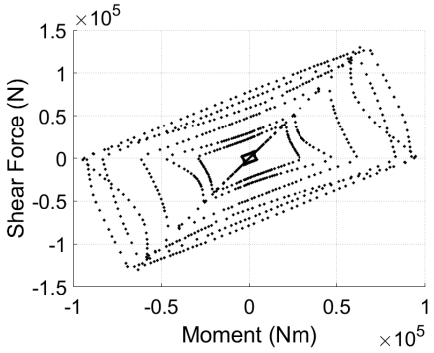

(b) View at the Shear Force-Bending Moment plane

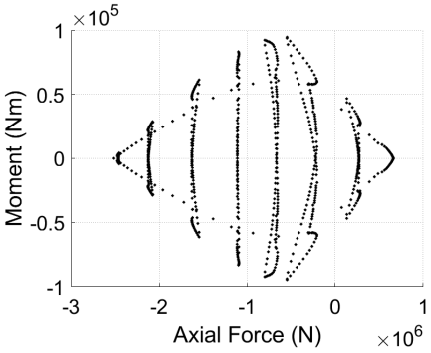

(c) View at the Bending Moment-Axial Force plane

Figure 2.26: 2^{nd} characteristic state (elastic domain of steel rebars): Interaction diagram (discrete points) obtained by numerical simulations.

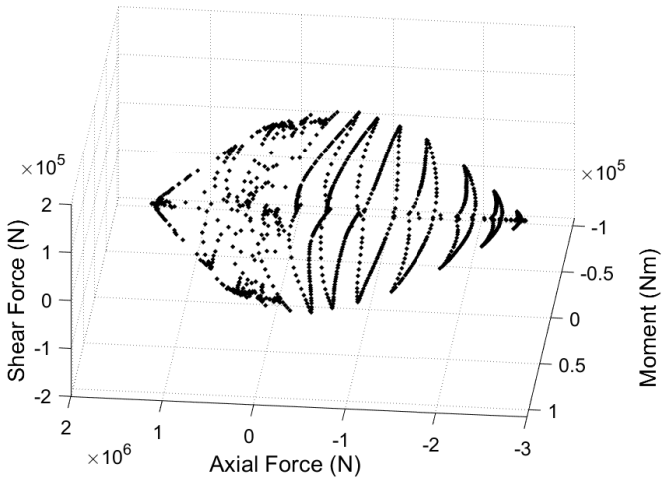

(a) 3D view

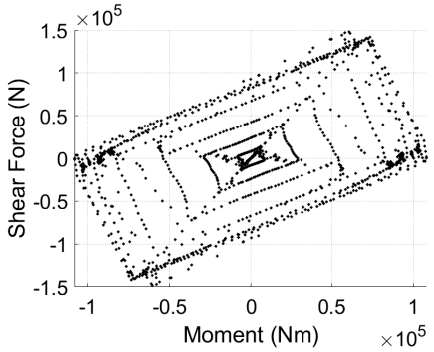

(b) View at the Shear Force-Bending Moment plane

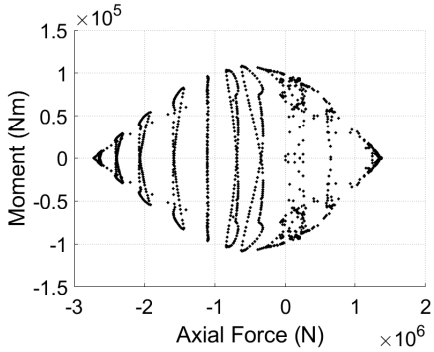

(c) View at the Bending Moment-Axial Force plane

Figure 2.27: 3^d characteristic state ('failure'): Interaction diagram (discrete points) obtained by numerical simulations.

Interaction diagrams for different reinforcement ratios are also constructed following the same procedure (the only difference in the numerical model is the number of the longitudinal steel bars and their diameter). Figure 2.28 presents interaction diagrams for the 3^d characteristic state ('failure') for sections M1, M2, M3 (initial validated model) and M4 for with the reinforcement ratios 1.01%, 2.01%, 2.57% and 5.15% respectively. It is found that as the reinforcement ratio increases, the failure domain expands, but the form of the interaction diagrams remains similar.

Given the same form for different reinforcement ratios, a stress-resultant model in terms of forces/moments-generalized strains (i.e. macroelement) can be formulated by considering the interaction diagram as a failure surface and intermidiate surfaces as the

loading surfaces. Further description of this strategy is presented in Chapter 3.

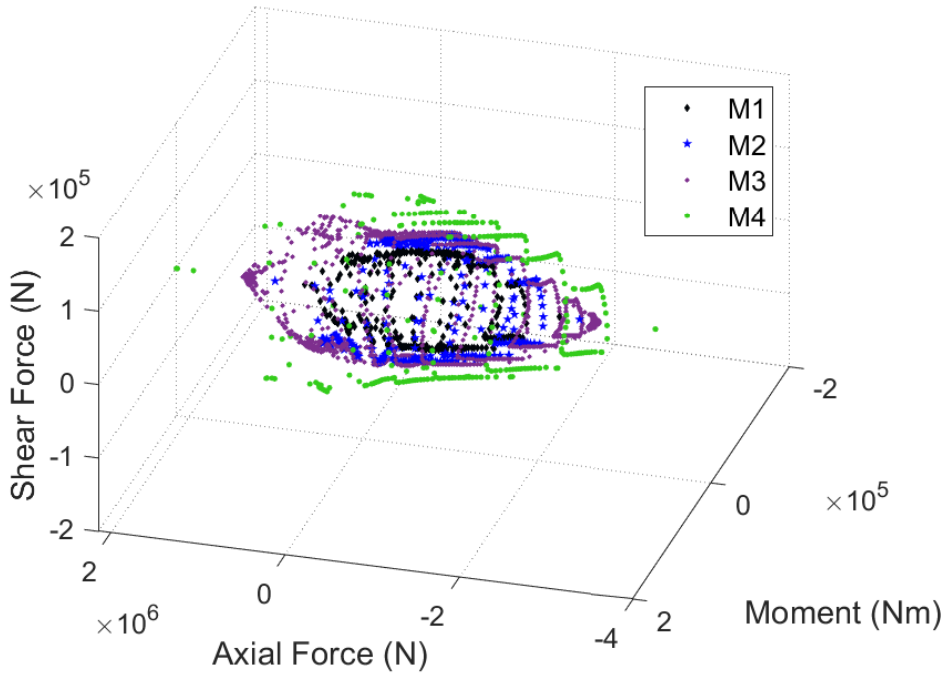

Figure 2.28: 3^d characteristic state ('failure'): Interaction diagrams (discrete points) for sections with different reinforcement ratios obtained by numerical simulations (M1 (1.01%), M2 (2.01%), M3 (initial validated model, 2.57%) and M4 (5.15%).

2.5 Comparison with Eurocode

For the 2D swipe tests in the moment - axial force space, a comparison of the failure surface obtained by the numerical simulations to the surface obtained by applying the methodology proposed in the Eurocode is provided in Figure 2.29 for the RC sections M1, M2, M3 and M4.

It can be observed that all surfaces obtained by finite element simulations and by the methodology described in the Eurocode present similar forms. Furthermore, as expected, the surface obtained by Eurocode underestimates the failure points. In the numerical model and for the combined flexion to traction area the ultimate longitudinal steel strain is fixed to 7.5%, see section 2.2. This criterion allows obtaining a less conservative interaction diagram, compared to the one from the Eurocode which (i) considers as an ultimate limit the point at which steel reaches its elastic limit in tension and (ii) ignores the

concrete tensile strength. The choice of a less conservative criterion can be beneficial for applications in civil engineering as it can lead to a more economical design of reinforced concrete structures. For the combined flexion to compression region, the numerically produced surface presents a good fit to the curve obtained by the method of Eurocode without application of security coefficients.

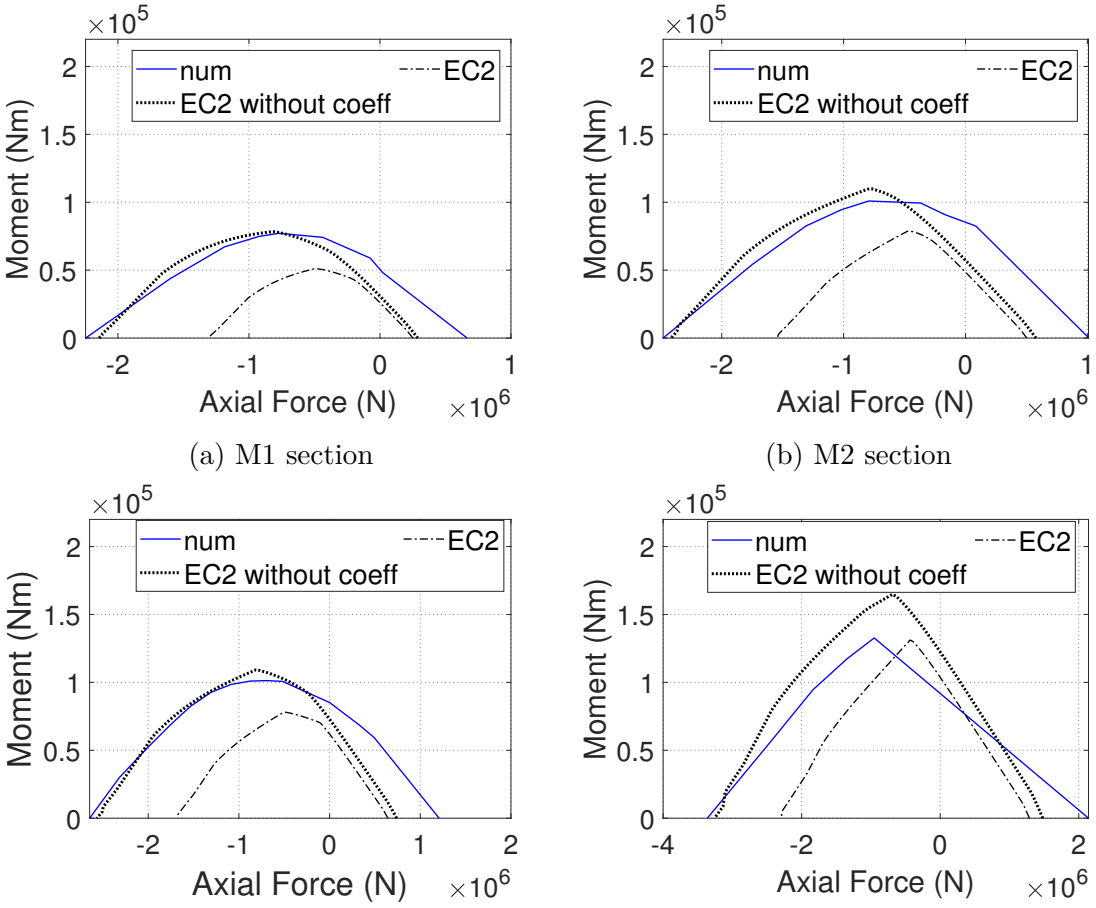

(a) M1 section

(b) M2 section

(c) M3 section

(d) M4 section

Figure 2.29: Moment - axial force interaction diagrams for the RC sections M1, M2, M3 and M4. Comparison of the numerical results with the one obtained by the method in the Eurocode with or without the appplication of the security coefficients.

2.6 Analytical convex expressions

2.6.1 Background

Analytical expressions of the interaction diagrams are very useful to practitioners to efficiently design reinforced concrete sections. For a robust numerical implementation, these functions should be convex.

Suryasentana et al. (Suryasentana et al. 2019) proposed a systematic framework employing a restricted set of sum of square convex polynomials for the construction of convex and sufficiently regular functions with the following characteristics: continuity, differentiability with a continuous gradient and Hessian, absence of singularities in the function and in its derivatives and the fact that they always have real values. Odd degree polynomials are excluded because of their lack of convexity. The restricted choice of homogeneous polynomials is justified by the direct identification of the coefficients which correspond to uniaxial loading conditions. The coefficients of the analytical expression of the failure envelope are computed through a convex optimization problem which minimizes the objective function:

$$F = \sum_{i=1}^{n} (f(\bar{X}_i^{\,data}) - 1)^2 \tag{2.13}$$

subjected to constraint: $\bar{Y}^\top \nabla^2 f(\bar{X}) \bar{Y}$ is sum of squares for all $\bar{X}$, $\bar{Y} \in$ domain of f, which guarantees that the Hessian $\nabla^2 f(\bar{X})$ of f is positive semi-definite. In Eq. 2.13 $\bar{X}_i^{\,data}$ is a vector of a discrete failure loading combination points and n is the number of failure points.

This procedure is adopted hereafter for the identification of the coefficients of the analytical expression and the sum of squares convex optimization problem is solved using YALMIP, a toolbox developed by Lofberg (Lofberg 2004) in Matlab together with the SeDuMi semi-definite solver (Sturm 1999).

2.6.2 Analytical expressions at failure (3^d characteristic state)

The procedure to compute the analytical expressions of the interaction diagram for the 3^d characteristic state has as follows:

1. At first, the data of the numerical simulations of section 2.4 are enriched in order to be used afterwards as input for the resolution of the sum of squares convex opti-

mization problem. In particular, every set of data of the numerical simulations (for sections M1, M2, M3, M4) are introduced in the following homogeneous polynomial expression of degree 6 (found to provide a good fit) in order to obtain the coefficients of the polynomial expression for each RC section tested, using a nonlinear least squares method:

$$f_6 = \sum_{\substack{i,j,k=0 \\ |i+j+k|=6}}^{6} a_{I(i,j,k)} \bar{N}^i \bar{M}^j \bar{V}^k - 1 \tag{2.14}$$

The complete expression of Equation 2.14 is given by:

$$\begin{aligned} f_6 = {} & a_1\bar{N}^6 + a_2\bar{N}^5\bar{M} + a_3\bar{N}^4\bar{M}^2 + a_4\bar{N}^3\bar{M}^3 + a_5\bar{N}^2\bar{M}^4 + a_6\bar{N}\bar{M}^5 + a_7\bar{M}^6 + \\ & a_8\bar{N}^5\bar{V} + a_9\bar{N}^4\bar{M}\bar{V} + a_{10}\bar{N}^3\bar{M}^2\bar{V} + a_{11}\bar{N}^2\bar{M}^3\bar{V} + a_{12}\bar{N}\bar{M}^4\bar{V} + a_{13}\bar{M}^5\bar{V} + \\ & a_{14}\bar{N}^4\bar{V}^2 + a_{15}\bar{N}^3\bar{M}\bar{V}^2 + a_{16}\bar{N}^2\bar{M}^2\bar{V}^2 + a_{17}\bar{N}\bar{M}^3\bar{V}^2 + a_{18}\bar{M}^4\bar{V}^2 + a_{19}\bar{N}^3\bar{V}^3 + \\ & a_{20}\bar{N}^2\bar{M}\bar{V}^3 + a_{21}\bar{N}\bar{M}^2\bar{V}^3 + a_{22}\bar{M}^3\bar{V}^3 + a_{23}\bar{N}^2\bar{V}^4 + a_{24}\bar{N}\bar{M}\bar{V}^4 + a_{25}\bar{M}^2\bar{V}^4 + \\ & a_{26}\bar{N}\bar{V}^5 + a_{27}\bar{M}\bar{V}^5 + a_{28}\bar{V}^6 - 1 \end{aligned} \tag{2.15}$$

2. This analytical expression, for which the coefficients are calculated, is not guaranteed to be convex. The next step is to use this analytical expression as a tool to obtain further data points, referred as 'interpolated points' from now on. These interpolated points are used as input for the resolution of the sum of squares convex optimization problem following Suryasentana et al. 2019

3. The interpolated points are standardized in a way that for uniaxial loading conditions their values are 1 (for the positive loading direction) and -1 (for the negative loading direction). For every set of data (sections M1, M2, M3, M4) two distinct sum of squares convex failure envelopes of the standardized loading variables of degree 4 and 6 are then selected, for which the coefficients need to be identified (Eq. 2.16 and Eq. 2.14). The polynomial expression of degree 4 is given by:

$$f_4 = \sum_{\substack{i,j,k=0 \\ |i+j+k|=4}}^{4} a_{I(i,j,k)} \bar{N}^i \bar{M}^j \bar{V}^k - 1 \tag{2.16}$$

and is equivalent to:

$$f_4 = a_1\bar{N}^4 + a_2\bar{N}^3\bar{M} + a_3\bar{N}^2\bar{M}^2 + a_4\bar{N}\bar{M}^3 + a_5\bar{M}^4 + a_6\bar{N}^3\bar{V} + a_7\bar{N}^2\bar{M}\bar{V} + a_8\bar{N}\bar{M}^2\bar{V} + a_9\bar{M}^3\bar{V} + a_{10}\bar{N}^2\bar{V}^2 + a_{11}\bar{N}\bar{M}\bar{V}^2 + a_{12}\bar{M}^2\bar{V}^2 + a_{13}\bar{N}\bar{V}^3 + a_{14}\bar{M}\bar{V}^3 + a_{15}\bar{V}^4 - 1 \quad (2.17)$$

The coeffcients of all monomials containing a single loading variable are 1 as long as the uniaxial loading conditions are applied.

4. Finally, the objective function is minimized, subjected to the condition of positive semi-definite Hessian. Thus, the coefficients of all monomials are obtained for every set of data (sections M1, M2, M3, M4).

The coefficients of the monomials for all the tested sections are presented in Tables 2.6-2.9 for the expression of degree 4 and in Tables 2.10-2.13 for the expression of degree 6.

a_1	a_2	a_3	a_4	a_5
1	0	5.7	0.01	1
a_6	a_7	a_8	a_9	a_{10}
0.01	-4.18	-0.01	-2.34	3.24
a_{11}	a_{12}	a_{13}	a_{14}	a_{15}
0.02	4.71	-0.01	-3.49	1

Table 2.6: M1 section: Coefficients of monomials for the failure envelope expression of degree 4.

a_1	a_2	a_3	a_4	a_5
1	0	5.87	0	1
a_6	a_7	a_8	a_9	a_{10}
0.01	-5.26	-0.01	2.36	3.9
a_{11}	a_{12}	a_{13}	a_{14}	a_{15}
0.02	4.81	-0.02	-3.5	1

Table 2.7: M2 section: Coefficients of monomials for the failure envelope expression of degree 4.

a_1	a_2	a_3	a_4	a_5
1	0	5.58	0.01	1
a_6	a_7	a_8	a_9	a_{10}
-0.01	-2.67	-0.03	-2.19	1.23
a_{11}	a_{12}	a_{13}	a_{14}	a_{15}
0.04	4.76	-0.01	-3.45	1

Table 2.8: M3 section: Coefficients of monomials for the failure envelope expression of degree 4.

a_1	a_2	a_3	a_4	a_5
1	-0.01	5.88	0.02	1
a_6	a_7	a_8	a_9	a_{10}
0.01	-3.59	-0.06	-1.8	3.18
a_{11}	a_{12}	a_{13}	a_{14}	a_{15}
0.05	4.25	-0.03	-3.28	1

Table 2.9: M4 section: Coefficients of monomials for the failure envelope expression of degree 4.

a_1	a_2	a_3	a_4	a_5	a_6	a_7
1	0	13.22	0.05	10.07	0.02	1
a_8	a_9	a_{10}	a_{11}	a_{12}	a_{13}	a_{14}
0.01	-9.44	-0.04	-10.43	-0.04	-3.39	6.79
a_{15}	a_{16}	a_{17}	a_{18}	a_{19}	a_{20}	a_{21}
-0.04	25.72	0.08	10.89	0.01	-17.33	-0.11
a_{22}	a_{23}	a_{24}	a_{25}	a_{26}	a_{27}	a_{28}
-15.40	4.56	0.07	12.65	-0.02	-5.5	1

Table 2.10: M1 section: Coefficients of monomials for the failure envelope expression of degree 6.

a_1	a_2	a_3	a_4	a_5	a_6	a_7
1	0	14.03	0.03	12.26	0.02	1
a_8	a_9	a_{10}	a_{11}	a_{12}	a_{13}	a_{14}
0.01	-12.73	0	-17.97	-0.06	-3.34	8.29
a_{15}	a_{16}	a_{17}	a_{18}	a_{19}	a_{20}	a_{21}
-0.05	35.83	0.13	11.09	0	-22.46	-0.18
a_{22}	a_{23}	a_{24}	a_{25}	a_{26}	a_{27}	a_{28}
15.42	5.56	0.1	12.69	-0.02	-5.51	1

Table 2.11: M2 section: Coefficients of monomials for the failure envelope expression of degree 6.

a_1	a_2	a_3	a_4	a_5	a_6	a_7
1	0.02	12.56	0.02	9.41	0.02	1
a_8	a_9	a_{10}	a_{11}	a_{12}	a_{13}	a_{14}
-0.02	-9.38	-0.01	-6.44	-0.06	-3.27	5.34
a_{15}	a_{16}	a_{17}	a_{18}	a_{19}	a_{20}	a_{21}
-0.03	10.68	0.09	11.17	0	-4.31	-0.11
a_{22}	a_{23}	a_{24}	a_{25}	a_{26}	a_{27}	a_{28}
-15.26	0.48	0.06	12.56	-0.01	-5.44	1

Table 2.12: M3 section: Coefficients of monomials for the failure envelope expression of degree 6.

a_1	a_2	a_3	a_4	a_5	a_6	a_7
1	0	11.76	0.09	8.58	0.03	1
a_8	a_9	a_{10}	a_{11}	a_{12}	a_{13}	a_{14}
0	-10.18	-0.15	-2.36	-0.08	-2.11	7.74
a_{15}	a_{16}	a_{17}	a_{18}	a_{19}	a_{20}	a_{21}
0.04	16.67	0.14	8.54	-0.02	-12.25	-0.18
a_{22}	a_{23}	a_{24}	a_{25}	a_{26}	a_{27}	a_{28}
-12.57	3.68	0.1	11.07	-0.02	-5.14	1

Table 2.13: M4 section: Coefficients of monomials for the failure envelope expression of degree 6.

2.6.3 Comparison of the different analytical expressions at failure (3^d characteristic state)

In order to choose the analytical expression of the failure envelope for a given reinforced concrete section, 2D sections of the failure envelope in the moment - axial force, shear force - moment and shear force - axial force planes, together with the data obtained by the numerical simulations and the interpolated data for the RC section M3 are presented in Figures 2.30, 2.31, 2.32. It can be clearly seen that the polynomial of degree 6 gives a better approximation of the failure envelope. In particular, the sum of squares convex optimization problem is solved for the RC section M3 with an overall precision of $1.1\,\mathrm{e}^{-6}$ for the polynomial of degree 4 and a precision of $9.4\,\mathrm{e}^{-10}$ for the polynomial of degree 6.

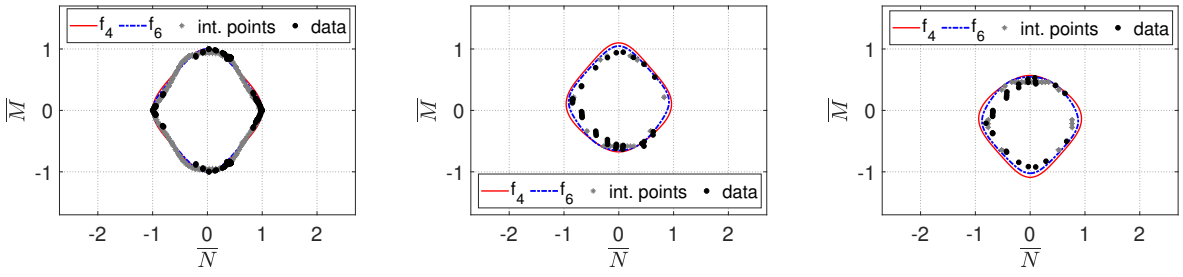

(a) $\bar{V}$=0 (b) $\bar{V}$=0.4 (c) $\bar{V}$=-0.5

Figure 2.30: M3 section: Moment - axial force interaction diagrams obtained by polynomials f_4, f_6 compared to data by numerical simulations and interpolated points.

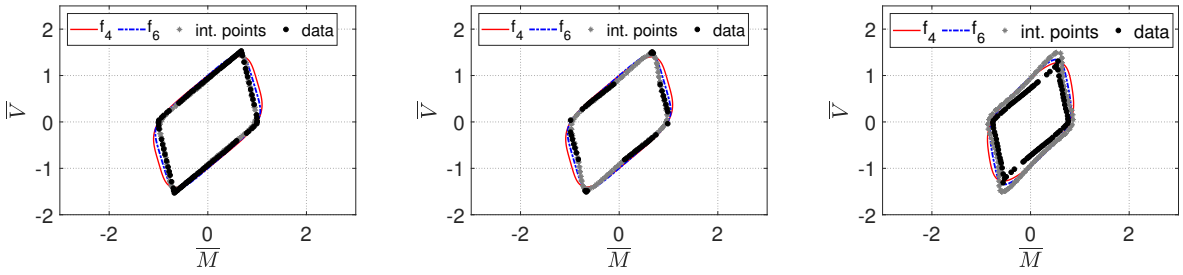

(a) $\bar{N}$=0 (b) $\bar{N}$=0.1 (c) $\bar{N}$=-0.4

Figure 2.31: M3 section: Moment - shear force interaction diagrams obtained by polynomials f_4, f_6 compared to data by numerical simulations and interpolated points.

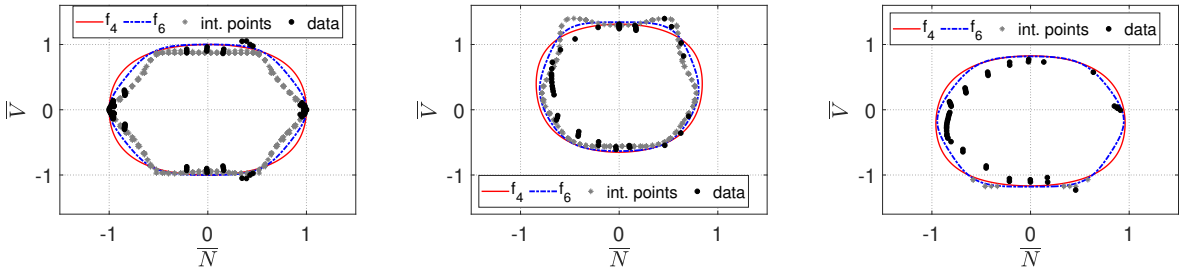

(a) $\bar{M}$=0 (b) $\bar{M}$=0.4 (c) $\bar{M}$=-0.2

Figure 2.32: M3 section: Axial force - shear force interaction diagrams obtained by polynomials f_4, f_6 compared to data by numerical simulations and interpolated points.

The results for the M1, M2 and M4 sections are included in the Annex and conclusions are similar. For the RC section M1, the precision of the resolution of the sum of squares convex optimization problem is $5.9\,\mathrm{e}^{-7}$ for the polynomial of degree 4 (f_4) and $5.1\,\mathrm{e}^{-9}$ for the polynomial of degree 6 (f_6). For the RC section M2, the precision is $1.1\,\mathrm{e}^{-6}$ for the polynomial of degree 4 and $5.1\,\mathrm{e}^{-10}$ for the polynomial of degree 6 and for the RC section M4, the precision is $1.2\,\mathrm{e}^{-7}$ for the polynomial of degree 4 and $5.8\,\mathrm{e}^{-10}$ for the polynomial of degree 6.

Figure 2.33 presents the failure envelope of degree 6 in the 3D space of the RC section M1, M2, M3 and M4.

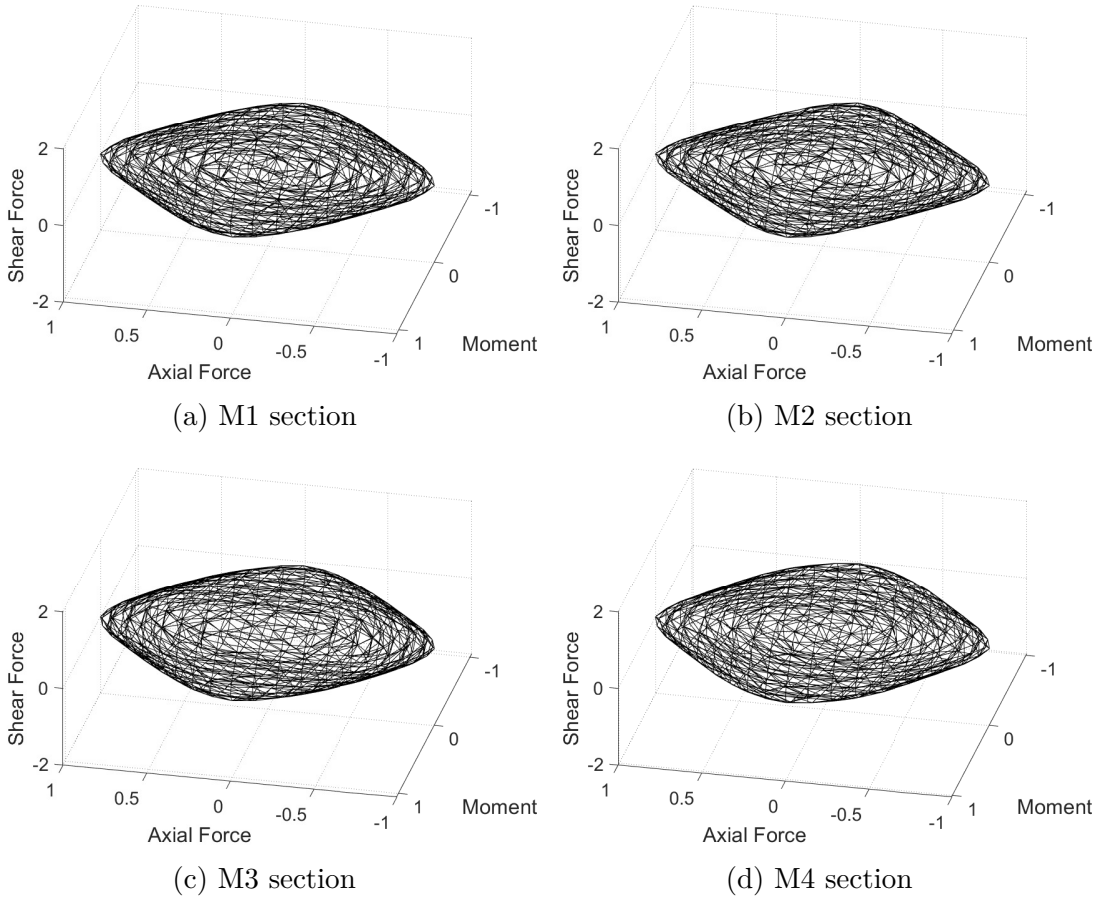

(a) M1 section (b) M2 section

(c) M3 section (d) M4 section

Figure 2.33: Failure envelope of degree 6 in 3D standardized space for the RC sections M1, M2, M3 and M4.

2.6.4 Analytical expressions at 2^{nd} characteristic state

The procedure to compute the analytical expression of the interaction diagram for the 2^{nd} characteristic state is slightly different than the one of section 2.6.3. More specifically, the interaction diagram for the 2^{nd} characteristic state (Figure 2.26) has a similar form to the one for the 3^d characteristic state (Figure 2.27). However, the centers of the two surfaces present an offset. The proposed analytical expression for the 2^{nd} characteristic state is therefore the same as Equation (2.14) but the standardized variables $\bar{N}$, $\bar{M}$, $\bar{V}$ are replaced by $\frac{\bar{N}-\bar{N}_0}{\bar{N}^*}$, $\frac{\bar{M}-\bar{M}_0}{\bar{M}^*}$, $\frac{\bar{V}-\bar{V}_0}{\bar{V}^*}$ respectively in order to modify the center and the radii of the ellipsoid. The analytical expression for the 2^{nd} characteristic state is given by Equation (2.18) for which the coefficients of all monomials are already calculated and presented in Tables 2.10-2.13 for the RC sections M1, M2, M3 and M4.

$$f_6 = \sum_{\substack{i,j,k=0 \\ |i+j+k|=6}}^{6} a_{I(i,j,k)} \left(\frac{\bar{N} - \bar{N}_0}{\bar{N}^*} \right)^i \left(\frac{\bar{M} - \bar{M}_0}{\bar{M}^*} \right)^j \left(\frac{\bar{V} - \bar{V}_0}{\bar{V}^*} \right)^k - 1 \tag{2.18}$$

Each set of data points that correspond to the 1^{st} characteristic state (Figure 2.26) are subsequenlty introduced in Equation (2.18). The center ($\bar{N}_0$, $\bar{M}_0$, $\bar{V}_0$) and the radii ($\bar{N}^*$, $\bar{M}^*$, $\bar{V}^*$) of the ellipsoid corresponding to the 2^{nd} characteristic state are calculated by the resolution of a nonlinear least squares optimization problem. The obtained values for the RC sections M1, M2, M3 and M4 are presented in Table 2.14. Figure 2.34 presents both characteristic states (2^{nd} and 3^d) of degree 6 in the 3D space for the RC sections M1, M2, M3 and M4.

RC section	$\bar{N}_0$	$\bar{M}_0$	$\bar{V}_0$	$\bar{N}^*$	$\bar{M}^*$	$\bar{V}^*$
M1	-0.0117	0.0000	-0.0003	0.7435	0.6096	0.6366
M2	-0.0346	0.0000	-0.0002	0.7783	0.8598	0.9427
M3	-0.1101	0.0001	0.0000	0.7590	0.8236	0.8517
M4	-0.0505	0.0001	0.0000	0.7658	0.8751	0.9514

Table 2.14: Center and radii of the ellipsoid corresponding to the 2^{nd} characteristic state.

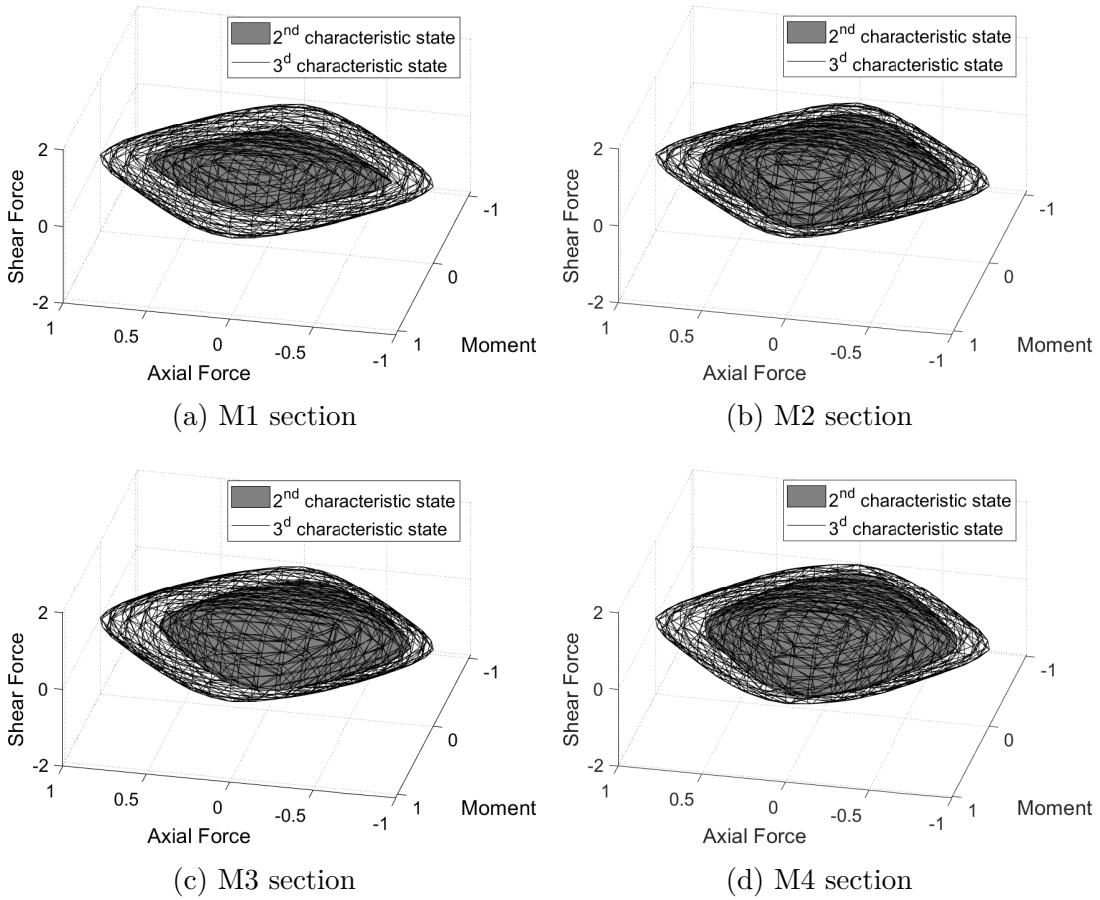

(a) M1 section (b) M2 section

(c) M3 section (d) M4 section

Figure 2.34: 2^{nd} and 3^{d} characteristic states of degree 6 in 3D standardized space for the RC sections M1, M2, M3 and M4.

2.6.5 Analytical expressions at 1^{st} characteristic state

The procedure to compute the analytical expression of the interaction diagram for the 1^{st} characteristic state is similar to the one of section 2.6.4. The interaction diagram for the 1^{st} characteristic state has a similar form to the one for the 3^{d} characteristic state as it is shown in Figure 2.35.

The analytical expression for the 1^{st} characteristic state results again from Equation (2.14) but the standardized variables $\bar{N}$, $\bar{M}$, $\bar{V}$ are replaced by $\frac{\bar{N}}{\bar{N}^*}$, $\frac{\bar{M}}{\bar{M}^*}$, $\frac{\bar{V}}{\bar{V}^*}$ respectively, thus modifying only the radii of the ellipsoid. The analytical expression for the 1^{st} characteristic state is given by Equation (2.19) for which the coefficients of all monomials are already calculated and presented in Tables 2.10-2.13 for the RC sections M1, M2, M3 and M4.

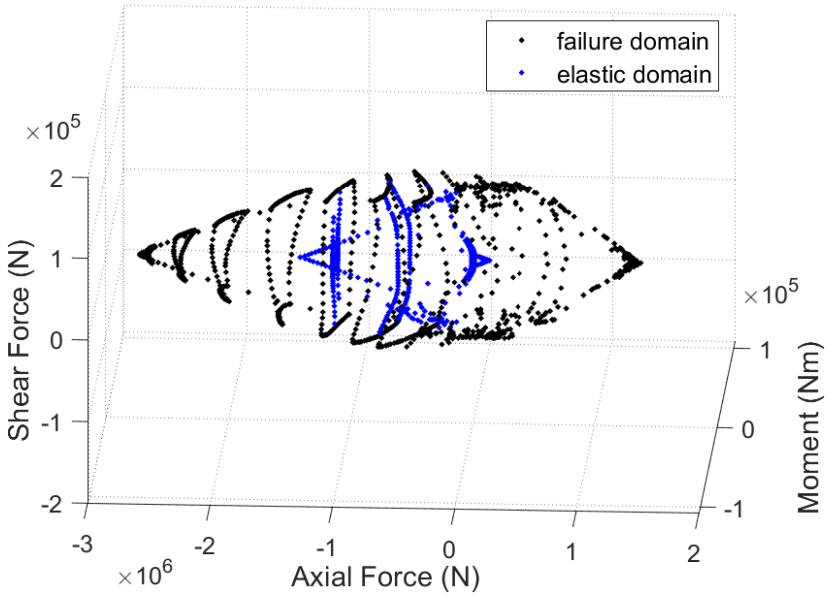

Figure 2.35: Interaction diagrams (discrete points) for M3 section (initial validated model: 1^{st} characteristic state ('elastic domain') and 3^d characteristic state ('failure').

$$f_6 = \sum_{\substack{i,j,k=0 \\ |i+j+k|=6}}^{6} a_{I(i,j,k)} \left(\frac{\bar{N}}{\bar{N}^*}\right)^i \left(\frac{\bar{M}}{\bar{M}^*}\right)^j \left(\frac{\bar{V}}{\bar{V}^*}\right)^k - 1 \tag{2.19}$$

Each set of data points that correspond to the 1^{st} characteristic state (Figure 2.35) are subsequenlty introduced in Equation (2.19). The radii ($\bar{N}^*$, $\bar{M}^*$, $\bar{V}^*$) of the ellipsoid corresponding to the 1^{st} characteristic state are approximately estimated by the use of resolution of a nonlinear least squares optimization problem. The obtained values for the RC sections M1, M2, M3 and M4 are presented in Table 2.15. Figure 2.36 presents both characteristic states (1^{st} and 3^d) of degree 6 in the 3D space for the RC sections M1, M2, M3 and M4.

RC section	$\bar{N}^*$	$\bar{M}^*$	$\bar{V}^*$
M1	0.45	0.45	0.50
M2	0.50	0.55	0.55
M3	0.50	0.65	0.65
M4	0.50	0.80	0.70

Table 2.15: Radii of the ellipsoid corresponding to the 1^{st} characteristic state.

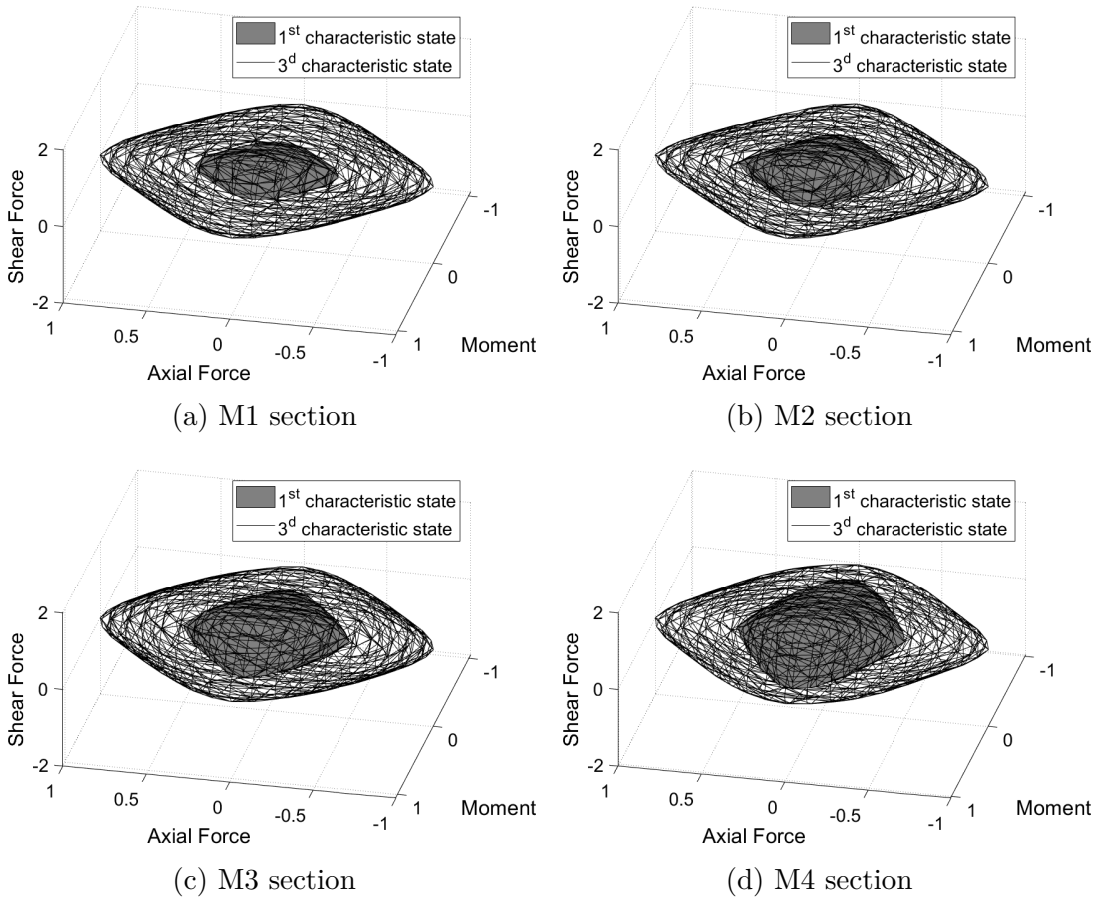

(a) M1 section

(b) M2 section

(c) M3 section

(d) M4 section

Figure 2.36: 1^{st} and 3^{d} characteristic states of degree 6 in 3D standardized space for the RC sections M1, M2, M3 and M4.

2.6.6 Summary of the steps for the calculation of the analytical expressions of the three characteristic states

The general procedure for the derivation of the analytical expressions of the two characteristic states is briefly summarized in the following steps:

- enrichment of the data points of the 3^{d} characteristic state from the numerical simulations;
- standardization of the enriched data points of the 3^{d} characteristic state;
- resolution of the sum of squares convex optimization problem for the chosen homogeneous polynomial expressions in order to obtain the coefficients of all monomials;

- standardization of the data points of the 2^{nd} characteristic state from the numerical simulations. These data are used as input in the next step;
- computation of the analytical expression of the 2^{nd} characteristic state using the same expression of the 3^{d} characteristic state by changing the center and the radii of the ellipsoid.
- standardization of the data points of the 1^{st} characteristic state from the numerical simulations. These data are used as input in the following step;
- computation of the analytical expression of the 1^{nd} characteristic state using the same expression of the 3^{d} characteristic state by changing the radii of the ellipsoid.

2.7 Summary

In this Chapter a numerical methodology is presented on the construction of failure envelopes for given symmetrically RC square sections with various reinforcement ratios. Suitable constitutive models are first chosen for the description of the material behavior, both for concrete and steel. The choice of a 3D finite element modeling leads to more precise results as there are no kinematic assumptions as in classical beam finite element calculations. Finally, a methodology is provided to derive analytical expressions of three characteristics states based on the numerical results. This study concerning the construction of interaction diagrams at the 2^{nd} and the 3^{d} characteristic states is also found in Doulgeroglou et al. 2022.

Further investigating factors, such as steel strength, concrete compressive strength, consideration of non-perfect bonding between concrete and steel, ratio and position of the transversal reinforcement, section geometry and shape should be examined in order to provide more complete interaction diagrams. The 3D calculations are however extremely costly, as more than 1428000 core hours of computational time were necessary to obtain the presented interaction diagrams. Calculations took place using the supercomputer Liger of the Centrale Nantes SuperComputing Center (Liger 2016). Liger is a BULL/Atos DLC720 cluster of 252 compute nodes and 14 visualization nodes with 24 cores per node and a total compute memory of 36608GB. Some first results on the influence of the section shape are for example given hereafter.

Influence of the section shape

In the following, rectangular, orthogonal and circular sections are studied having equal areas and reinforcement ratios the same as M3 section. The meshes of these sections are presented in Figure 2.37.

Radial displacement imposed loads are imposed by keeping the ratio of axial displacement to transversal displacement of each loading combination constant. In Figure 2.38 the loading paths in the moment - axial force plane are presented for the different types of section tested. The results are similar, independent of the section form. This is a positive indication for the possibility to generalize the failure surface. This work is under progress as more loading combinations must be tested to study the influence of the form of the section on the failure envelope.

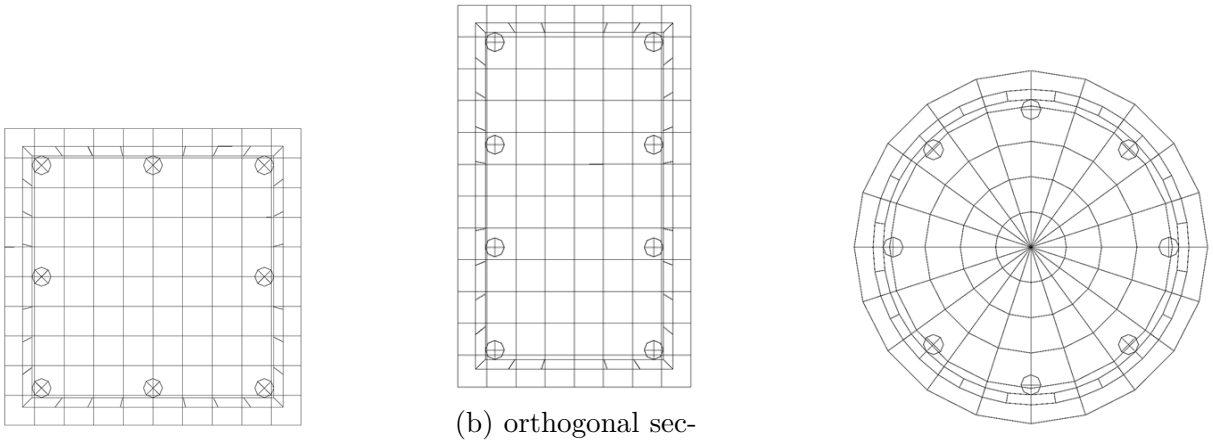

(a) rectangular section

(b) orthogonal section

(c) circular section

Figure 2.37: Different sections of equal areas and reinforcing ratios.

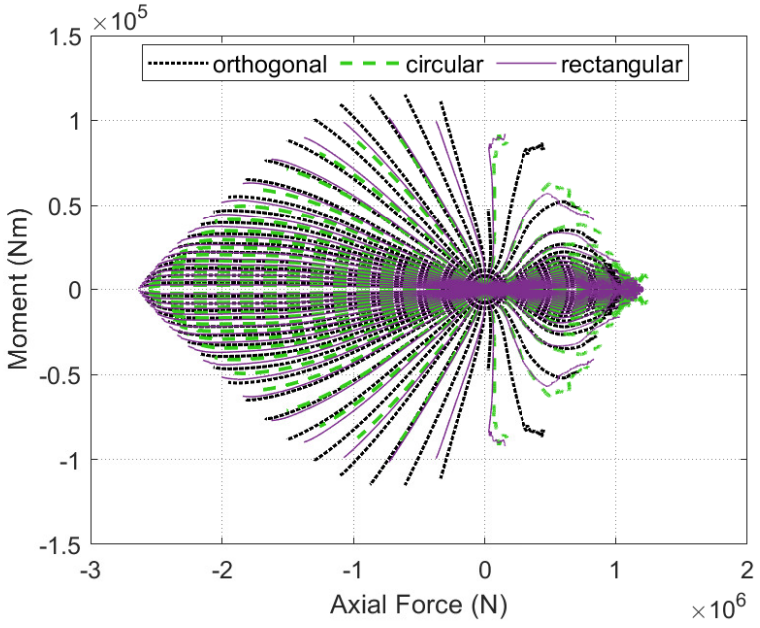

Figure 2.38: Moment - axial force interaction diagrams for orthogonal, circular and rectangular sections of equal areas and reinforcing ratios.

Chapter 3

Macroelement modelling

3.1 Different types of macroelements

Introduced in geomechanics by Nova and Montrasio (Nova and Montrasio 1991), the macroelement considers the global behavior of the foundation and of the soil volume interacting with it "lumped" into a single, integral, 3D constitutive equation linking the evolution of the resultant loads/moments on the foundation to the corresponding displacements/rotations histories. For dynamic Soil Structure Interaction problems (SSI), the nonlinear behavior of the soil and the (more often linear elastic) behavior of the foundation are considered concentrated on the "near field", while elasticity and radiation damping are considered on the "far field" (Figure 3.1). Subsequent developments of macroelements for SSI can for example be found in the work of Cremer et al. 2000, Chatzigogos et al. 2009, Grange et al. 2009a for shallow foundations, Li et al. 2014, Li et al. 2016, Li et al. 2018 for piles and Jin et al. 2019 for caisson foundations respectively, following either the elasto-plasticity or hypoplasticity computational framework.

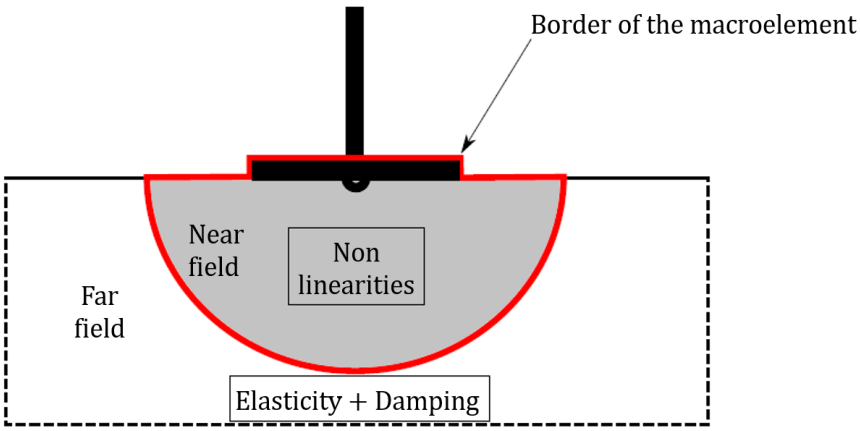

Figure 3.1: The macroelement concept for SSI problems (Grange 2008).

In structural mechanics, the macroelement concept has been applied to describe the nonlinear response of an RC element in terms of global variables forces/moments – displacements/rotations (Elachachi 1992) and the parameter identification results from analysis at a local level (see for example Elachachi 1992, Davenne and Brenet 1998). At the same engineering field, the word macroelement is more often used for uniaxial (uncoupled) nonlinear springs. For instance, Tajiri et al. 2006 introduced a macroelement consisting of axial springs, representing concrete, reinforcements and the bond slip behavior (see Figure 3.2) providing the constitutive relationship between four nodes with three degrees of freedom (two translations and one rotation) for reinforced beam-column joints.

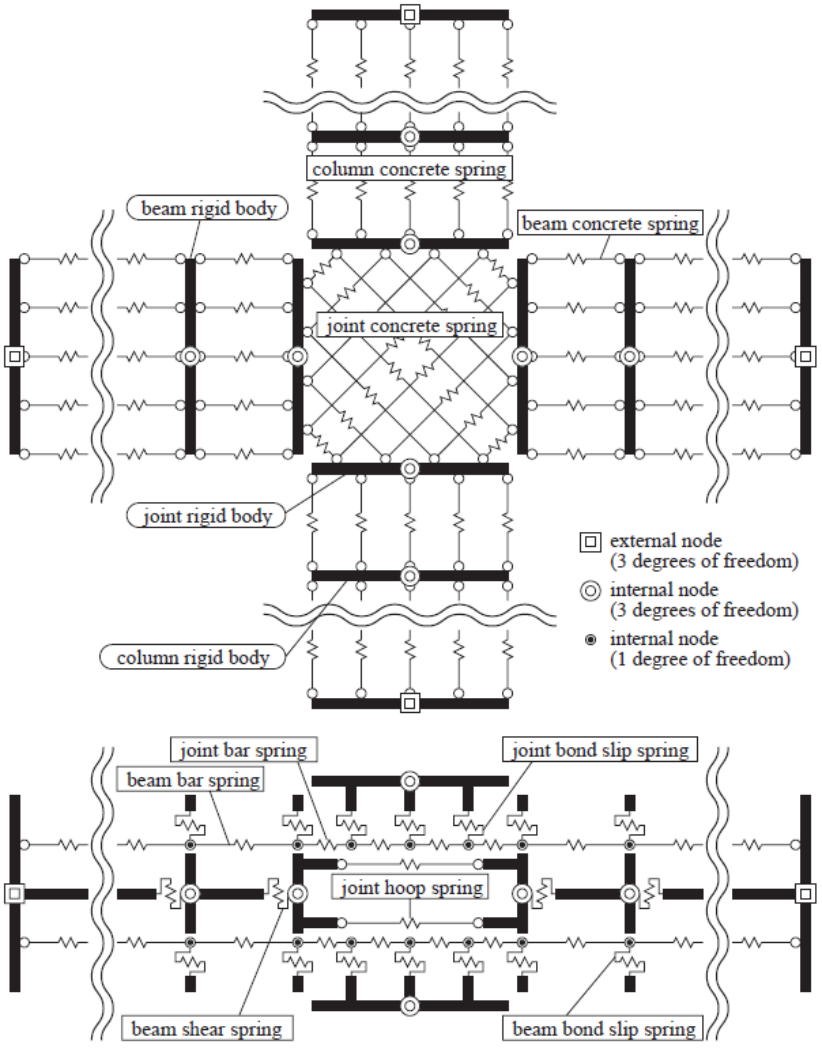

Figure 3.2: Macroelement representation for reinforced beam-column joints (Tajiri et al. 2006).

Hemsas et al. 2009 used the macroelement concept to reproduce the flexural behavior of RC walls. Each macroelement consists of sub-elements charcterized by a uniaxial stiffness, assembled in parallel between the floors (see Figure 3.3), the latter assumed infinitely rigid. The shear behavior is taken into account by a nonlinear horizontal spring such that the relative rotation of the macroelement occurs around a point defined on the central axis. The behavior is described in terms of forces-displacements.

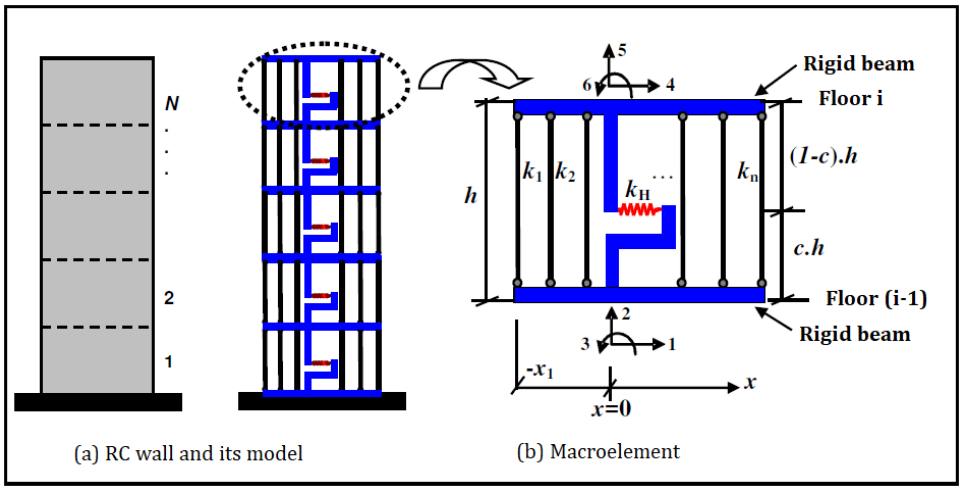

Figure 3.3: Macroelement representation for RC walls (Hemsas et al. 2009).

In Pantò et al. 2015, two macroelements are used for the simulation of the nonlinear in-plane behavior of unreinforced masonry walls. The first one, initially proposed by Raka et al. 2015, uses piers and spandrels, connected by rigid nodes, resulting to an equivalent frame model with a fiber section (see Figure 3.4). The constitutive modeling is described by uniaxial consitutive models. The second macroelement initially proposed by Caliò et al. 2012 is represented by an articulated quadrilateral constituted by four rigid edges connected by four hinges and two diagonal nonlinear springs (see Figure 3.5). Panels interact between them by interface nonlinear springs. This mechanical scheme allows to capture different collapse mechanisms, such as flexural, diagonal shear and sliding shear failure.

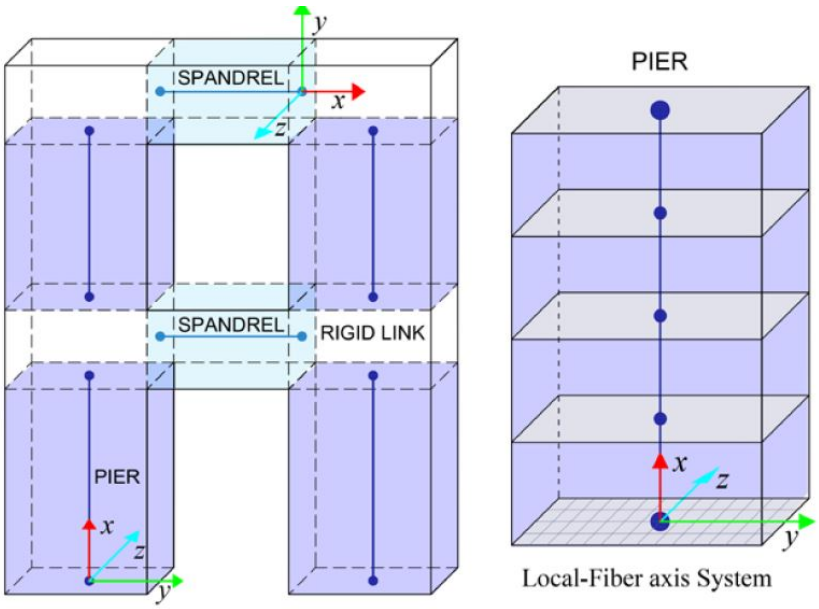

Figure 3.4: Macroelement by piers and spandrels and fiber section subdivision (Pantò et al. 2015).

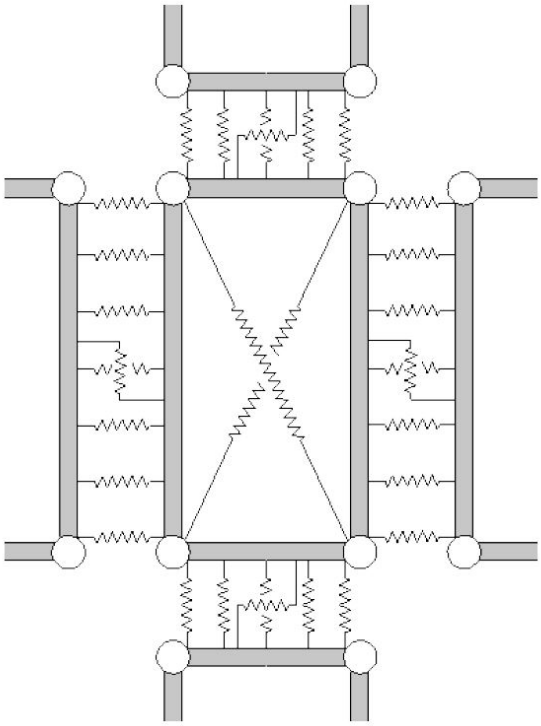

Figure 3.5: Macroelement for UnReinforced Masonry (URM) buildings (Pantò et al. 2015).

3.2 A novel macroelement for RC beam-columns

A novel macroelement for RC beams and RC columns is introduced hereafter. The proposed macroelement adopts the original definition of Nova and Montrasio 1991 and is introduced as a 3D constitutive equation linking the evolution of the resultant loads/moments to the corresponding generalized strains histories at the level of a Timoshenko homogeneous beam section (stress-resultant model). The constitutive description of the section is based on the results of Chapter 2 and more particular the analytical expressions of the interaction diagrams within an elasto-plastic computational framework. Section 3.2.1 briefly presents the Timoshenko beam finite element formulation and section 3.2.2 the stress-resultant elasto-plastic model.

3.2.1 A Timoshenko finite element beam

A 2D Timoshenko beam is shown in Figure 3.6. The displacement vector field $u_P = (u_x, u_y)$ of a point is expressed in terms of the generalized displacement vector $U_G = (U_x, U_y)$ of the barycenter of the section and the rotation Θ of the section as follows (Guedes et al. 1994; Pegon 1994):

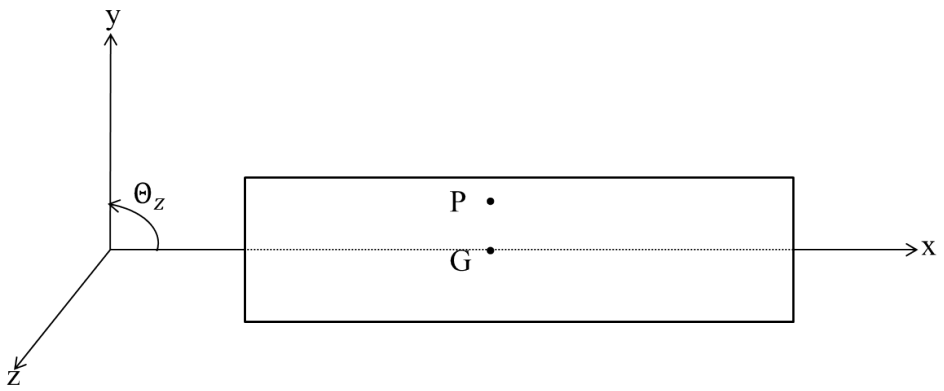

Figure 3.6: 2D Timoshenko beam.

$$u_P = U_G + \Theta \wedge GP \tag{3.1}$$

or using the components:

$$\begin{aligned} u_x(x,y) &= U_x(x) - y\Theta_z(x) \\ u_y(x,y) &= U_y(x) \end{aligned} \tag{3.2}$$

Using the small strain assumption the strain components are given by:

$$\begin{aligned} \varepsilon_x &= \frac{\partial u_x}{\partial x} = U'_x(x) - y\Theta'_z(x) \\ \gamma_{xy} &= \frac{\partial u_y}{\partial x} + \frac{\partial u_x}{\partial y} = U'_y(x) - \Theta_z(x) = \beta_y \neq 0 \end{aligned} \tag{3.3}$$

where prime indicates derivative with respect to x.

Consider now a 2D beam finite element of length L_e, with two nodes i and j and three degrees of freedom per node: axial displacement (U_{xi} and U_{xj}), transversal displacement (U_{yi} and U_{yj}) and rotation (Θ_{zi} and Θ_{zj}), see Figure 3.7.

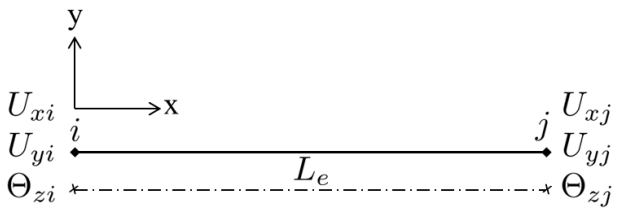

Figure 3.7: 2-node finite element Timoshenko beam

The generalised displacement vector $\underline{U_s}$ is expressed in function of the nodal displacement vector $\underline{U}$ as follows (Guedes et al. 1994; Pegon 1994):

$$\underline{U_s} = \underline{\underline{N}}\,\underline{U} \tag{3.4}$$

$$\begin{bmatrix} U_x \\ U_y \\ \Theta_z \end{bmatrix} = \begin{bmatrix} N_1^a & 0 & 0 & N_4^a & 0 & 0 \\ 0 & N_2^t & 0 & 0 & N_5^t & 0 \\ 0 & 0 & N_3^\theta & 0 & 0 & N_6^\theta \end{bmatrix} \begin{bmatrix} U_{xi} \\ U_{yi} \\ \Theta_{zi} \\ U_{xj} \\ U_{yj} \\ \Theta_{zj} \end{bmatrix}, \tag{3.5}$$

with:

$$\begin{aligned} N_1^a = N_2^t = N_3^\theta = 1 - \frac{x}{L_e} \\ N_4^a = N_5^t = N_6^\theta = \frac{x}{L_e} \end{aligned} \tag{3.6}$$

with $\underline{\underline{N}}$ the shape functions matrix and the upper indexes a, t, θ denoting the axial, transversal and rotational components respectively. By derivation of the displacement field, and following Equation (3.3) the generalized strain vector $\underline{\varepsilon}_s$ is obtained:

$$\begin{bmatrix} \varepsilon_x \\ \beta_y \\ \kappa_\theta \end{bmatrix} = \begin{bmatrix} U'_x \\ \beta_y \\ \Theta'_z \end{bmatrix} = \begin{bmatrix} U'_x \\ U'_y - \Theta_z \\ \Theta'_z \end{bmatrix} = \underline{\underline{B}}\ \underline{U} \tag{3.7}$$

or

$$\begin{bmatrix} \varepsilon_x \\ \beta_y \\ \kappa_\theta \end{bmatrix} = \begin{bmatrix} -\frac{1}{L_e} & 0 & 0 & \frac{1}{L_e} & 0 & 0 \\ 0 & -\frac{1}{L_e} & -\frac{1}{2} & 0 & \frac{1}{L_e} & -\frac{1}{2} \\ 0 & 0 & -\frac{1}{L_e} & 0 & 0 & \frac{1}{L_e} \end{bmatrix} \begin{bmatrix} U_{xi} \\ V_{yi} \\ \Theta_{zi} \\ U_{xj} \\ V_{yj} \\ \Theta_{zj} \end{bmatrix} \tag{3.8}$$

with $\underline{\underline{B}}$ the shape functions' derivatives matrix with respect to x neglecting the linear terms and ε_x, β_y and κ_θ the axial strain, the shear strain and the curvature, located at the beam axis respectively.

Finally, using the virtual work expression one easily finds the following expressions for the element stiffness and mass matrices and the forces internal vector (Pegon 1994):

$$\underline{\underline{K}}_e = \int_0^{L_e} \underline{\underline{B}}^T\ \underline{\underline{K}}_s\ \underline{\underline{B}}\ dx \tag{3.9}$$

with $\underline{\underline{K}}_s$ the stiffness matrix of the section (see section 3.2.2).

The element mass matrix becomes (Guedes et al. 1994):

$$\underline{\underline{M}}_e = \int_0^{L_e} \underline{\underline{N}}^T\ \underline{\underline{M}}_s\ \underline{\underline{N}}\ dx \tag{3.10}$$

with $\underline{\underline{M}}_s$ the mass matrix of the section given as:

$$\underline{\underline{M}}_s = \begin{bmatrix} M_x & 0 & 0 \\ 0 & M_y & 0 \\ 0 & 0 & M_\theta \end{bmatrix} \tag{3.11}$$

with

$$\begin{aligned} M_x &= \rho S \\ M_y &= \rho S \\ M_\theta &= \rho I \end{aligned} \tag{3.12}$$

ρ being the material density, S the area of the section and I the quadratic moment of the section.

The element nodal forces due to the stress resultants developed in the section are calculated using the following integral:

$$\underline{F}_e = \int_0^{L_e} \underline{\underline{B}}^T \ \underline{F}_s \ dx \tag{3.13}$$

with $\underline{F}_s$ the vector of forces in the section (see section 3.2.2).

Remarks:

- The Timoshenko beam Finite element formulation presented in this section has LInear, independent shape functions $\underline{\underline{N}}$ for the generalized displacement field and it is termed hereafter FLI. It was introduced by Pegon 1994 in the finite element code Cast3M (Cast3M 2019). The linear terms are neglected in the $\underline{\underline{B}}$ matrix and the FLI element has only one integration point at the center as this choice overcomes the shear locking problem (Donea and Lamain 1987; Pegon 1994). Contrary to the Timoshenko beam finite element with higher order shape functions introduced by Caillerie et al. 2015, one FLI finite element is not sufficient to reproduce the exact analytical solution. However, as shown in Bitar et al. 2018a, the precision quickly increases with increasing number of FLI finite elements.

- In most finite element codes, the mass matrix is the one of an Euler-Bernoulli type beam as presented in Equations (3.11)-(3.12) (thus the terms of shear correction intervene only in the stiffness matrix). For the case of a short beam with $L/r \approx 12$ ($r = \sqrt{I/S}$ the radius of gyration of the section and I the moment of inertia), of

full circular section S however, the use of the mass matrix of the Euler-Bernoulli type leads to a relative error of the order of 30% from the fourth mode, whereas the error is almost zero for the mass matrix when shear energy is considered (Corn 1998).

3.2.2 Stress-resultant plasticity model (macroelement)

The constitutive model of the section is expressed in terms of generalized forces - generalized strains and is built within the plasticity framework. The failure surface and the loading surfaces are deduced in Chapter 2 and their convexity is guaranteed.

Elastic behavior

The elastic behavior of the section is defined by:

$$\underline{F}_s = \underline{\underline{K}}_s^{el} \underline{\varepsilon}_s \tag{3.14}$$

where $\underline{F}_s$ is the generalized force vector, $\underline{\varepsilon}_s$ the generalized strain vector (Equation (3.7)) and $\underline{\underline{K}}_s^{el}$ the elastic stiffness matrix of the section, the terms of which are uncoupled as the section is considered homogeneous. More specifically:

$$\underline{F}_s = \begin{bmatrix} F_x \\ F_y \\ M_\theta \end{bmatrix} \quad , \quad \underline{\varepsilon}_s = \begin{bmatrix} \varepsilon_x \\ \beta_y \\ \kappa_\theta \end{bmatrix} \quad , \quad \underline{\underline{K}}_s^{el} = \begin{bmatrix} K_x & 0 & \\ 0 & K_y & 0 \\ 0 & 0 & K_\theta \end{bmatrix} \tag{3.15}$$

with F_x, F_y and M_θ the axial force, the shear force and the in-plane bending moment of the section respectively and K_x, K_y and K_θ the axial, transversal and flexural stiffness of the section.

Plastic behavior

The total generalized strain vector is split into an elastic and a plastic part:

$$\underline{\varepsilon}_s = \underline{\varepsilon}_s^{el} + \underline{\varepsilon}_s^{pl} \tag{3.16}$$

Using Equations (3.14) and (3.16) the incremental form of the generalized force vector

is deduced:

$$\dot{\underline{F}}_s = \underline{\underline{K}}_s^{el}(\dot{\underline{\varepsilon}}_s - \dot{\underline{\varepsilon}}_s^{pl}) \tag{3.17}$$

Failure surface

The failure surface f_U is the homogeneous polynomial expression of degree 6 in the standardized space:

$$f_U = \sum_{\substack{i,j,k=0 \\ |i+j+k|=6}}^{6} a_{I(i,j,k)} \bar{F}_x{}^i \bar{F}_y{}^j \bar{M}_\theta{}^k - 1 \tag{3.18}$$

where i, j, k are the exponents of every component of the monomials and $a_{I(i,j,k)}$ are the coefficients of the monomials already calculated in Chapter 2 via the resolution of the convex optimization problem (3^d characteristic state).

Loading surfaces and hardening evolution laws

The loading surfaces are deduced by the failure surface. In the previous Chapter, the 2^{nd} characteristic state was defined as the yield limit of the steel rebars and had the form of a surface similar to the failure surface but with different center and radii. Nevertheless, this is not the choice made hereafter for the macroelement where the elastic domain should be defined closer to the elastic limit of the concrete; otherwise the elastic limit of the response is overestimated. Consequently, the 1^{st} characteristic state is exploited for the definition of the loading surfaces f_L, which are given by the following expression:

$$f_L = \sum_{\substack{i,j,k=0 \\ |i+j+k|=6}}^{6} a_{I(i,j,k)} \left(\frac{\bar{F}_x}{r_x}\right)^i \left(\frac{\bar{F}_y}{r_y}\right)^j \left(\frac{\bar{M}_\theta}{r_\theta}\right)^k - 1 \tag{3.19}$$

with r_x, r_y, r_θ the different uncoupled hardening laws for each loading (x, y, θ).

The proposed formulation does not integrate a kinematic hardening law, as this would lead to inerpenetration of the failure surface by the loading surface if a tangent rule is not additionally considered. A tangent rule (Prevost 1980), has been used in the previous works of Cremer et al. 2001 and Grange et al. 2008 in order to ensure that the final loading point belongs to the failure surface by limiting the kinematic hardening variables. In these cases the failure surface is of 2^{nd} degree and by a change of variables the surfaces reduce to circles; therefore tangency of loading surfaces and failure surface is guaranteed. Given the complexity of the failure surface of the proposed macroelement of this work (polynomial

of degree 6 with coupled terms), there arises the difficulty of deducing a tangent rule, justifying the absence of a kinematic hardening rule.

The proposed hardening evolution laws are expressed as exponential functions which tend asymptotically to unity. This choice is beneficial as it presents two advantages; firstly, it can represent the global response of a RC element up to peak that has an exponential form and secondly it excludes the non-interpenetration of the failure surface by the loading surface. The expression of the hardening evolution laws of the proposed macroelement are given by:

$$\underline{r} = \begin{bmatrix} r_x \\ r_y \\ r_\theta \end{bmatrix} = \begin{bmatrix} 1 + (r_{x0} - 1)e^{-a_x p_x} \\ 1 + (r_{y0} - 1)e^{-a_y p_y} \\ 1 + (r_{\theta 0} - 1)e^{-a_\theta p_\theta} \end{bmatrix} \tag{3.20}$$

with r_{x0}, r_{y0}, $r_{\theta 0}$ defining the initial domain of elasticity in the standardized space and a_x, a_y, a_θ corresponding to the parameters that control the rate of the hardening evolution and depend on the material. Finally, p_x, p_y, p_θ are the internal hardening variables and are non negative functions of the cumulative plastic flow of each loading direction. The evolution of these variables is defined simply as follows:

$$\underline{p} = \begin{bmatrix} p_x \\ p_y \\ p_\theta \end{bmatrix} \quad , \quad \underline{\dot{p}} = \begin{bmatrix} \dot{p}_x \\ \dot{p}_y \\ \dot{p}_\theta \end{bmatrix} = \begin{bmatrix} |\dot{\varepsilon_x}^{pl}| \\ |\dot{\beta_y}^{pl}| \\ |\dot{\kappa_\theta}^{pl}| \end{bmatrix} \tag{3.21}$$

Plastic potential function and normality condition

An associative Levy-Saint Venant plastic flow rule is assumed and thus the plastic potential function is identical to the yield function. Via the normality condition the plastic generalized strain evolution is subsequently computed as:

$$\underline{\dot{\varepsilon}}_s^{pl} = \dot{\lambda} \frac{\partial f_L}{\partial \underline{F}_s} \Leftrightarrow \begin{bmatrix} \dot{\varepsilon_x}^{pl} \\ \dot{\beta_y}^{pl} \\ \dot{\kappa_\theta}^{pl} \end{bmatrix} = \dot{\lambda} \begin{bmatrix} \frac{\partial f_L}{\partial F_x} \\ \frac{\partial f_L}{\partial F_y} \\ \frac{\partial f_L}{\partial M_\theta} \end{bmatrix} \tag{3.22}$$

Combining Equations (3.20) and (3.22) the 1^{st} order differential equations of the different hardenings are expressed by:

$$\underline{\dot{r}} = \begin{bmatrix} \dot{r}_x \\ \dot{r}_y \\ \dot{r}_\theta \end{bmatrix} = \begin{bmatrix} a_x(1-r_x)\dot{p}_x \\ a_y(1-r_y)\dot{p}_y \\ a_\theta(1-r_\theta)\dot{p}_\theta \end{bmatrix} = \dot{\lambda} \underbrace{\begin{bmatrix} a_x(1-r_x)\left|\frac{\partial f_L}{\partial F_x}\right| \\ a_y(1-r_y)\left|\frac{\partial f_L}{\partial F_y}\right| \\ a_\theta(1-r_\theta)\left|\frac{\partial f_L}{\partial M_\theta}\right| \end{bmatrix}}_{\underline{h}_L(\underline{F}_s,\underline{r})} \tag{3.23}$$

where $\underline{h}_L(\underline{F}_s, \underline{r})$ is the vectorial expression of the hardening.

Persistency condition

During plastic flow, in order to ensure nonzero $\underline{\dot{\varepsilon}}_s^{pl}$, $\dot{\lambda}$ must be positive and the actual stress point must remain on the boundary of the yield function i.e. $f_L = 0$ (Simo and Hughes 2006). The persistency condition corresponds to these requirements and is given by:

$$\dot{\lambda}\dot{f}_L = 0 \quad (if \quad f_L = 0) \tag{3.24}$$

The persistency condition is used for the calculation of the plastic multiplier $\dot{\lambda}$ as follows. Equation (3.24) implies:

$$\dot{f}_L = 0 \Leftrightarrow \frac{\partial f_L}{\partial \underline{F}_s}\underline{\dot{F}}_s + \frac{\partial f_L}{\partial \underline{r}}\underline{\dot{r}} = 0 \tag{3.25}$$

Combination of Equations (3.25) and (3.17) results in:

$$\begin{aligned} &\frac{\partial f_L}{\partial \underline{F}_s}\underline{\underline{K}}_s^{el}(\underline{\dot{\varepsilon}}_s - \underline{\dot{\varepsilon}}_s^{pl}) + \frac{\partial f_L}{\partial \underline{r}}\underline{\dot{r}} = 0 \Leftrightarrow \\ &\frac{\partial f_L}{\partial \underline{F}_s}\underline{\underline{K}}_s^{el}\underline{\dot{\varepsilon}}_s - \frac{\partial f_L}{\partial \underline{F}_s}\underline{\underline{K}}_s^{el}\underline{\dot{\varepsilon}}_s^{pl} + \frac{\partial f_L}{\partial \underline{r}}\underline{\dot{r}} = 0 \Leftrightarrow \\ &\frac{\partial f_L}{\partial \underline{F}_s}\underline{\underline{K}}_s^{el}\underline{\dot{\varepsilon}}_s - \frac{\partial f_L}{\partial \underline{F}_s}\underline{\underline{K}}_s^{el}\dot{\lambda}\frac{\partial f_L}{\partial \underline{F}_s} + \frac{\partial f_L}{\partial \underline{r}}\dot{\lambda}\underline{h}_L = 0 \Leftrightarrow \\ &\dot{\lambda} = \frac{\frac{\partial f_L}{\partial \underline{F}_s}\underline{\underline{K}}_s^{el}\underline{\dot{\varepsilon}}_s}{\frac{\partial f_L}{\partial \underline{F}_s}\underline{\underline{K}}_s^{el}\frac{\partial f_L}{\partial \underline{F}_s} - \frac{\partial f_L}{\partial \underline{r}}\underline{h}_L} \end{aligned} \tag{3.26}$$

Knowing the analytical expression of the plastic multiplier $\dot{\lambda}$ and using Equations

(3.17), (3.22) and (3.26) the following expression is obtained:

$$\underline{\dot{F}}_s = \underbrace{\left(\underline{\underline{K}}_s^{el} - \frac{\left(\underline{\underline{K}}_s^{el} : \frac{\partial f_L}{\partial \underline{F}_s} \right) \otimes \left(\frac{\partial f_L}{\partial \underline{F}_s} : \underline{\underline{K}}_s^{el} \right)}{\frac{\partial f_L}{\partial \underline{F}_s} \underline{\underline{K}}_s^{el} \frac{\partial f_L}{\partial \underline{F}_s} - \frac{\partial f_L}{\partial \underline{r}} \dot{\lambda} \underline{h}_L} \right)}_{\underline{\underline{K}_s}^{ep,analytical}} \underline{\dot{\varepsilon}}_s \tag{3.27}$$

that gives the analytical elasto-plastic tangent stiffness matrix $\underline{\underline{K_s}}^{ep,analytical}$.

3.3 Parameter identification

As stated in Chapter 2, the stress-resultant forces are standardized such that they are equal to 1 (for the positive loading direction) and -1 (for the negative loading direction) for uniaxial loading conditions. In the standardized space, the failure surface is thus symmetrical with respect to the origin. In the real dimensional space however, the failure surface presents asymmetry with respect to the center of the axes in the axial loading directions. The standardization procedure requires therefore a reference parameter and a shift parameter for the axial component, while for the shear and flexural components only shift parameters are needed.

In Equation (3.18) of the failure surface the axial force $\bar{F}_x$, shear force $\bar{F}_y$ and bending moment $\bar{M}_\theta$ are given in the standardized space. They are defined as:

$$\bar{F}_x = \frac{F_x - F_{x0}}{F_x^*} \quad , \quad \bar{F}_y = \frac{F_y}{F_y^*} \quad , \quad \bar{M}_\theta = \frac{M_\theta}{M_\theta^*} \tag{3.28}$$

with F_{x0} the reference parameter for the axial component and F_x^*, F_y^*, M_θ^* the shift parameters for the axial, shear and flexural components respectively.

The reference parameter F_{x0} is the midpoint between the maximum axial force $F^t_{x,max}$ (tensile force of positive sign) and the minimum axial force $F^c_{x,max}$ (compressive force of negative sign):

$$F_{x0} = (F^t_{x,max} + F^c_{x,max})/2 \tag{3.29}$$

The shift parameter F_x^* is defined as:

$$F_x^* = (F^t_{x,max} - F^c_{x,max})/2 \tag{3.30}$$

The following four (4) parameters thus remain to be to identified:

$$F^t_{x,max}, \quad F^c_{x,max}, \quad F^*_y, \quad M^*_\theta$$

Analytical computation of the maximum axial tensile force $F^t_{x,max}$ corresponding to the characteristic states defined in Section 2.2 is not possible. $F^c_{x,max}$ can be analytically computed given the following material parameters both for concrete and steel: elastic modulus, limit of elasticity, ultimate strength and their corresponding strains. F^*_y and M^*_θ do not coincide with the maximum values of the shear force and bending moment of the failure surface; bending moment reaches its maximum for low levels of axial force and shear force reaches its maximum when coupled to bending moment. Actually, except for uniaxial tension and compression, pure uniaxial loading conditions do not always exist for RC elements. For imposed bending loads and when the elastic limit of the section is reached, axial forces appear (given the asymmetric behavior of concrete in tension and compression); for applied transversal loads, shear is always coupled to flexion.

The identification of the parameters used for the standardization procedure is therefore not straightforward. Despite the complexity of the computation of the standardization parameters other than $F^c_{x,max}$, a simplified procedure is however proposed hereafter.

1. Maximum axial tensile force $F^t_{x,max}$: the ultimate strength of the total number of the steel rebars is considered (Equation (3.31)), even though the numerical calculations of the previous Chapter showed that this assumption is underestimated. Nevertheless, tensile forces especially of large magnitude, are rarely expected in usual RC structures and therefore, it is concluded that this standardization parameter does not affect the precision of the macroelement.

$$F^t_{x,max} = f^{ult}_s A_s \tag{3.31}$$

   where f^{ult}_s is the steel ultimate strength and A_s is the total area of the steel rebars.

2. Maximum axial compressive force $F^c_{x,max}$: the sum of the utlimate strength of the concrete section and the contribution of the steel rebars is used (Equation (3.32)). The latter can be either in the elastic ot the plastic range of the material's response, according to the material properties of the steel.

$$F^c_{x,max} = f_c A_c + f^{cur}_s A_s \tag{3.32}$$

where f_c is the maximum concrete compressive strength, A_c is the area of the concrete section, f_s^{cur} is the steel current stress (in the elastic range or not) and A_s is the total area of the steel rebars.

3. Shift parameter M_θ^*: using the moment-axial force interaction diagrams of Eurocode (CEN 2004), without application of security coefficients, as it was found (see section 2.5) that this choice presents a good fit of the numerical results to the ones obtained by the method of Eurocode.

4. Shift parameter F_y^*: using the method of Rahal (Rahal 2000b) based on a simplification of the Modified Compression Field Theory (MCFT) for pure shear. The shift parameter F_y^* is identified as the ultimate shear strength ν_u multiplied by the effective sectional area ($b_w d_v$) and is provided by the graph of Figure 3.8, given the compressive concrete strength f_c and the adimensional indices ω_L and ω_t: with

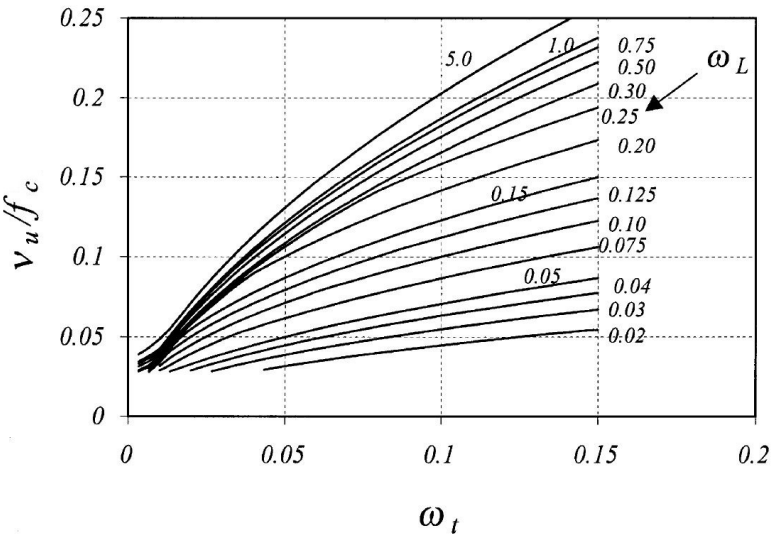

Figure 3.8: Normalized strength curves (Rahal 2000b).

$\omega_L = \dfrac{A_L f_{yL}}{b_w d_v f_c}$ and $\omega_t = \dfrac{A_v f_{yt}}{b_w s f_c}$ where f_{yL} and f_{yt} are the yield strengths of longitudinal and transverse steel respectively, A_L is the total area of symmetrical longitudinal steel, A_v is the area of shear reinforcement within the distance s, which corresponds to the spacing of the stirrups along the length of the beam and b_w and d_v are the effective shear width and depth respectively.

In Equation (3.20), r_{x0}, r_{y0}, $r_{\theta 0}$ define the elasticity domain of the RC section and

their values are selected in the range of $0.35 - 0.8$ (see section 2.6.5). In the same equation, a_x, a_y, a_θ are the parameters of the hardening evolution law. These parameters can be calibrated via numerical simulations at the material level by imposing uniaxial loading conditions. For the case of RC beam-columns however, realistic uniaxial loading conditions can be applied only during tension and compression. For the rest of the cases, bending results to axial forces when the elastic limit is reached and transversal shear loads engender flexural loads. Therefore, calibration of these parameters is more feasible via numerical simulations at the level of the beam finite element (and not at the Gauss point). Given the coupled relationship between the stress-resultant components of the macroelement, the equilibrium of the element has to be respected. Therefore, this calibration strategy is proven to be more accurate. Numerical simulations have taken place and a satisfactory fit to experimental curves is provided for $a_x = 500$, $a_y = 250$, $a_\theta = 250$.

In order to illustrate the influence of the above mentioned parameters on the global response of a RC element, a cantilever beam subjected to a transversal load has been numerically simulated for two cases; in the first case a parametric study concernig the r_{x0}, r_{y0}, $r_{\theta 0}$ values is presented in Figure 3.9a. For the second case, three sets of the parameters a_x, a_y, a_θ are selected and the results are presented in Figure 3.9b.

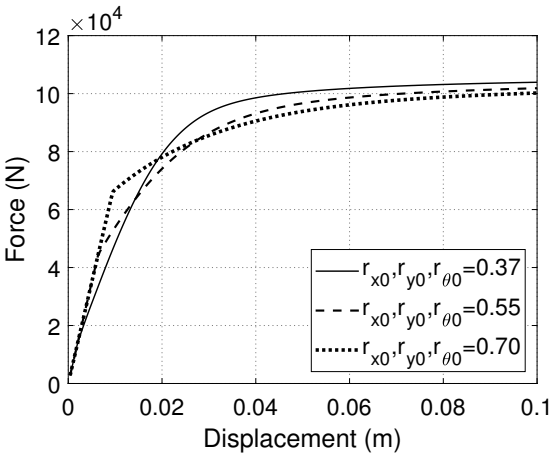

(a) Influence of the parameters r_{x0}, r_{y0}, $r_{\theta 0}$ on the global response of a beam.

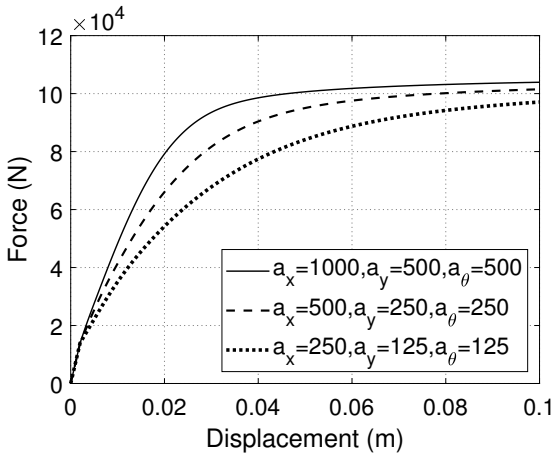

(b) Influence of the parameters a_x, a_y, a_θ on the global response of a beam.

Figure 3.9: Parametric study of the parameters r_{x0}, r_{y0}, $r_{\theta 0}$ and a_x, a_y, a_θ of the proposed macroelement.

3.4 Integration algorithm

A backward (implicit) Euler scheme of the Return Mapping Algorithm is used for the the numerical implementation of macroelement. The generalized forces are calculated for a given history of generalized strains at the section level. During each load increment, a *trial* elastic prediction of the sectional response is considered and a plastic correction is carried out if the predicted stress point is situated out of the loading surface.

The main idea consists in calculating the forces and the internal variables of the current step, denoted $n+1$, based on the previous converged step n and for a given $\underline{\varepsilon}_{s_{n+1}}$. The equations of the developed model are expressed in an incremental form and the *trial* elastic prediction is then expressed as:

$$\begin{aligned}
\underline{F}^{trial}_{s_{n+1}} &= \underline{\underline{K}}^{el}_{s}(\underline{\varepsilon}_{s_{n+1}} - \underline{\varepsilon}^{pl}_{s_n}) \Leftrightarrow \\
\underline{F}^{trial}_{s_{n+1}} &= \underline{\underline{K}}^{el}_{s}(\underline{\varepsilon}_{s_{n+1}} - \underline{\varepsilon}_{s_n} + \underline{\varepsilon}_{s_n} - \underline{\varepsilon}^{pl}_{s_n}) \Leftrightarrow \\
\underline{F}^{trial}_{s_{n+1}} &= \underline{\underline{K}}^{el}_{s} d\underline{\varepsilon}_{s_n} + \underline{F}_{s_n}
\end{aligned} \tag{3.33}$$

The force vector of the current step $n+1$ is defined by the following relation and is re-written as the sum of the *trial* elastic prediction and the correction:

$$\begin{aligned}
\underline{F}_{s_{n+1}} &= \underline{\underline{K}}^{el}_{s}(\underline{\varepsilon}_{s_{n+1}} - \underline{\varepsilon}^{pl}_{s_{n+1}}) \Leftrightarrow \\
\underline{F}_{s_{n+1}} &= \underline{\underline{K}}^{el}_{s}(\underline{\varepsilon}_{s_{n+1}} - \underline{\varepsilon}^{pl}_{s_n} + \underline{\varepsilon}^{pl}_{s_n} - \underline{\varepsilon}^{pl}_{s_{n+1}}) \Leftrightarrow \\
\underline{F}_{s_{n+1}} &= \underline{\underline{K}}^{el}_{s}(\underline{\varepsilon}_{s_{n+1}} - \underline{\varepsilon}^{pl}_{s_n}) \underbrace{- \underline{\underline{K}}^{el}_{s}(\underline{\varepsilon}^{pl}_{s_{n+1}} - \underline{\varepsilon}^{pl}_{s_n})}_{d\underline{F}_s} \Leftrightarrow \\
\underline{F}_{s_{n+1}} &= \underline{F}^{trial}_{s_{n+1}} + d\underline{F}_s
\end{aligned} \tag{3.34}$$

Using Equation (3.22) the incremental form of the plastic strain vector is obtained:

$$\begin{aligned}
\dot{\underline{\varepsilon}}^{pl}_{s} &= \dot{\lambda}\frac{\partial f_L}{\partial \underline{F}_s} \Rightarrow \\
\underline{\varepsilon}^{pl}_{s_{n+1}} - \underline{\varepsilon}^{pl}_{s_n} &= d\lambda\frac{\partial f_L(\underline{F}_{s_n}, \underline{r}_n)}{\partial \underline{F}_s} \Rightarrow \\
\underline{\varepsilon}^{pl}_{s_{n+1}} &= \underline{\varepsilon}^{pl}_{s_n} + d\lambda\frac{\partial f_L(\underline{F}_{s_n}, \underline{r}_n)}{\partial \underline{F}_s}
\end{aligned} \tag{3.35}$$

and thus the correction of the forces is expressed by combining Equations (3.34)-(3.35):

$$\begin{aligned} d\underline{F}_s &= -\underline{\underline{K}}_s^{el}(\underline{\varepsilon}_{s_{n+1}}^{pl} - \underline{\varepsilon}_{s_n}^{pl}) \Leftrightarrow \\ d\underline{F}_s &= -\underline{\underline{K}}_s^{el} d\lambda \frac{\partial f_L(\underline{F}_{s_n}, \underline{r}_n)}{\partial \underline{F}_s} \end{aligned} \tag{3.36}$$

By the use of Equation (3.36), Equation (3.34) takes the following form:

$$\underline{F}_{s_{n+1}} = \underline{F}_{s_{n+1}}^{trial} \underbrace{-\underline{\underline{K}}_s^{el} d\lambda \frac{\partial f_L(\underline{F}_{s_n}, \underline{r}_n)}{\partial \underline{F}_s}}_{d\underline{F}_s} \tag{3.37}$$

The incremental form of the hardening evolution is given by Equation (3.23):

$$\begin{aligned} &\dot{\underline{r}} = \dot{\lambda} \underline{h}_L(\underline{F}_s, \underline{r}) \Rightarrow \\ &\underline{r}_{n+1} - \underline{r}_n = d\lambda \underline{h}_L(\underline{F}_s, \underline{r}) \Rightarrow \\ &\underline{r}_{n+1} = \underline{r}_n + d\lambda \underline{h}_L(\underline{F}_s, \underline{r}) \end{aligned} \tag{3.38}$$

If the current stress state is out of the domain of linear elasticity it must remain at the current loading surface. Consequently, the following condition for the yield function must be satisfied:

$$f_{Ln+1} = 0 \tag{3.39}$$

Considering the non-linearity of the yield surface of the proposed model, which corresponds to a high order polynomial expression, the above equation needs to be solved through an iterative resolution scheme. For that purpose the Newton–Raphson method is adopted based on the linearization of Equation (3.39).

In the following expressions n is the current step and i corresponds to the iteration of the Newton–Raphson algorithm.

During the iterative procedure, Equations (3.35), (3.37), (3.38) describe the updated state between the iterations. In particular, Equation (3.35) is transformed to:

$$\underline{\varepsilon}_{s_n}^{pl,i+1} = \underline{\varepsilon}_{s_n}^{pl,i} + \delta d\lambda^i \frac{\partial f_L(\underline{F}_{s_n}^i, \underline{r}_n^i)}{\partial \underline{F}_s}, \tag{3.40}$$

Equation (3.37) becomes :

$$\underline{F}_{s_n}^{i+1} = \underline{F}_{s_n}^{i} \underbrace{- \underline{\underline{K}}_s^{el} \delta d\lambda^i \frac{\partial f_L(\underline{F}_{s_n}^i, \underline{r}_n^i)}{\partial \underline{F}_s}}_{d\underline{F}_s^i} \tag{3.41}$$

with $\underline{F}_{s_n}^0 = \underline{F}_{s_{n+1}}^{trial}$ initially and Equation (3.38) results in:

$$\underline{r}_n^{i+1} = \underline{r}_n^i + \delta d\lambda^i \underline{h}_L(\underline{F}_{s_n}^i, \underline{r}_n^i) \tag{3.42}$$

Equation (3.39) is linearized by the Newton–Raphson method and has the following expression:

$$f_L(\underline{F}_{s_n}^{i+1}, \underline{r}_n^{i+1}) = f_L(\underline{F}_{s_n}^i, \underline{r}_n^i) + \frac{\partial f_L(\underline{F}_{s_n}^i, \underline{r}_n^i)}{\partial \underline{F}_s} d\underline{F}_s^i + \frac{\partial f_L(\underline{F}_{s_n}^i, \underline{r}_n^i)}{\partial \underline{r}} d\underline{r}^i = 0 \tag{3.43}$$

Substituting Equations (3.41) and (3.42) in Equation (3.43) allows to obtain the expression of the yield function as a function of a single unknown scalar variable, i.e. $\delta d\lambda^i$

$$\begin{aligned} f_L(\underline{F}_{s_n}^{i+1}, \underline{r}_n^{i+1}) = f_L(\underline{F}_{s_n}^i, \underline{r}_n^i) &- \frac{\partial f_L(\underline{F}_{s_n}^i, \underline{r}_n^i)}{\partial \underline{F}_s} \underline{\underline{K}}_s^{el} \delta d\lambda^i \frac{\partial f_L(\underline{F}_{s_n}^i, \underline{r}_n^i)}{\partial \underline{F}_s} \\ &+ \frac{\partial f_L(\underline{F}_{s_n}^i, \underline{r}_n^i)}{\partial \underline{r}} \delta d\lambda^i \underline{h}_L(\underline{F}_{s_n}^i, \underline{r}_n^i) = 0 \end{aligned} \tag{3.44}$$

and thus $\delta d\lambda^i$ is obtained by the resolution of the above expression with respect to $\delta d\lambda^i$:

$$\delta d\lambda^i = \frac{f_L(\underline{F}_{s_n}^i, \underline{r}_n^i)}{\frac{\partial f_L(\underline{F}_{s_n}^i, \underline{r}_n^i)}{\partial \underline{F}_s} \underline{\underline{K}}_s^{el} \frac{\partial f_L(\underline{F}_{s_n}^i, \underline{r}_n^i)}{\partial \underline{F}_s} - \frac{\partial f_L(\underline{F}_{s_n}^i, \underline{r}_n^i)}{\partial \underline{r}} \underline{h}_L(\underline{F}_{s_n}^i, \underline{r}_n^i)} \tag{3.45}$$

3.5 Adjustment for cyclic loading conditions

The proposed model is built within the elasto-plasticity framework and therefore, the unloading response is elastic. This does not provide a realistic response as the model cannot capture different phenomena appearing during cyclic loads, such as stiffness degradation and pinching, already described in Chapter 1. Two simplified strategies are proposed hereafter to improve the performance of the model: the former for loading cycles of constant sign and the latter for loading cycles of alternate sign; the driving idea is that the response of the reinforced concrete element is mainly controlled by steel once concrete is damaged and beyond a certain level of damage of the concrete.

- **Cyclic loads of constant sign**

  As the values of the $\underline{r}$ (Equation (3.20)) tend to unity, the loading surface approaches the failure surface and thus the damage of concrete is more severe. A limit value is assigned to each hardening variable $r_x^{lim}, r_y^{lim}, r_\theta^{lim}$, such as one or more of the following conditions are satisfied:

  $$r_x \geq r_x^{lim} \quad , \quad r_y \geq r_y^{lim} \quad , \quad r_\theta \geq r_\theta^{lim} \tag{3.46}$$

  then, accordingly, the axial, shear, and flexural components of the sectional stiffness matrix get the stiffness of steel:

  $$K_x = K_x^{steel} \quad , \quad K_y = K_y^{steel} \quad , \quad K_\theta = K_\theta^{steel} \tag{3.47}$$

  The limit value for each hardening variable is fixed at 0.8. The global response of a cantilever beam subjected to a cyclic transversal load of constant sign is presented in Figure 3.10 for two cases; using the elastic stiffness and the modified (steel) stiffness.

- **Cyclic loads of alternate sign**

  For the case of cyclic loads of alternate sign, two approaches for considering stiffness degradation are proposed:

  – The first approach for considering stiffness degradation is based on the well-known constitutive model developed by Menegotto and Pinto (Menegotto and Pinto 1973). This model provides a relation which describes the evolution of

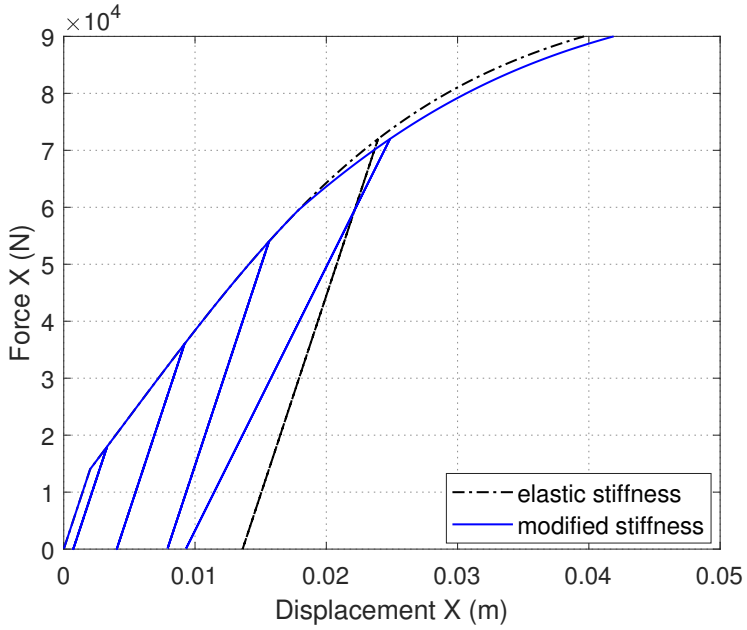

Figure 3.10: Comparison of the global responses of a cantilever beam subjected to a cyclic transversal load, using the elastic stiffness and the modified (steel) stiffness.

the elastic modulus at the semi-cycle under tension (Equation (3.48)).

$$E = E_0(c_1 + (1 - c_1)e^{-c_2 p^2}) \tag{3.48}$$

where E_0 is the initial Young modulus, p corresponds to the plastic strain and c_1 and c_2 two material constants, the former depending on the geometric properties of the rebars and the latter depending on the mechanical properties of the steel. The values assigned to these constants can be found in the technical report of Fléjou 2018. The relation (3.48) is used in the proposed macroelement for each component independently as:

$$\underline{\underline{K}}_s^{el}(i,i) = \underline{\underline{K}}_{s0}^{el}(i,i)(c_1(i) + (1 - c_1(i))e^{-c_2(i)p^2(i)}) \tag{3.49}$$

In the above relation $\underline{\underline{K}}_{s0}^{el}$ is the initial stiffness matrix of the section and i indicates its different components. In Figure 3.11, the global response of a cantilever beam subjected to a cyclic transversal displacement of alternate sign is presented for two cases: using the elastic stiffness and the modified stiffness following Equation (3.49).

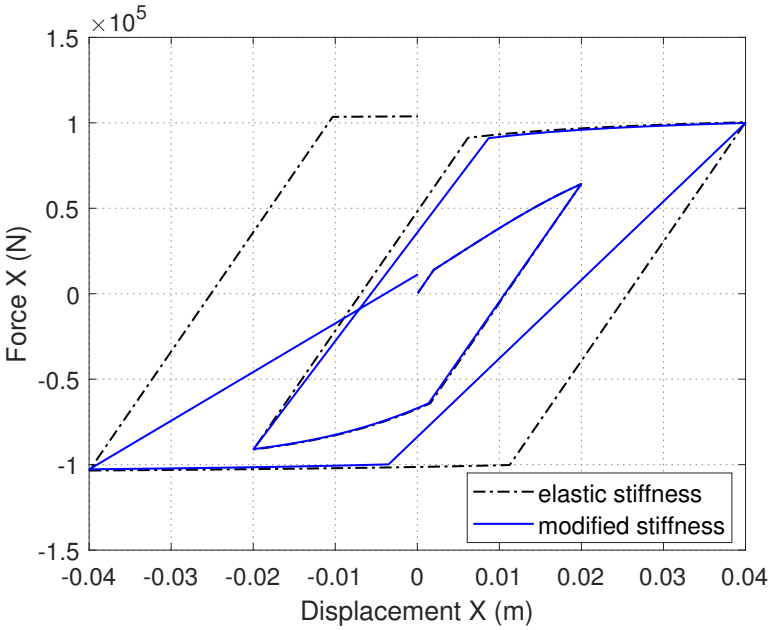

Figure 3.11: Comparison of the global responses of a cantilever beam subjected to cyclic transversal displacement, using the elastic stiffness and modified stiffness according to Equation 3.49.

– The second approach considers stiffness degradation, the pinching effect and stiffness recovery in a simplified way as it is schematically depicted in Figure 3.12. Firstly, the same conditions (3.46) are considered. If one or more of these

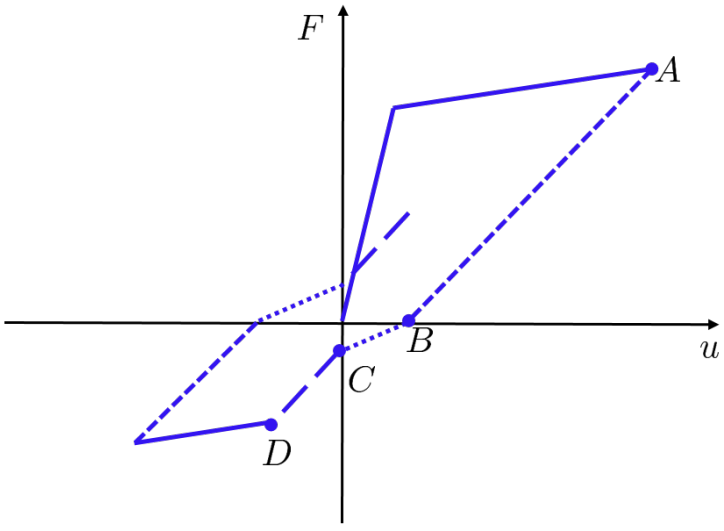

Figure 3.12: Schematic representation of cyclic response by considering a simplified approach for stiffness degradation, the pinching effect and stiffness recovery.

conditions are verified, then:

- during unloading, until force becomes zero (point A until point B in Figure 3.12) a reduced stiffness of 50% of the initial stiffness is considered.
- during crack-reclosure (point B until point C in Figure 3.12), a further reduced stiffness of 20% of the initial stiffness is considered.
- during stiffness recovery (point C until point D in Figure 3.12), it is assumed a subsequent increase of the stiffness, the value of which is 50% of the initial stiffness.

In Figure 3.13, the global response of a cantilever beam subjected to a cyclic rotation of alternate sign is presented for two cases: using the elastic stiffness and the modified stiffnesses following the above mentioned modifications.

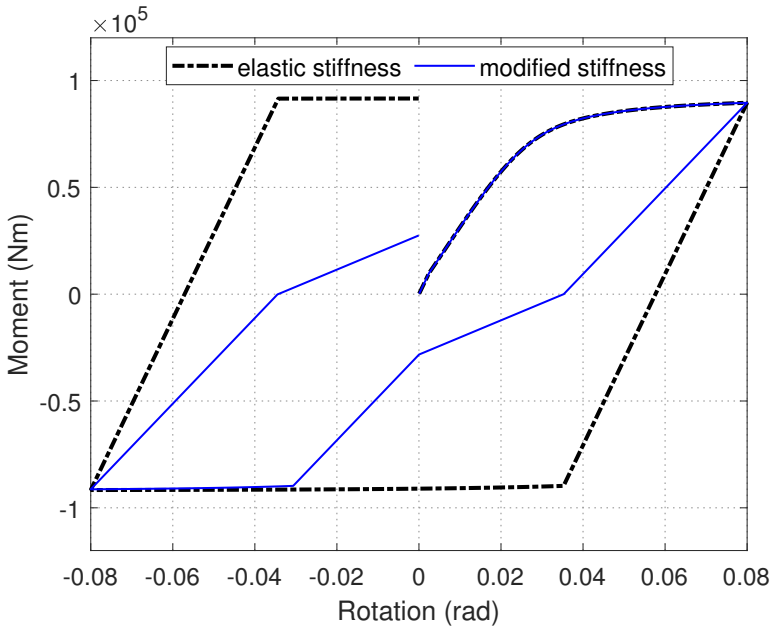

Figure 3.13: Comparison of the global responses of a cantilever beam subjected to a cyclic rotation, using the elastic stiffness and the modified stiffnesses.

3.6 Convergence rate

It has been numerically observed that the use of the updated stiffness matrix given by Equation (3.27) often lead to numerical instabilities and convergence failure (when off-diagonal terms appeared). This could be related to the reduced integration technique of the stiffness matrix of the FLI Timoshenko beam element. On the other hand, the use of the elastic stiffness matrix significantly increased the computational time.

In order to improve the numerical performance of the proposed macroelement, a numerical tangent stiffness matrix is adopted. More specifically, the approach proposed in the finite element code LAGAMINE (University of Liège) by Barnichon (Barnichon 1998) and Collin (Collin 2003) which consists in calculating the elementary stiffness matrix at each time step as the derivative of nodal forces with respect to displacements. For this, the compliance matrix is computed by applying arbitrarily small perturbations of the velocity gradient as initially proposed by Charlier (Charlier 1987). The terms of the compliance matrix are numerically calculated by finite differences between a perturbed state and a non-perturbed state. Thus, for each term of the matrix, successive small perturbations of the velocity are applied at the level of the constitutive law and each component of the matrix is the ratio of the stress variations at the end of the step and the variations of the velocity gradient.

The proposed solution is inspired by these works. In fact, the adopted strategy relies on updating the sectional stiffness matrix by applying strain perturbations at the constitutive law level once convergence is achieved. At this state the force vector is denoted $\underline{F}_s^{conv}$. Subsequently, strain perturbations are applied successively for each loading direction and during each perturbation a new state is calculated by applying the same resolution algorithm, described in section 3.4. Thus, for each directional perturbation i of the generalized strain vector $d\underline{\varepsilon}_s^{per}$ a new state of generalized forces is computed at each perturbed state and is denoted $\underline{F}_s^{per}$. The magnitude of each directional strain perturbation is fixed at $1.0\,\mathrm{e}^{-8}$. The sectional stiffness matrix is updated at every loading step and each term is numerically calculated by the following equation:

$$\underline{\underline{K}}_s^{per}(i,i) = \frac{\underline{F}_s^{per}(i) - \underline{F}_s^{conv}(i)}{d\underline{\varepsilon}_s^{per}(i)} \tag{3.50}$$

Calculation speed is significantly improved as the convergence rate is accelerated and the number of necessary iterations is reduced. Numerical simulations of a cantilever beam subjected to transversal monotonic displacement at its free edge have been conducted to

illustrate the influence of the adopted strategy on the convergence rate. One finite element has been used for the spatial discretization and the load has been divided into 1000 steps. Figure 3.14 presents the number of the necessary iterations versus the time step of the analysis for two cases: using the elastic stiffness and the numerical stiffness applying strain perturbations.

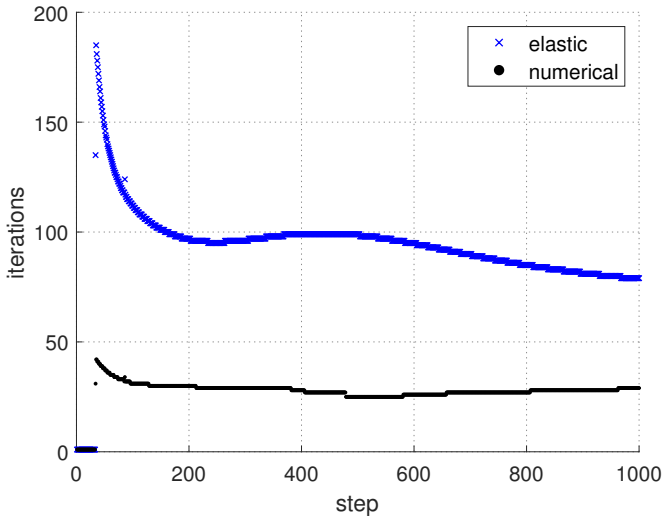

Figure 3.14: Number of necessary iterations for the convergence of the global Newton algorithm using the elstic stiffness and the updated stiffness with strain perturbations.

3.7 Summary of macroelement parameters

Eighteen (18) parameters need to be defined for the constitutive description of the sectional behavior of RC beams-columns given by the proposed macroelement. For each parameter, an identification procedure has been proposed in Section 3.3. The only set of parameters that may require a more specific calibration are those related to the rate of hardening (a_x, a_y, a_θ). However, default values for these parameters have been provided in Section 3.3, if calibration procedure is not feasible. A description of the macroelement parameters and the corresponding required identification procedure is briefly presented in Table 3.1.

Table 3.1: Macroelement parameters

Description	**Parameter**	**Identification**
Linear elastic behavior		
Axial stiffness	K_x	Geometrical &
Shear stiffness	K_y	mechanical
Flexural stiffness	K_θ	properties
Axial elastic limit	r_{x0}	Selected in the
Shear elastic limit	r_{y0}	range 0.35 to 0.8
Flexural elastic limit	$r_{\theta 0}$	(see Table 2.15)
Standardization		
Maximum axial tensile force	$F^t_{x,max}$	From material
Maximum axial compressive force	$F^c_{x,max}$	strength formulas
Shear shift parameter	F^*_y	MCFT (Rahal 2000b)
Flexural shift parameter	M^*_θ	Moment-axial force interaction diagram (CEN 2004)
Hardening evolution laws		
Axial rate of hardening	a_x	Calibration by
Shear rate of hardening	a_y	numerical simulations
Flexural rate of hardening	a_θ	or experiments
Stiffness degradation (cyclic loading of constant sign)		
Axial stiffness of steel	K^{steel}_x	Geometrical &
Shear stiffness of steel	K^{steel}_y	mechanical
Flexural stiffness of steel	K^{steel}_θ	properties
Stiffness degradation (cyclic loading of alternate sign)		
Geometrical property of the rebars	c_1	Found in the technical
Mechanical property of the steel	c_2	report of Fléjou 2018

Chapter 4

Modeling up to failure

4.1 Introduction

In order to simulate the behavior up to failure of steel structures, kinematically enhanced formulations coupled with cohesive models were first introduced by Armero and Ehrlich (Armero and Ehrlich 2004, 2006; Ehrlich and Armero 2005) for generalized Euler-Bernoulli and Timoshenko beams. Based on their work, several researchers focused on the failure of RC structures.

In particular, Pham et al. (Pham et al. 2013; Pham et al. 2010) used the FLI Timoshenko beam presented in Section 3.2.1, uncoupled stress-resultant constitutive models for the continuous part and a linear generalized cohesive model describing the relation between moment-rotation jump to represent the flexural behavior until failure. The parameter identification of the generalized flexural cohesive law was carried out via kinematically enhanced multi-fiber Timoshenko finite element beams, enriched by axial displacement discontinuity at the fiber level. The longitudinal dimension of the beams was relatively small with respect to the transversal dimensions in order to represent a sectional analysis. In their formulation, different constitutive laws (continuum and cohesive, the latter given in terms of stress-axial displacement jump) at a local level were assigned to each fiber to respresent the uniaxial concrete and steel behavior.

Jukić et al. 2013 proposed a stress-resultant Euler-Bernoulli beam with linear shape functions for the axial component and high order (of order 3) shape functions for the transversal and rotational components for the continuous part of the finite element formulation. The enhanced formulation integrated the discontinuity at the rotational component. The constitutive description at the discontinuity was given by a linear cohesive model in terms of moment-rotation jump. Jukić developed a muti-fiber Euler-Bernoulli beam (Jukiić 2013) and Jukić et al. presented a muti-fiber Timoshenko beam (Jukić et al. 2014) for the analysis of RC beams and frames until failure. In both works, the axial kinematical field of the fibers was enriched by discontinuities. The continuous constitutive

description of the concrete layer was given by a damage model while for the discontinuity a softening-damage traction-separation cohesive model was adopted. An elasto-plastic model and a softening-plasticity traction-separation cohesive law were used to describe the continuous and the discontinuous part of the steel.

Bui et al. 2014 investigated the response of RC beam-columns by considering two modes of failure: flexural and shear. A generalized Timoshenko FLI beam element enriched by two discontinuity variables (transversal displacement and rotation jumps) was used. The results of the numerical simulations of a four-point bending test were presented by considering only shear failure, only bending failure and both shear and bending failures (see Figure 4.1). The authors showed that when considering only shear failure, with the bending response remaining elastic, the overall resistance was highly overestimated and the repsonse was brittle. When considering only bending failure mode or both shear and bending failures, the obtained results were quite similar, more realistic and the response was more ductile. The authors explained that the type of failure depended on the peak resistances of the generalized shear and bending models. The dominant failure mechanism is therefore mainly driven by the geometrical and mechanical properties of the RC element. This conclusion is the basis of the assumptions of the enhanced formulation presented in section 4.2.

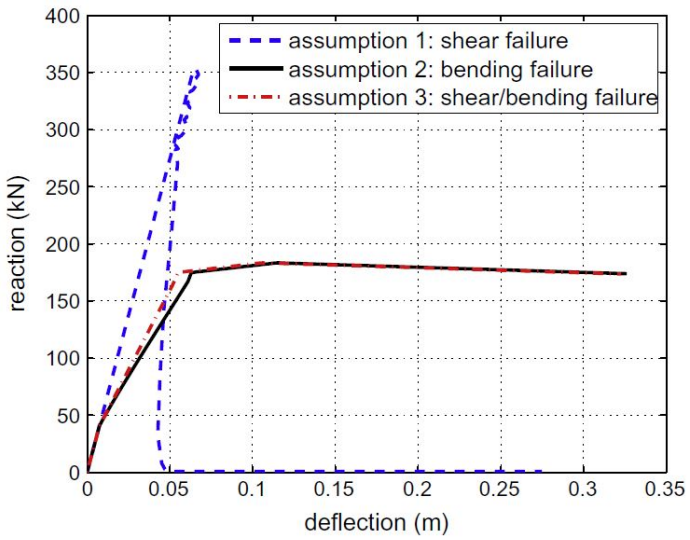

Figure 4.1: Load-deflection curves for four-point bending test; assumption 1: only shear failure, assumption 2: only bending failure, assumption 3: both shear and bending failures are considered (Bui et al. 2014).

Bitar and co-authors used a high-order Timoshenko beam finite element as the basis of the enhanced formulation. This beam was initially developed by Caillerie et al. 2015 and presents the advantage that it is free of shear locking and that only one element provides the exact displacements at the nodes for whatever loading for the case of linear elasticity. In the first part of their work (Bitar et al. 2018b), a generalized beam was considered and uncoupled stress-resultant models for the continuous part, while a rotational jump was introduced to account for bending failure. In Bitar et al. 2019, the authors presented an enhanced formulation of a multi-fiber beam. The fibers were enriched at the Gauss points by axial discontinuities whose behavior was described by a linear cohesive law linking the axial stress and the displacement jump. The continuous part of the uniaxial behavior was expressed by a damage law for the concrete fibers and an elasto-plastic law for the steel fibers, while the shear behavior was assumed elastic. The authors compared finally the results of their enhanced high-order Timoshenko beam with the results of the enhanced FLI Timoshenko beam.

4.2 Enhanced formulation

In the following, the variables assigned to continuous fields have a single top dash while those assigned to discontinuous fields have a double top dash.

The adopted enhanced formulation is the one proposed by Ehrlich and Armero 2005. In particular, among the four formulations introduced by the authors, the $N0M0S0$ formulation corresponds to a constant axial, constant bending and constant shear finite element with one-point integration rule. In our case the plastic hinges are considered activated at the center of the Timoshenko FLI beam element. The enhanced generalized displacement field of the beam section, in the general case (i.e. three discontinuity jumps assigned to each displacement component), is given by:

$$\underline{U}_s(x,t) = \overline{\underline{U}}_s(x,t) + \overline{\overline{\underline{U}}}_s(x,t) = \underline{\underline{N}}(x)\underline{U}_e(t) + \underline{\underline{M}}(x)\overline{\overline{\underline{U}}}_e(t) \tag{4.1}$$

with:

$$\underbrace{\underline{U}_s = \begin{bmatrix} U_x \\ U_y \\ \Theta_z \end{bmatrix}}_{\text{total displacements}} \quad , \quad \underbrace{\overline{\underline{U}}_s = \begin{bmatrix} \overline{U}_x \\ \overline{U}_y \\ \overline{\Theta}_z \end{bmatrix}}_{\text{continuous part}} \quad , \quad \underbrace{\overline{\overline{\underline{U}}}_s = \begin{bmatrix} \overline{\overline{U}}_x \\ \overline{\overline{U}}_y \\ \overline{\overline{\Theta}}_z \end{bmatrix}}_{\text{discontinuous part}} , \tag{4.2}$$

$$\underbrace{\underline{U}_e = \begin{bmatrix} U_{xi} \\ U_{yi} \\ \Theta_{zi} \\ U_{xj} \\ U_{yj} \\ \Theta_{zj} \end{bmatrix}}_{\text{nodal displacements}} \quad , \quad \underbrace{\overline{\overline{\underline{U}}}_e = \begin{bmatrix} \overline{\overline{U}}_x \\ \overline{\overline{U}}_y \\ \overline{\overline{\Theta}}_z \end{bmatrix}}_{\text{elementary displacement jumps}} , \tag{4.3}$$

$\underline{\underline{N}}$ the matrix of the FLI Timoshenko beam shape functions (see Equations (3.4), (3.5), (3.6)) and $\underline{\underline{M}}$ the matrix containing the enhancement interpolation functions.

The additional term $\overline{\overline{\underline{U}}}_s(x,t)$ in Equation (4.1) describe the discontinuities in the generalized displacement field. Given the singularities of the corresponding strain field and the purpose being to preserve the structure of the large-scale problem in terms of the large-scale displacements, $\underline{\underline{M}}$ is decomposed into the following terms:

$$\underline{\underline{M}} = \begin{bmatrix} M_1^a & M_2^a & M_3^a \\ M_1^t & M_2^t & M_3^t \\ M_1^\theta & M_2^\theta & M_3^\theta \end{bmatrix} = \underbrace{\begin{bmatrix} \overline{M}_1^a & \overline{M}_2^a & \overline{M}_3^a \\ \overline{M}_1^t & \overline{M}_2^t & \overline{M}_3^t \\ \overline{M}_1^\theta & \overline{M}_2^\theta & \overline{M}_3^\theta \end{bmatrix}}_{\overline{\underline{\underline{M}}}(x)} + \underbrace{\begin{bmatrix} H_{x_d}^a & 0 & 0 \\ 0 & H_{x_d}^t & 0 \\ 0 & 0 & H_{x_d}^\theta \end{bmatrix}}_{\overline{\overline{\underline{\underline{M}}}}(x)} \tag{4.4}$$

with $H_{x_d}^a$, $H_{x_d}^t$, $H_{x_d}^\theta$ the Heaviside functions and $\overline{\underline{\underline{M}}}(x)$ containing additional functions that their role is to ensure the continuity of the displacement field between the finite elements.

Equation (4.1) is re-expressed for every displacement component as:

$$\begin{aligned} U_x(x,t) &= \overline{U}_x(x,t) + \overline{\overline{U}}_x(x,t) = \underline{N}^a(x)\underline{U}_e(t) + \underline{M}^a(x)\overline{\overline{\underline{U}}}_e(t) \\ U_y(x,t) &= \overline{U}_y(x,t) + \overline{\overline{U}}_y(x,t) = \underline{N}^t(x)\underline{U}_e(t) + \underline{M}^t(x)\overline{\overline{\underline{U}}}_e(t) \\ \Theta_z(x,t) &= \overline{\Theta}_z(x,t) + \overline{\overline{\Theta}}_z(x,t) = \underline{N}^\theta(x)\underline{U}_e(t) + \underline{M}^\theta(x)\overline{\overline{\underline{U}}}_e(t) \end{aligned} \tag{4.5}$$

with $\underline{N}^a$, $\underline{N}^t$ and $\underline{N}^\theta$ the shape functions and $\underline{M}^a$, $\underline{M}^t$ and $\underline{M}^\theta$ the enhancement functions for each component. The enhancement functions are not known a priori and in the follow-

ing, the procedure of their identification is provided, based on the kinematic assumptions describing the discontinuity when it is completely open.

The generalized strain field $\underline{\varepsilon}_s(x,t)$ of a Timoshenko beam's section is given as (see also Equation (3.7)):

$$\underline{\varepsilon}_s(x,t) = \begin{bmatrix} \varepsilon_x(x,t) \\ \beta_y(x,t) \\ \kappa_\theta(x,t) \end{bmatrix} = \begin{bmatrix} \frac{\partial}{\partial x} U_x(x,t) \\ \frac{\partial}{\partial x} U_y(x,t) - \Theta_z(x,t) \\ \frac{\partial}{\partial x} \Theta_z(x,t) \end{bmatrix} \tag{4.6}$$

where $\varepsilon_x(x,t)$, $\beta_y(x,t)$ and $\kappa_\theta(x,t)$ are the axial strain, the shear strain and the curvature respectively. It is obtained by derivation of the displacement field of Equation (4.1):

$$\underline{\varepsilon}_s(x,t) = \overline{\underline{\varepsilon}}_s(x,t) + \overline{\overline{\underline{\varepsilon}}}_s(x,t) = \underline{\underline{B}}(x)\underline{U}_e(t) + \underline{\underline{G}}_r(x)\overline{\overline{\underline{U}}}_e(t) \tag{4.7}$$

where $\underline{\underline{B}}$ is the matrix of the derivatives of the FLI Timoshenko beam shape functions (see Equations (3.7), (3.8) again neglecting the linear terms) and $\underline{\underline{G}}_r$ the matrix containing the derivatives of the enhancement interpolation functions of the following form:

$$\underline{\underline{G}}_r = \begin{bmatrix} G^\varepsilon_{r1} & G^\varepsilon_{r2} & G^\varepsilon_{r3} \\ G^\gamma_{r1} & G^\gamma_{r2} & G^\gamma_{r3} \\ G^\kappa_{r1} & G^\kappa_{r2} & G^\kappa_{r3} \end{bmatrix} = \underbrace{\begin{bmatrix} \overline{G}^\varepsilon_{r1} & \overline{G}^\varepsilon_{r2} & \overline{G}^\varepsilon_{r3} \\ \overline{G}^\gamma_{r1} & \overline{G}^\gamma_{r2} & \overline{G}^\gamma_{r3} \\ \overline{G}^\kappa_{r1} & \overline{G}^\kappa_{r2} & \overline{G}^\kappa_{r3} \end{bmatrix}}_{\overline{\underline{\underline{G}}}_r(x)} + \underbrace{\begin{bmatrix} \delta^a_{x_d} & 0 & 0 \\ 0 & \delta^t_{x_d} & 0 \\ 0 & 0 & \delta^\theta_{x_d} \end{bmatrix}}_{\overline{\overline{\underline{\underline{G}}}}_r(x)} \tag{4.8}$$

with $\delta^a_{x_d}$, $\delta^t_{x_d}$, $\delta^\theta_{x_d}$ the Dirac functions and $\overline{\overline{\underline{\underline{G}}}}_r$ the diagonal matrix of the Dirac functions. Equation (4.7) is equivalent to the following expressions for each strain component:

$$\begin{aligned} \varepsilon_x(x,t) &= \overline{\varepsilon}_x(x,t) + \overline{\overline{\varepsilon}}_x(x,t) = \underline{B}^\varepsilon(x)\underline{U}_e(t) + \underline{G}^\varepsilon_r(x)\overline{\overline{\underline{U}}}_e(t) \\ \beta_y(x,t) &= \overline{\beta}_y(x,t) + \overline{\overline{\beta}}_y(x,t) = \underline{B}^\gamma(x)\underline{U}_e(t) + \underline{G}^\gamma_r(x)\overline{\overline{\underline{U}}}_e(t) \\ \kappa_\theta(x,t) &= \overline{\kappa}_\theta(x,t) + \overline{\overline{\kappa}}_\theta(x,t) = \underline{B}^\kappa(x)\underline{U}_e(t) + \underline{G}^\kappa_r(x)\overline{\overline{\underline{U}}}_e(t) \end{aligned} \tag{4.9}$$

with $\underline{B}^\varepsilon(x)$, $\underline{B}^\gamma(x)$, $\underline{B}^\kappa(x)$ the derivatives of the shape functions for the three strain components and $\underline{G}^\varepsilon_r(x)$, $\underline{G}^\gamma_r(x)$ and $\underline{G}^\kappa_r(x)$ the derivatives of the enhancement functions, with respect to x, for the three enhanced strain components. Using the decomposition of $\underline{\underline{G}}_r$ into continuous and discontinuous parts (see Equation (4.8)), the strain field correspond-

ing to Equation (4.7) is rewritten as:

$$\underline{\varepsilon}_s(x,t) = \underbrace{\underline{\underline{B}}(x)\underline{U}_e(t) + \underline{\underline{\overline{G}}}_r(x)\underline{\overline{\overline{U}}}_e(t)}_{\text{regular part } \underline{\tilde{\varepsilon}}_s(x,t)} + \underbrace{\underline{\underline{\overline{G}}}_r(x)\underline{\overline{\overline{U}}}_e(t)}_{\text{singular part}} \tag{4.10}$$

The matrix $\underline{\underline{\overline{G}}}_r$ is defined by considering the kinematics of the discontinuity at the final state. According to Ehrlich and Armero 2005 at the zero hinge mode (fully softened plastic hinge), the end nodal displacements of the Timoshenko beam finite element (of length L_e) associated to zero strain can be written as (see Figure 4.2):

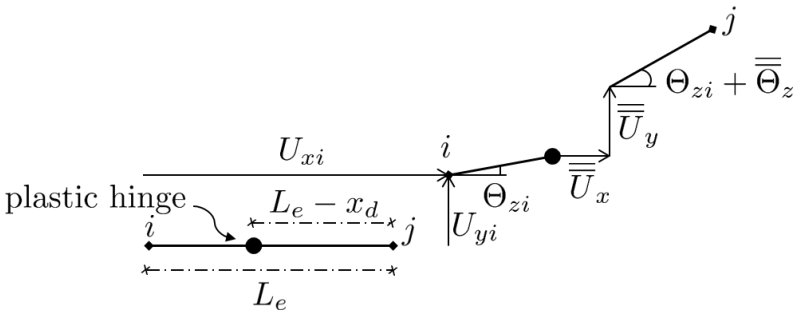

Figure 4.2: Sketch of the plastic hinge mode: initiation of the plastic hinge (bottom) and fully softened hinge (up).

$$\begin{aligned} U_{xj} =& U_{xi} + \overline{\overline{U}}_x \\ U_{yj} =& U_{yi} + \Theta_{zi}L_e + \overline{\overline{U}}_y + (L_e - x_d)\overline{\overline{\Theta}}_z \\ \Theta_{zj} =& \Theta_{zi} + \overline{\overline{\Theta}}_z \end{aligned} \tag{4.11}$$

with x_d the the geometrical position of the discontinuity within the finite element. Based on the above Expressions (4.11) the jump components are defined as:

$$\begin{aligned} \overline{\overline{U}}_x =& U_{xj} - U_{xi} \\ \overline{\overline{U}}_y =& U_{yj} - U_{yi} - x_d\Theta_{zi} - (L_e - x_d)\Theta_{zj} \\ \overline{\overline{\Theta}}_z =& \Theta_{zj} - \Theta_{zi} \end{aligned} \tag{4.12}$$

At the final state, the complete opening of the discontinuities results in rigid body modes and the regular part of the enhanced strains (see Equation (4.10)) in the elements where

the strong discontinuity has been detected vanishes:

$$\tilde{\underline{\varepsilon}}_s(x,t) = \underline{\underline{B}}(x)\underline{U}_e(t) + \underline{\underline{\overline{G}}}_r(x)\underline{\overline{U}}_e(t) = 0 \tag{4.13}$$

and thus for each generalized strain component the following relations hold:

$$\begin{aligned}
\tilde{\varepsilon}_x(x,t) &= \underline{B}^{\varepsilon}(x)\underline{U}_e(t) + \underline{\overline{G}}_r^{\varepsilon}(x)\underline{\overline{U}}_e(t) = 0 \\
\tilde{\beta}_y(x,t) &= \underline{B}^{\gamma}(x)\underline{U}_e(t) + \underline{\overline{G}}_r^{\gamma}(x)\underline{\overline{U}}_e(t) = 0 \\
\tilde{\kappa}_\theta(x,t) &= \underline{B}^{\kappa}(x)\underline{U}_e(t) + \underline{\overline{G}}_r^{\kappa}(x)\underline{\overline{U}}_e(t) = 0
\end{aligned} \tag{4.14}$$

For the FLI Timoshenko beam, $\underline{B}^{\varepsilon}$, $\underline{B}^{\gamma}$ and $\underline{B}^{\kappa}$ are defined in Equation (3.8). Consequently, at the final state, the regular strain components are expressed as:

$$\begin{aligned}
\tilde{\varepsilon} =& \frac{1}{L_e}(U_{xj} - U_{xi}) + \underline{\overline{G}}_r^{\varepsilon}(x)\underline{\overline{U}}_e(t) = 0 \\
\tilde{\gamma} =& \frac{1}{L_e}(U_{yj} - U_{yi}) - \frac{1}{2}(\Theta_{zi} + \Theta_{zj}) + \underline{\overline{G}}_r^{\gamma}(x)\underline{\overline{U}}_e(t) = 0 \\
\tilde{\kappa} =& \frac{1}{L_e}(\Theta_{zj} - \Theta_{zi}) + \underline{\overline{G}}_r^{\kappa}(x)\underline{\overline{U}}_e(t) = 0
\end{aligned} \tag{4.15}$$

By introducing the displacement jumps definitions of Equations (4.12) in Equations (4.15), the expressions $\underline{\overline{G}}_r^{\varepsilon}$, $\underline{\overline{G}}_r^{\gamma}$ and $\underline{\overline{G}}_r^{\kappa}$ are deduced:

$$\underline{\underline{\overline{G}}}_r(x) = \begin{bmatrix} \overline{G}_{r1}^{\varepsilon} & \overline{G}_{r2}^{\varepsilon} & \overline{G}_{r3}^{\varepsilon} \\ \overline{G}_{r1}^{\gamma} & \overline{G}_{r2}^{\gamma} & \overline{G}_{r3}^{\gamma} \\ \overline{G}_{r1}^{\kappa} & \overline{G}_{r2}^{\kappa} & \overline{G}_{r3}^{\kappa} \end{bmatrix} = \begin{bmatrix} -\frac{1}{L_e} & 0 & 0 \\ 0 & -\frac{1}{L_e} & 0 \\ 0 & 0 & -\frac{1}{L_e} \end{bmatrix} \tag{4.16}$$

and thus the enhancement interpolation functions of the matrix $\underline{\underline{\overline{M}}}$ are obtained by integration of the components of the $\underline{\underline{\overline{G}}}_r$ matrix.

The above formulation corresponds to the general case of enhanced kinematics by three discontinuities at each displacement component (axial displacement, transversal displacement and rotation). The purpose of this work being the simplified evaluation of the response of RC beams and columns up to failure, the axial failure mode is excluded as it is the least probable to happen. Furthermore, as stated in Section 4.1, the dominant failure mechanism depends on the geometrical and mechanical properties of the RC element under study (Bui et al. 2014). Considering that the design of RC members is carried out by preventing shear failure (provided that adequate number and spacing of stirrups is

selected), it is assumed in the following that the dominant failure mode is related to flexion. The displacement field is therefore hereafter enhanced only by strong discontinuity at the rotational component. For the other components of the displacement field, the standard interpolation functions of the FLI Timoshenko beam are used.

4.3 Global cohesive model

4.3.1 Activation and behavior

The constitutive behavior of the discontinuity in the rotational field is described by means of a global cohesive model. This model reproduces a softening behavior that associates the moment at the plastic hinge to the rotation jump and it is activated when the moment of the section reaches an ultimate value. In other words, at activation the moment of the cohesive model is identical to the ultimate moment of the macroelement (see Section 3.2.2) while the rotational jump is null. Further increase of the applied flexural loading results in decrease of the cohesive moment and in increase of the rotational jump. For symmetric RC sections, the cohesive model is supposed identical for positive and negative flexion.

The activation criterion of the cohesive model cannot be based on a single ultimate value of the bending moment. Actually, the activation of the 3D failure criterion depends on the interaction forces combination (axial force, shear force, bending moment). Different combinations of the sectional internal forces result in different values of ultimate axial force, shear force and bending moment. In other words, for each loading scenario the ultimate moment is different. The adopted activation criterion is based on the ultimate rotational capacity of the RC element and is given as:

$$\Theta_z \geq \Theta_z^{act} \tag{4.17}$$

and in terms of curvature:

$$\kappa_\theta \geq \kappa_\theta^{act} \tag{4.18}$$

For a cyclic loading, a plasticity type or a damage mechanics type model can be considered, see Figure 4.3 for cyclic loading of constant sign and Figure 4.4 for cyclic loading of alternate sign.

For the case of a plastic softening law, when the ultimate flexural capacity of the section

is reached and the cohesive model is activated, as mentioned before, increasing the imposed rotation results to further opening of the discontinuity and reduction of the cohesive moment (plastic softening). If unloading pursues, the opening of the discontinuity remains intact, likewise the remaining plastic deformations in the framework of a plasticity law, while the moment decreases. If reloading conditions are applied, the moment increases until the previous value (absolute) is reached and thereafter the rotational jump evolves according to the sign of the cohesive moment.

If damage softening law is considered, when the discontinuity is activated, further rotation increment results in decrease of the cohesive moment and increase of the magnitude of the rotational jump. If unloading follows, the opening of the discontinuity decreases accompanied by decrease of the moment (elastic unloading). At this state, if reloading occurs, the rotational jump and the moment increase until their previous values (absolute) and the opening of the discontinuity increases, while the cohesive moment decreases until it vanishes.

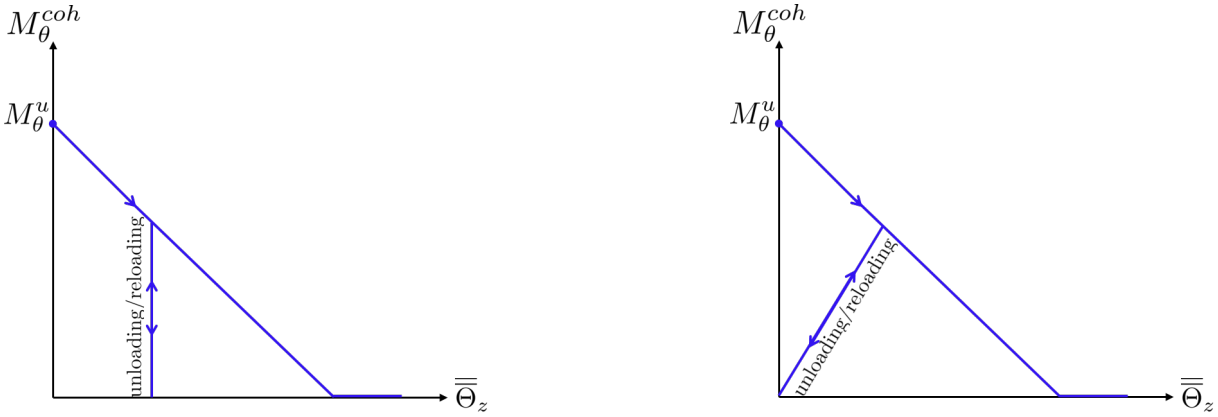

(a) Plastic type softening model

(b) Damage type softening model

Figure 4.3: Cyclic loading of constant sign: plastic hinge moment – rotational jump relations.

A damage softening law can represent more realistically the crack closure and the pinching effect, while a plastic softening law is more appropriate for modeling permanent inelastic deformations. The role of the activation criterion is also crucial for the choice of the softening law during cyclic loading. If the criterion is activated at early stages of the loading, a plastic softening model is more appropriate to represent inelastic deformations. Otherwise, at late stages of loading the pinching effect is more pronounced and a damage softening model can be more suitable to represent this phenomenon. In the following, a

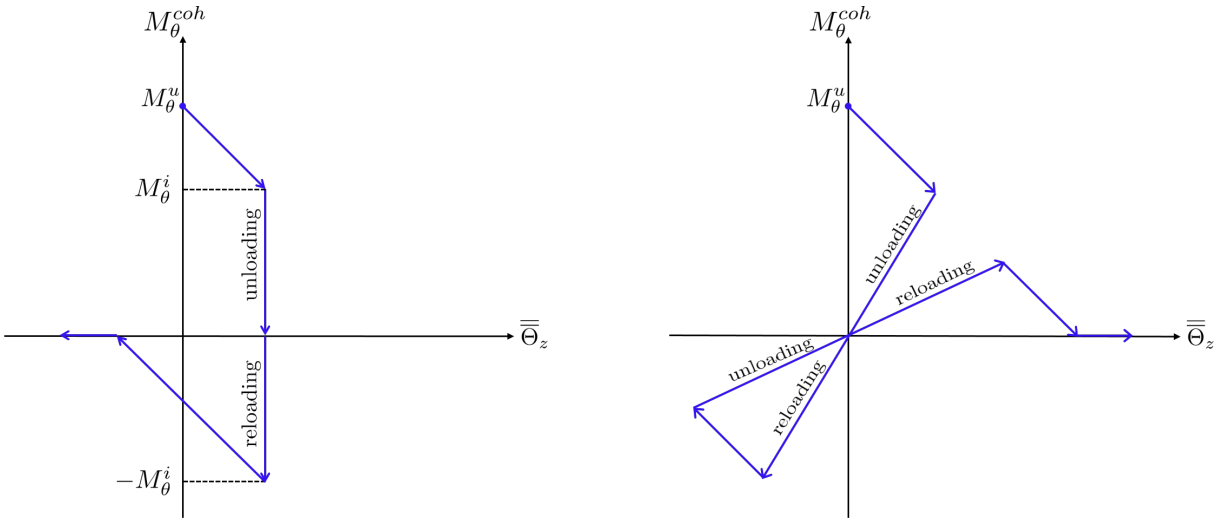

(a) Plastic type softening model (b) Damage type softening model

Figure 4.4: Cyclic loading of alternate sign: plastic hinge moment – rotational jump relations.

plastic type softening model is adopted in order to take into account permanent strains. In order to illustrate the behavior of the chosen cohesive model under cyclic loads, in Figure 4.5 an example of the response of a 1D continuous model with linear hardening coupled to a cohesive model of plasticity type is presented.

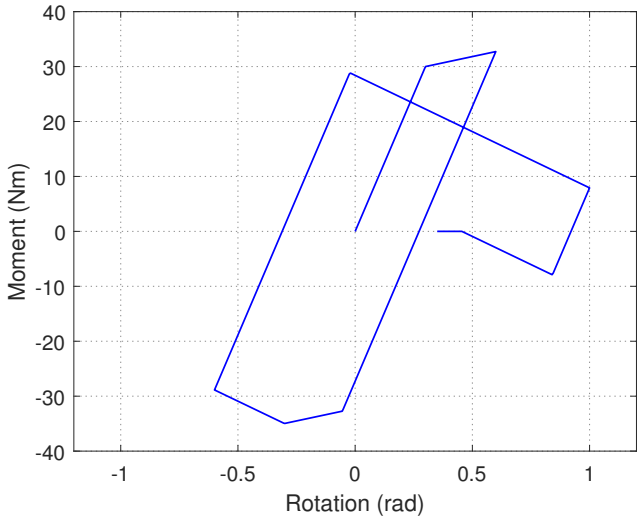

Figure 4.5: Cyclic loading: global response of a continuous model coupled to a cohesive model of plasticity type.

Stiffness degradation and the pinching effect are taken into account by modification of the unloading modulus of the continuous model (section 3.5). In particular, it is assumed that when the cohesive model is activated, the RC section has reached a high level of damage and its behavior is mainly controlled by the reinforcing steel behavior. Thus, the stiffness of the RC section is represented by the one of the steel and unloading stiffness is equal to the one of the steel rebars.

4.3.2 Parameter identification

As stated in Section 4.3.1, the constitutive description of the cohesive zone is given by a traction-separation law, the area under which corresponds to the fracture energy. This energy is a material property and for example for concrete, it is often considered between $70 - 150N/m$ (Matallah and La Borderie 2009). For a RC section however, the fracture energy is not a material property and it cannot be used to explicitly identify the softening modulus of the cohesive moment-rotational jump relation. On the other hand, it is preferable not to use the 3D model presented in Chapter 2 to get the softening modulus, the reason being that the Hilleborg type regularisation was not applied for the compression softening brunch.

As mentioned in Section 4.1, Pham et al. 2010, Pham et al. 2013 identified the parameters of the global flexural cohesive model by conducting numerical simulations. The authors used an enhanced multi-fiber Timoshenko finite element beam, enriched by discontinuities at the fiber level for sectional analysis of imposed rotation until failure. The constitutive description of the materials was given at a local level, in terms of stress-strain for the continuous part and in terms of traction-separation laws for the discontinuous part. Results showed a strong influence of the axial force on the moment-curvature response and in particular on the softening modulus, Figure 4.6.

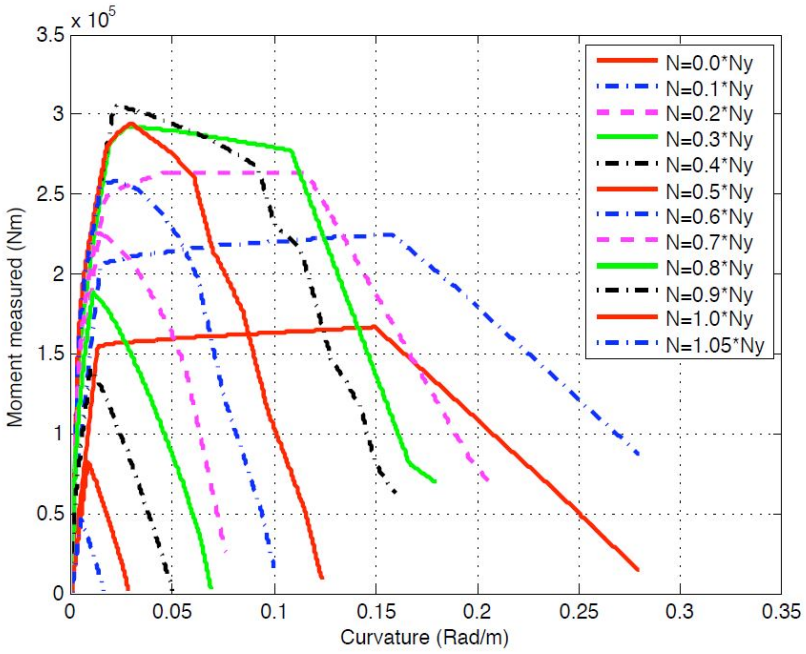

Figure 4.6: Moment-curvature relations for different levels of axial force, obtained by enhanced multi-fiber beam calculations (Pham et al. 2010).

The softening modulus of the cohesive moment-rotational jump relation is approximately estimated based on two choices which are tested in Chapter 5. The first choice is the approximation of the softening modulus as -7% of the initial flexural modulus, according to Haselton 2006. The second choice is used ad hoc to capture the RC sectional response during cyclic loadings. In this case the softening modulus is taken equal to -0.7% of the initial flexural modulus.

In the following and in order to identify the ultimate rotational capacity Θ_z^{act} (in percent) of Equation (4.17), the analytical relation provided in Park et al. 1987 is used and is based on regression analysis on data from experimental testing of RC components of rectangular sections:

$$\Theta_z^{act}(\%) = 0.52(L/d)^{0.93}\rho^{-0.27}\rho_w^{0.48}n_o^{-0.48}f_c^{-0.15} \tag{4.19}$$

with:

- L/d the shear span ratio (L is the length of the RC element and d is the depth of the RC section).

- ρ the normalized steel ratio, defined as: $\frac{A_s}{A_c}\frac{f_y}{f_c}$ (A_s is the area of the longitudinal reinforcement in tension and A_c is the cross-sectional area).
- f_c the concrete compressive strength in ksi.
- f_y the steel yield limit in ksi.
- n_o the normalized axial force defined as: P/P_o, with P being the axial force (positive for compression) and $P_o = bdf_c$ (b is the width and d is the depth of the column).
- ρ_w the confinement ratio in percent, defined as: $\frac{100A_{sx}}{bs_h}$ (A_{sx} is the area of the transverse steel parallel to the direction of loading and s_h is the spacing of the stirrups).

The critical value assigned to the curvature for the chosen activation criterion (Equation (4.18)) is given by:

$$\kappa_\theta^{act} = \frac{\Theta_z^{act}}{100L} \tag{4.20}$$

where L is the length of the RC element.

4.3.3 Integration algorithm

As stated in Ehrlich and Armero 2005, the enhanced by strong discontinuities approach is considered as a tool for the modeling of the localized dissipative mechanisms when localized failures occur and allows for capturing energy dissipation in the large-scale problem. Thus, the displacement jump presents similar role to an internal variable in an inelastic model and for the numerical resolution of the flexural cohesive model within the plasticity framework, a backward (or implicit) Euler scheme of the Return Mapping Algorithm families is used. The numerical implementation and the computational procedure (including static condensation at an elementary level) adopted are identical to the work of Bitar et al. 2018b. In the following, the integration algorithm of the cohesive model is briefly presented.

The adopted cohesive model is a linear type plastic softening law (see Figure 4.3(a)) that describes the relationship between the cohesive moment M_θ^{coh} and the rotational jump $\overline{\overline{\Theta}}_z$:

$$M_\theta^{coh} = M_\theta^u + S\overline{\overline{\Theta}}_z \tag{4.21}$$

where S is the softening modulus (of negative value). The activation criterion is given by:

$$f_c = |M_\theta^{coh}| - (M_\theta^u + S\overline{\overline{\Theta}}_z) \leq 0 \tag{4.22}$$

It is assumed that when the rotational discontinuity is activated, it remains activated for the rest of the loading history and the failure criterion is the same as the activation criterion f_c. The evolution of the elementary variable of the rotational jump is given by:

$$\dot{\overline{\overline{\Theta}}}_z = \dot{\overline{\overline{\lambda}}} sign(M_\theta^{coh}) \tag{4.23}$$

where $\dot{\overline{\overline{\lambda}}}$ is the plastic multiplier defining the magnitude of the rotational jump rate. The persistency condition expresses that once the discontinuity is activated the plastic multiplier $\dot{\overline{\overline{\lambda}}}$ is positive and thus the failure criterion is satisfied. This implies that:

$$\begin{aligned}
&\dot{\overline{\overline{\lambda}}} \dot{f}_c = 0 \Rightarrow \dot{f}_c = 0 \Rightarrow \\
&|\dot{M}_\theta^{coh}| - S\dot{\overline{\overline{\Theta}}}_z = 0 \Rightarrow |\dot{M}_\theta^{coh}| - S\dot{\overline{\overline{\lambda}}} sign(M_\theta^{coh}) = 0 \Rightarrow \\
&\dot{\overline{\overline{\lambda}}} = \frac{1}{S}|\dot{M}_\theta^{coh}| \Rightarrow \dot{\overline{\overline{\lambda}}} = \frac{1}{S}\dot{M}_\theta^{coh} sign(M_\theta^{coh})
\end{aligned} \tag{4.24}$$

and therefore the expression for the calculation of the plastic multiplier is known. The

cohesive model internal variable $\overline{\overline{\Theta}}_z$ is computed at every time step (once the ctivation criterion is satified) for every Gauss point at every iteration k. The eleastic predictor of the current step $n+1$ is equal to the previous step n value:

$$\overline{\overline{\Theta}}^{trial}_{z_{n+1}} = \overline{\overline{\Theta}}_{z_n} \tag{4.25}$$

and the trial cohesive moment is given by the following expression:

$$M^{coh,trial}_{\theta_{n+1}} = -\int_{L_e} \overline{G}^{\kappa}_{v3}(x) M^{trial}_{\theta_{n+1}}(x) dx = -\frac{L_e}{2} \sum_{pg=1}^{npg} \overline{G}^{\kappa}_{v3}(x_{pg}) M^{trial}_{\theta_{n+1}}(x_{pg}) w(x_{pg}) \tag{4.26}$$

where npg is the number of integration points of the beam element, $w(x_{pg})$ is the integration weight of point x_{pg} and $\overline{G}^{\kappa}_{v3}$ is the enhanced shape function for the virtual discontinuity variable. In the general case $\overline{G}^{\kappa}_{v3}$ and $\overline{G}^{\kappa}_{r3}$ are different. However for the present formulation these functions are identical. The expression of $M^{trial}_{\theta_{n+1}}(x_{pg})$ is:

$$M^{trial}_{\theta_{n+1}}(x_{pg}) = K_{\theta}(x_{pg}) \left(\underline{B}^{\kappa} \underline{U}^{k-1}_{e_{n+1}} + \overline{G}^{\kappa}_{r3}(x_{pg}) \overline{\overline{\Theta}}^{trial}_{z_{n+1}} - \kappa^{pl}_{\theta_n} \right) \tag{4.27}$$

The trial failure criterion is evaluated:

$$f^{trial}_{c_{n+1}} = |M^{coh,trial}_{\theta_{n+1}}| - (M^{u}_{\theta} + S\overline{\overline{\Theta}}^{trial}_{z_{n+1}}) \leq 0 \tag{4.28}$$

If this condition (4.28) holds the discontinuity is not activated and thus the variables of the cohesive model are updated as:

$$\begin{aligned} \overline{\overline{\Theta}}_{z_{n+1}} &= \overline{\overline{\Theta}}^{trial}_{z_{n+1}} \\ M^{coh}_{\theta_{n+1}} &= M^{coh,trial}_{\theta_{n+1}} \end{aligned} \tag{4.29}$$

If discontinuity is activated the rotational jump at the current step is given by:

$$\overline{\overline{\Theta}}_{z_{n+1}} = \overline{\overline{\Theta}}_{z_n} + \dot{\overline{\overline{\lambda}}} sign(M^{coh,trial}_{\theta_{n+1}}) \tag{4.30}$$

The updated cohesive force at the step $n+1$ can be expressed as:

$$\begin{aligned} M^{coh}_{\theta_{n+1}} &= -\int_{L_e} \overline{G}^{\kappa}_{v3}(x) M_{\theta_{n+1}}(x) dx \\ &= -\int_{L_e} \overline{G}^{\kappa}_{v3}(x) K_\theta \left(\underline{B}^{\kappa}(x) \underline{U}_{e_{n+1}} + \overline{G}^{\kappa}_{r3}(x) \overline{\overline{\Theta}}_{z_{n+1}} - \kappa^{pl}_{\theta_n} \right) dx \\ &= \underbrace{-\int_{L_e} \overline{G}^{\kappa}_{v3}(x) K_\theta \left(\underline{B}^{\kappa}(x) \underline{U}_{e_{n+1}} + \overline{G}^{\kappa}_{r3}(x) \overline{\overline{\Theta}}_{z_n} - \kappa^{pl}_{\theta_n} \right) dx}_{M^{coh,trial}_{\theta_{n+1}}} \underbrace{-\int_{L_e} \overline{G}^{\kappa}_{v}(x) K_\theta \overline{G}^{\kappa}_{r3}(x) dx \Delta \overline{\overline{\Theta}}_z}_{K_m} \end{aligned} \tag{4.31}$$

and thus:

$$M^{coh}_{\theta_{n+1}} = M^{coh,trial}_{\theta_{n+1}} - K_m \dot{\overline{\overline{\lambda}}} sign(M^{coh,trial}_{\theta_{n+1}}) \tag{4.32}$$

The above expression allows for the calculation of the plastic multiplier:

$$\dot{\overline{\overline{\lambda}}} = \begin{cases} \dfrac{f^{trial}_{c_{n+1}}}{K_m + S} \text{ if } |S\overline{\overline{\Theta}}_{z_n}| < M^u_\theta \\ \dfrac{|M^{coh,trial}_{\theta_{n+1}}|}{K_m} \text{ if } |S\overline{\overline{\Theta}}_{z_n}| = M^u_\theta \end{cases} \tag{4.33}$$

and the cohesive tangent modulus is defined as:

$$\frac{dM^{coh}_{\theta_{n+1}}}{d\overline{\overline{\Theta}}_z} = \begin{cases} \text{not defined if } \dot{\overline{\overline{\lambda}}} = 0 \\ S \text{ if } \dot{\overline{\overline{\lambda}}} > 0 \text{ and } |S\overline{\overline{\Theta}}_{z_{n+1}}| < M^u_\theta \\ 0 \text{ if } \dot{\overline{\overline{\lambda}}} > 0 \text{ and } |S\overline{\overline{\Theta}}_{z_{n+1}}| = M^u_\theta \end{cases} \tag{4.34}$$

Chapter 5

Numerical applications

A novel macroelement was proposed in Chapter 3, built within the plasticity framework in terms of axial force, shear force and bending moment. The model is based on the numerical results of Chapter 2 and the resulting 3D failure surface. Suitable modifications have been proposed to account for stiffness degradation during cyclic loading of constant and alternate sign. An enhanced (strong discontinuities) formulation was introduced in Chapter 4 together with a global cohesive model. The different tools have been integrated within a Timoshenko beam finite element. The calibration procedure of all the model parameters was given based on simplified methods, as the purpose of this work is to provide a user-oriented numerical tool for everyday engineering applications and practitioners. The proposed numerical tools allow for modeling the response of Reinforced Concrete (RC) frame structures up to failure submitted to static (monotonic or cyclic) or dynamic severe loading.

The performance of the novel macroelement integrating all the above features is tested in this Chapter. In particular, four (4) representative case studies demonstrate the efficiency of the macroelement under static (monotonic and cyclic loads of constant and alternate sign) and dynamic loading, up to failure.

5.1 Case studies

5.1.1 RC cantilever columns

RC cantilever column S1 (Bousias et al. 1995)

The first case study is the RC cantilever column experimentally studied by Bousias et al. 1995 (already modeled in Chapter 2 using a 3D finite element model). The column geometry and the reinforcement details were shown in Figure 2.5, reproduced hereafter in Figure 5.1 for convenience.

During the experimental campaign, the cantilever column was subjected to biaxial

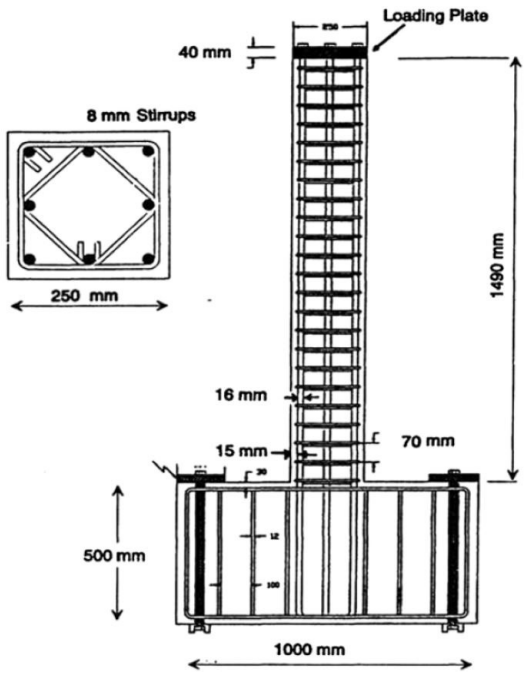

Figure 5.1: RC cantilever column: geometry and reinforcement details (Gutierrez et al. 1993).

bending under an axial force. The experimental results of the S1 test showed however that the response was similar in both bending directions (see Figure 2.12). As the proposed macroelement formulation is capable of reproducing the sectional behavior under in-plane loading conditions, the numerical simulation of the cyclic test S1 is presented hereafter considering the loading history of only one direction, according to Figure 5.2.

Five (5) preliminary numerical simulations with different number of beam elements (2, 4, 8, 16, 32) took place in order to investigate the mesh dependency problem. The axial load is imposed by a constant force, while transversal displacement increments of $0.06mm$ are applied at the free edge of the column. The parameters of the macroelement are presented in Table 5.1.

Figure 5.3 presents the numerical results for monotonic application of the transversal load, by using 2, 4, 8, 16 and 32 beam elments . As it is observed, the solutions coincide for four (4) elements and finer discretisations. Thus, in order to optimize the time calculation performance, four (4) FLI Timoshenko beams of $0.375m$ length are used as a final choice for the spatial discretisation (see Figure 5.4 for the chosen mesh and the boundary conditions).

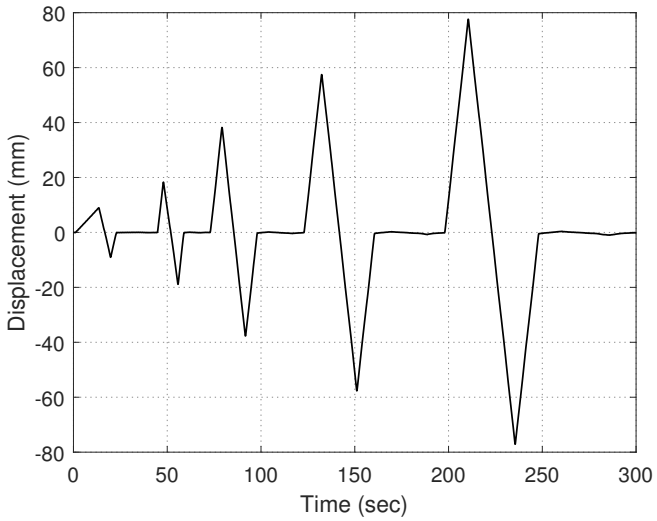

Figure 5.2: RC cantilever column S1: loading history (one direction).

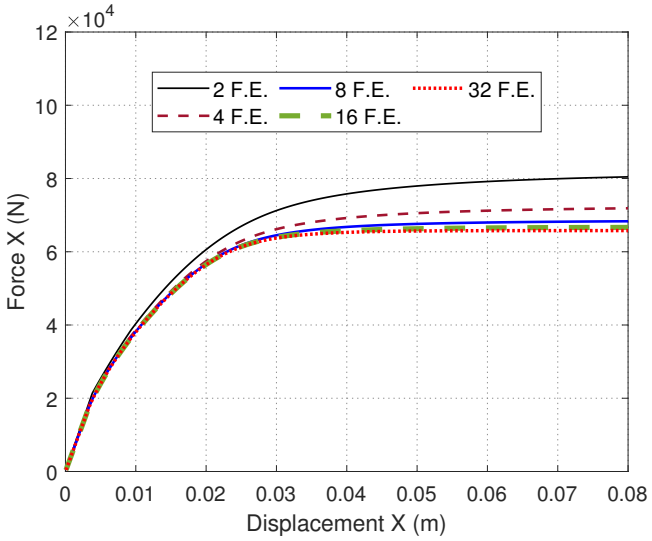

Figure 5.3: RC cantilever column S1: Numerical global response depending on the number of the elements (monotonic loading).

The numerical versus the experimental results for monotonic and cyclic loading of constant and alternate sign (Figure 5.2) are presented hereafter. The monotonic response is accurately reproduced in Figure 5.5. According to Bousias et al. 1995 a monotonic test can be considered as an envelope to the hysteresis loops. The difference between the two experimental curves is due to the slightly lower concrete compressive strength and

Table 5.1: Macroelement parameters for the RC cantilever column S1

Description	**Parameter**	**Value**	**SI Unit**
Linear elastic behavior			
Axial stiffness	K_x	1.21 e09	N
Shear stiffness	K_y	5.03 e08	N
Flexural stiffness	K_θ	6.01 e06	Nm^2
Axial elastic limit	r_{x0}	0.37	–
Shear elastic limit	r_{y0}	0.37	–
Flexural elastic limit	$r_{\theta 0}$	0.37	–
Standardization			
Maximum axial tensile force	$F^t_{x,max}$	1.38 e06	N
Maximum axial compressive force	$F^c_{x,max}$	−2.72 e06	N
Shear shift parameter	F^*_y	9.28 e04	N
Flexural shift parameter	M^*_θ	1.08 e05	Nm
Hardening evolution laws			
Axial rate of hardening	a_x	500	–
Shear rate of hardening	a_y	250	–
Flexural rate of hardening	a_θ	250	–
Stiffness degradation (cyclic loading of constant sign)			
Axial stiffness of steel	K_x^{steel}	2.90 e08	N
Shear stiffness of steel	K_y^{steel}	1.11 e08	N
Flexural stiffness of steel	K_θ^{steel}	1.92 e06	Nm^2
Stiffness degradation (cyclic loading of alternate sign)			
Geometrical property of the rebars	c_1	0.3	–
Mechanical property of the steel	c_2	620	–
Cohesive model			
Concrete compressive strength	f_c	4.21	ksi
Steel yield limit	f_y	66.72	ksi
Normalized axial force	n_o	0.12	–
Normalized steel ratio	ρ	0.153	–
Depth of the section	d	0.25	m
Shear span ratio	L/d	6	–
Confinement ratio in percent	ρ_w	5.75%	–
Softening modulus	S	−4.21 e05	Nm
Softening modulus (ad hoc)	S	−4.21 e04	Nm

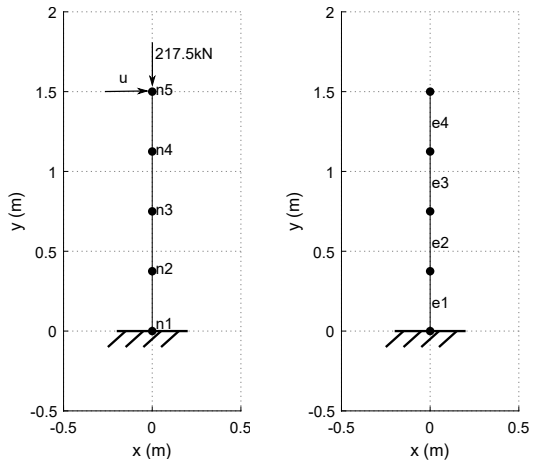

(a) nodes (b) elements

Figure 5.4: RC cantilever column S1: mesh and boundary conditions.

compressive axial force values of the monotonic test ($23.9MPa$ and $164.3kN$ respectively) with respect to the ones of the ones of the cyclic test ($29.0MPa$ and $217.5kN$ respectively). The calculation time for the simulation of the monotonic test was 5.5 minutes.

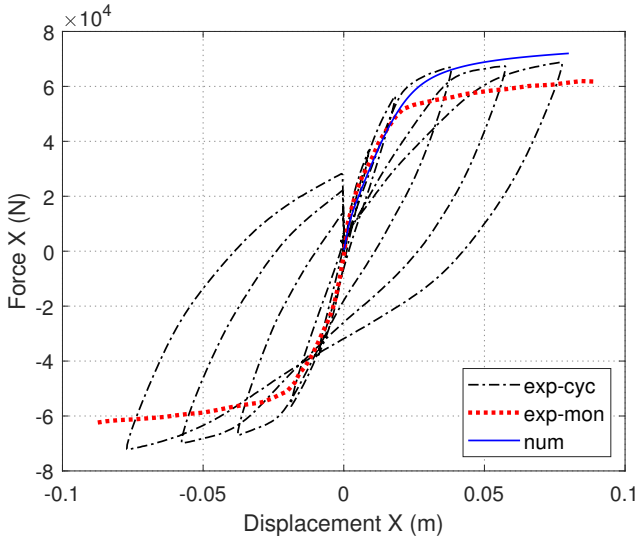

Figure 5.5: RC cantilever column S1: Numerical vs. experimental global response (monotonic loading).

For the cyclic loading without change of sign, (Figure 5.6), the macroelment represents sufficiently loading and unloading response. As it was assumed in section 3.5, the global response of the RC column is dominated by the reinforcing steel at late stages of the loading history (the stiffness components are modified to the ones of the reinforcing steel).

The calculation time for this test was 7.5 minutes.

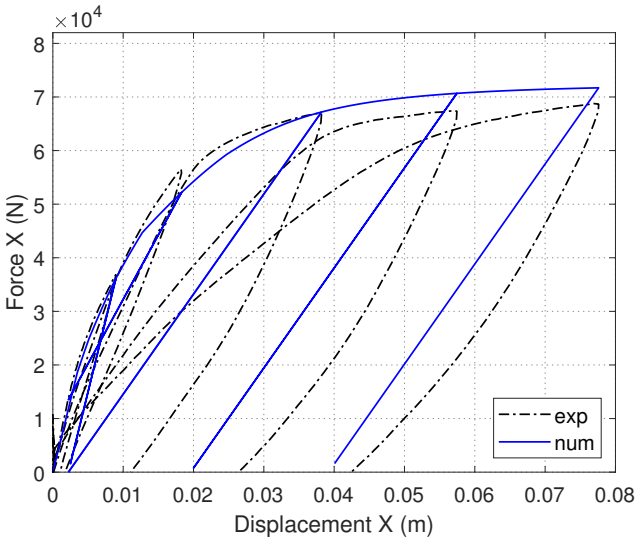

Figure 5.6: RC cantilever column S1: Numerical vs. experimental global response (cyclic loading of constant sign).

For the cyclic loading of aletrnate sign, both approaches discussed in section 3.5 have been applied for the numerical simulation of the experimentally tested RC column: considering stiffness degradation based on the constitutive relation of Menegotto and Pinto 1973 in Figure 5.7 and additionnaly the pinching effect based on the simplified approach describing three different stages of the response, in Figure 5.8.

For the cyclic loading, when the first approach is considered (Figure 5.7), the model is again capable of capturing the peaks of each loading cycle and the stiffness degradation during unloading. During the reloading stages however, the model overestimates the response. This is probably due to the linear unloading slope and the fact that the model does not integrate a kinematic hardening law because such a choice would lead to inerpenetration of the failure surface by the loading surface (see section 3.2.2). In particular, in late stages of loading, the response is mainly controlled by the behavior of the reinforcement bars where the Bauschinger effect is predominant.

The calculation time for this simulation (cyclic test of alternate sign adopting the first approach) was 1.8 hours, while the simulation conducted with the 3D model built in section 2.1 using the Cast3M finite element code, to numerically reproduce the same experiment, was 14.8 hours, noting that Cast3M uses an automatic substepping strategy by default. Taking into account that GemLab (the research finite element code in which

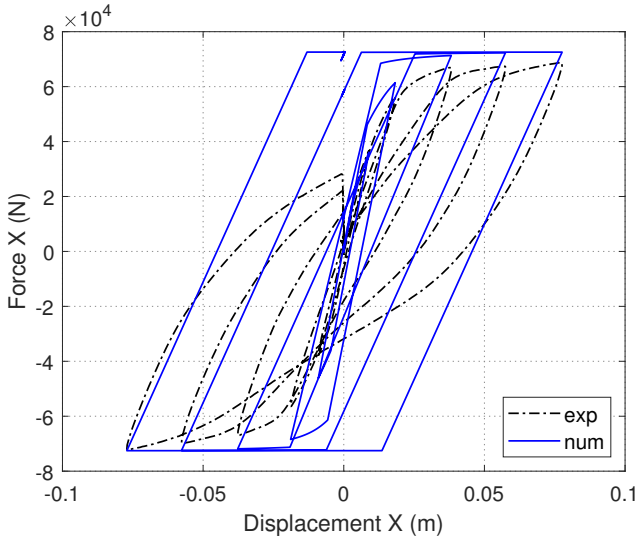

Figure 5.7: RC cantilever column S1: Numerical (1^{st} approach) vs. experimental global response (cyclic loading of alternate sign).

the Timoshenko beam and the macroelement are implemented) is based on Matlab program, the computational efficiency of the macroelement can be significantly improved if a software developed in compiled language (such as Fortran) is used instead and if an an automatic substepping strategy is applied.

Numerical versus experimental results of the cyclic test of alternate sign, by adopting the second approach of section 3.5 are presented in Figure 5.8. The calculation time for this simulation was 2.5 hours. The second approach captures the reloading stages in a more accurate way, compared to the first one (Figure 5.7). The second approach considers a reduced stiffness of 20% of the elastic stiffness during crack-reclosure. Alternatively, a reduced stiffness of 10% of the elastic stiffness during crack-reclosure is proposed as a result of calibartion procedure. The global response of the simulation conducted by application of this calibration is shown in Figure 5.9 together with the experimental results. As it is observed, the calibrated 2^{nd} approach provides a better fit to the experimental curve. However, such an abrupt stiffness reduction leads to numerical problems and loss of convergence and the simulation is not complete till the end of the loading history.

During all the above simulations the cohesive model was not activated, as the activation criterion of Equation (4.18) is not verified, given the loading histories applied on the RC column.

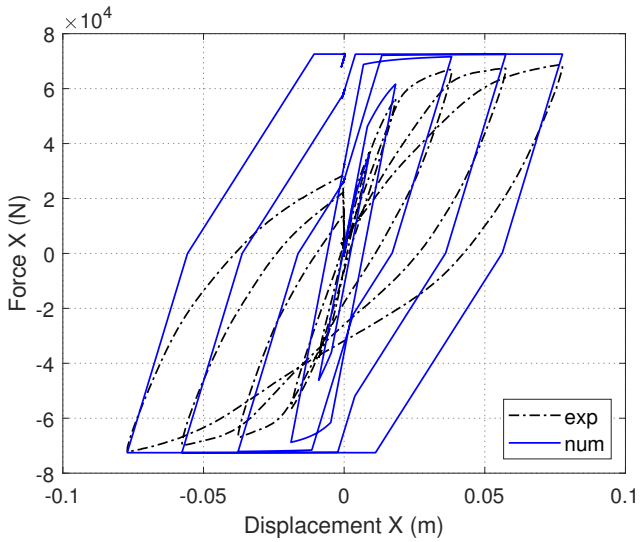

Figure 5.8: RC cantilever column S1: Numerical (2^{nd} approach) vs. experimental global response (cyclic loading of alternate sign).

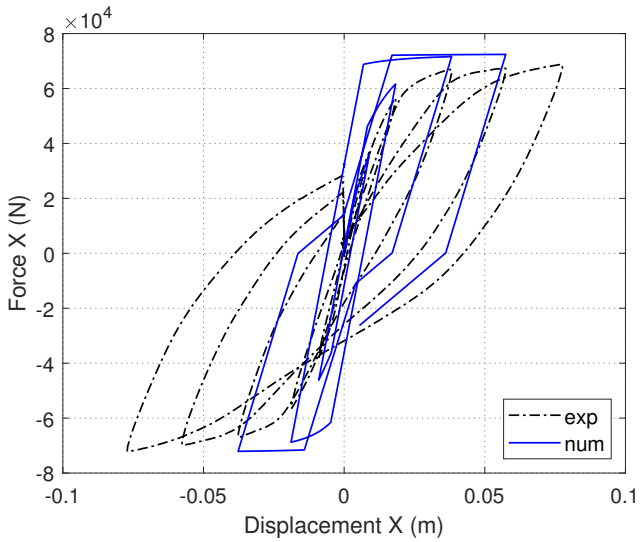

Figure 5.9: RC cantilever column S1: Numerical (calibrated 2^{nd} approach) vs. experimental global response (cyclic loading of alternate sign).

RC cantilever column (carbon steel) (Melo et al. 2019)

Melo et al. 2019 experimentally studied the performance of RC cantilever columns with carbon steel and stainless steel reinforcement bars under constant compressive axial load, monotonic and cyclic lateral loading conditions. In the following, the RC cantilever col-

umn with carbon steel is simulated. The geometry and the reinforcement details are given in Figure 5.10.

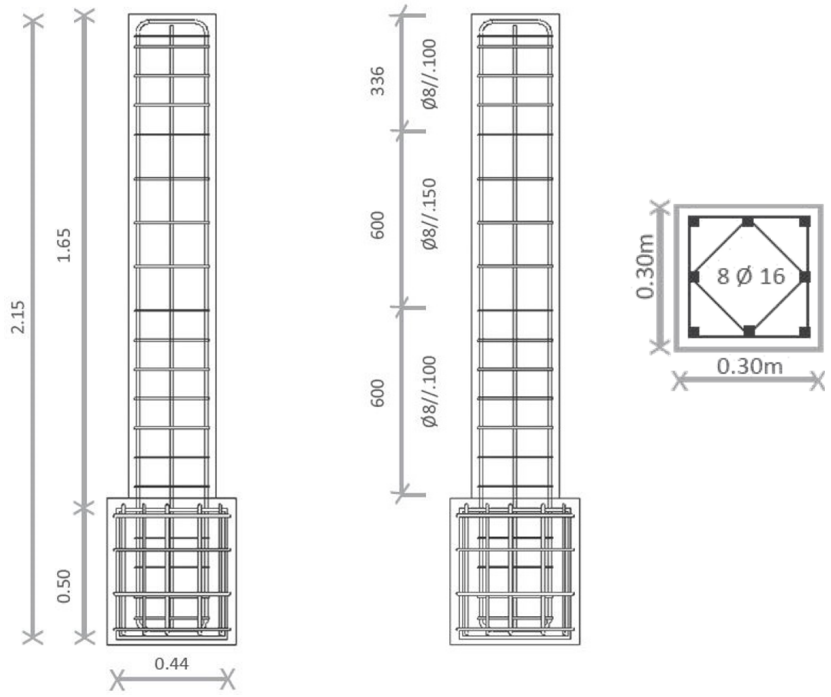

Figure 5.10: RC cantilever column (carbon steel): Specimen dimensions (left), shear reinforcement details (center) and cross-section of the specimen (right).

The lateral displacement loading history is provided in Figure 5.11.

Four (4) Timoshenko beam finite elements of $0.375m$ length are used for the spatial discretisation. A constant axial force is applied at the top of the model while the lateral load is displacement controlled (displacement increments of $0.1mm$). In Figure 5.12, the mesh and the boundary conditions are presented.

Numerical simulations took place for the three following cases:

1. the lateral load is monotonically applied.
2. the experimental lateral loading history is applied without change of sign.
3. the experimental lateral loading history is applied (Figure 5.11).

The macroelement parameters are presented in Table 5.2 for this case study.

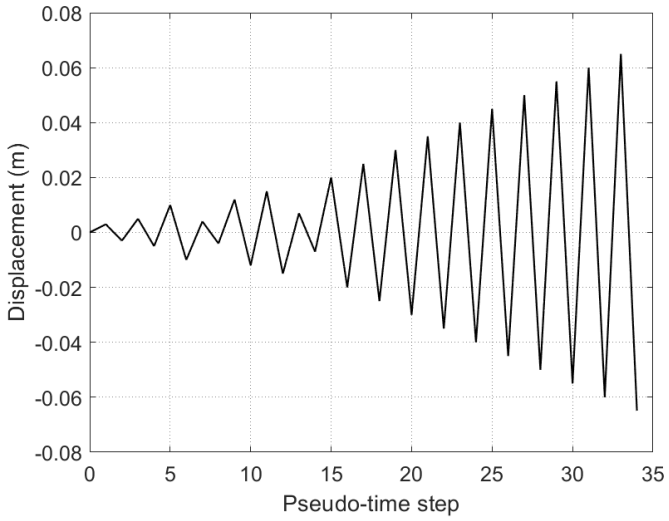

Figure 5.11: RC cantilever column (carbon steel): Lateral displacement loading history.

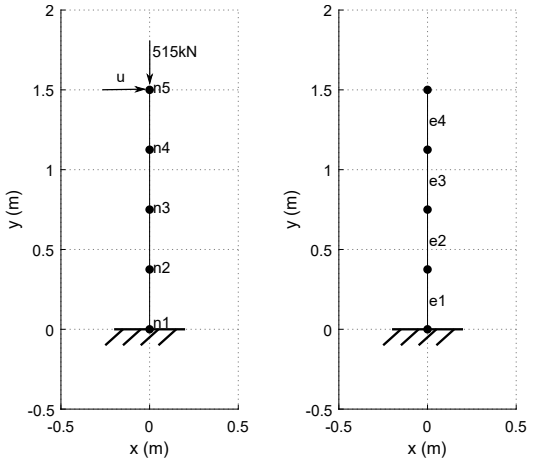

(a) nodes (b) elements

Figure 5.12: RC cantilever column (carbon steel): mesh and boundary conditions.

Comparison between the experimental and numerical results are presented for the three cases in Figures 5.13, 5.14 and 5.15 respectively. For each loading case, the numerical response is provided for the two choices of the softening modulus (see Section 4.3.2): as -7% and as -0.7% (ad hoc) of the initial flexural modulus. The calculation time for the three cases was 2, 3 and 19 minutes respectively.

Figure 5.13 presents the envelope of the (cyclic) experimental response compared with the monotonic macroelement results. It can be clearly seen that the macroelement ac-

Table 5.2: Macroelement parameters for the RC cantilever column (carbon steel)

Description	Parameter	Value	SI Unit
Linear elastic behavior			
Axial stiffness	K_x	3.17 e09	N
Shear stiffness	K_y	1.31 e09	N
Flexural stiffness	K_θ	2.32 e07	Nm^2
Axial elastic limit	r_{x0}	0.4	–
Shear elastic limit	r_{y0}	0.4	–
Flexural elastic limit	$r_{\theta 0}$	0.4	–
Standardization			
Maximum axial tensile force	$F^t_{x,max}$	9.25 e05	N
Maximum axial compressive force	$F^c_{x,max}$	−2.69 e06	N
Shear shift parameter	F^*_y	2.61 e05	N
Flexural shift parameter	M^*_θ	1.32 e05	Nm
Hardening evolution laws			
Axial rate of hardening	a_x	500	–
Shear rate of hardening	a_y	250	–
Flexural rate of hardening	a_θ	250	–
Stiffness degradation (cyclic loading of constant sign)			
Axial stiffness of steel	K^{steel}_x	3.33 e08	N
Shear stiffness of steel	K^{steel}_y	1.28 e08	N
Flexural stiffness of steel	K^{steel}_θ	1.98 e06	Nm^2
Stiffness degradation (cyclic loading of alternate sign)			
Geometrical property of the rebars	c_1	0.3	–
Mechanical property of the steel	c_2	620	–
Cohesive model			
Concrete compressive strength	f_c	3.63	ksi
Steel yield limit	f_y	83.40	ksi
Normalized axial force	n_o	0.515	–
Normalized steel ratio	ρ	0.154	–
Depth of the section	d	0.30	m
Shear span ratio	L/d	5	–
Confinement ratio in percent	ρ_w	0.67%	–
Softening modulus	S	−1.63 e06	Nm
Softening modulus (ad hoc)	S	−1.63 e05	Nm

curately represents the global response up to the peak. The initiation of the softening behavior is also satisfactorily approximated. The first estimation of the softening slope (as $-7\%EI$) is more abrupt than the experimental data, while for the second ad hoc approximation of the softening modulus (as $-0.7\%EI$) the post-peak response is overestimated.

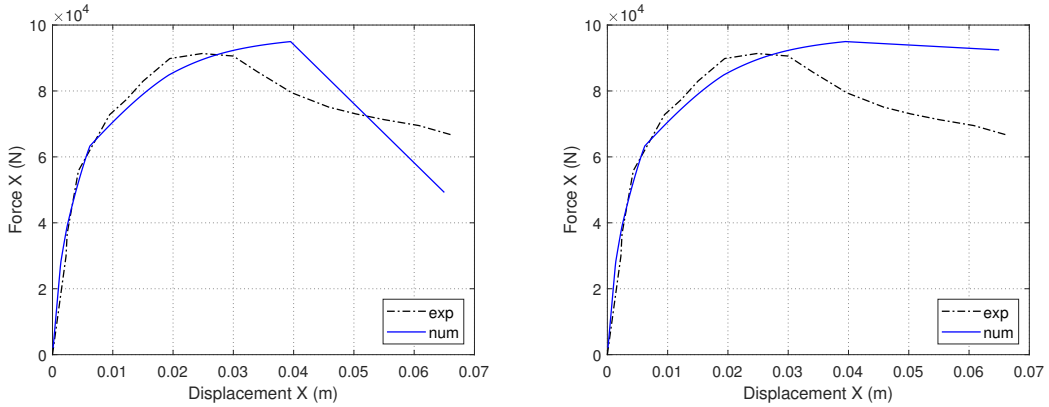

(a) $S = -7\%$EI (b) $S = -0.7\%$EI (ad hoc)

Figure 5.13: RC cantilever column (carbon steel): Numerical vs. experimental global response (monotonic loading).

For the cyclic loading without change of sign, (Figure 5.14), the macroelment represents sufficiently loading and unloading response. The global response of the RC column is again dominated by the reinforcing steel at late stages of the loading history. Softening initiation is correctly represented, while similar observations to the monotonic response concern the softening slope.

Finally, Figure 5.15 compares the numerical cyclic response with the experimental data considering both approximations of the softening modulus. It can be clearly seen that when cyclic loading conditions with change of signe are considered, the second estimation (ad hoc) of the softening modulus provides more accurate numerical results.

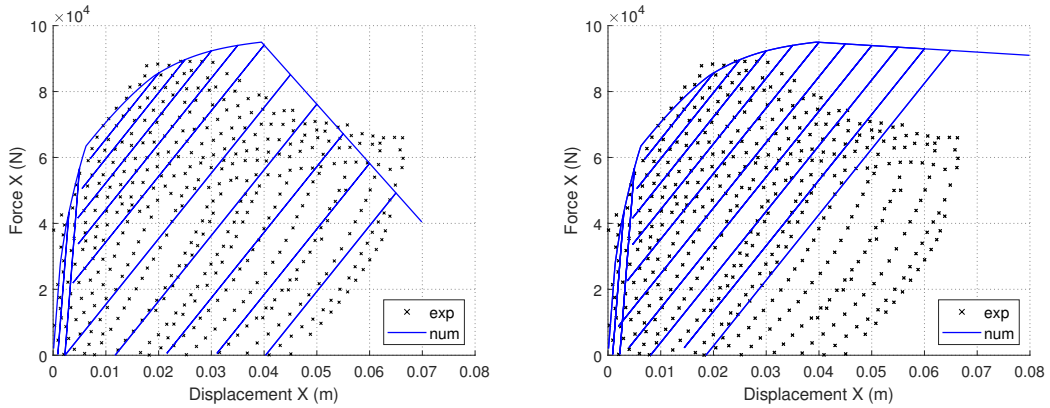

(a) $S = -7\%\text{EI}$ (b) $S = -0.7\%\text{EI}$ (ad hoc)

Figure 5.14: RC cantilever column (carbon steel): Numerical vs. experimental global response (cyclic loading of constant sign).

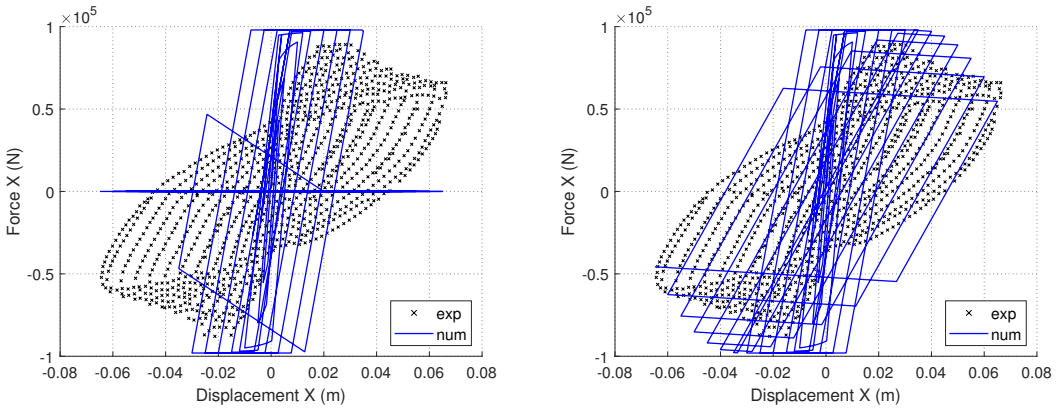

(a) $S = -7\%\text{EI}$ (b) $S = -0.7\%\text{EI}$ (ad hoc)

Figure 5.15: RC cantilever column (carbon steel): Numerical vs. experimental global response (cyclic loading).

In order to improve the response of the macroelement with the cohesive model, for this last case of cyclic loading of alternate sign, a calibration procedure of the macroelement parameters took place by changing the flexural rate of hardening a_θ to the value of 20, thus ameliorating the response until the peak. A different value is also assigned to the stiffness degradation parameter c_1 equal to 0.1 in order to improve the unloading/reloading response of the macroelement. Figure 5.16 shows that the whole response is significantly improved. The calculation time for this simulation was 15 minutes.

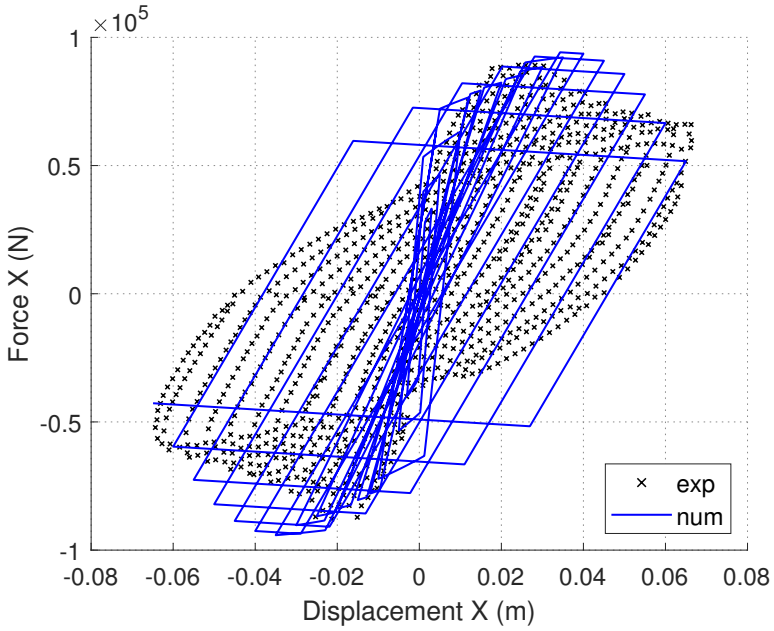

Figure 5.16: RC cantilever column (carbon steel): Numerical (calibrated) vs. experimental global response (cyclic loading) with the cohesive model.

5.1.2 RC plane frames

A two story RC frame (Vecchio and Emara 1992)

A two story RC frame was experimentally tested by Vecchio and Emara 1992. Its geometry and reinforcement details are depicted in Figure 5.17. All beam and columns sections have the same geometrical and material properties, the only difference being the concrete cover (concrete cover is $30mm$ for beams and $20mm$ for columns).

This structure has been often used for validation purposes (see for example Pham et al. 2013, Bui et al. 2014, Jukić et al. 2014, Bitar et al. 2018b). In these works, the researchers assigned different material parameters to the beams and the columns, justified by the fact that columns are submitted to axial compressive loads resulting to higher flexural resistances. This is not necessary for the macroelement as the coupling between the different stress-resultant components is explicitly taken into account via the 3D failure surface.

Thirty (30) finite elements of $0.5m$ length are used for the spatial discretization (seven (7) for each beam and eight (8) for each column). The columns are considered fixed at their base. Figure 5.18 presents the mesh and the boundary conditions.

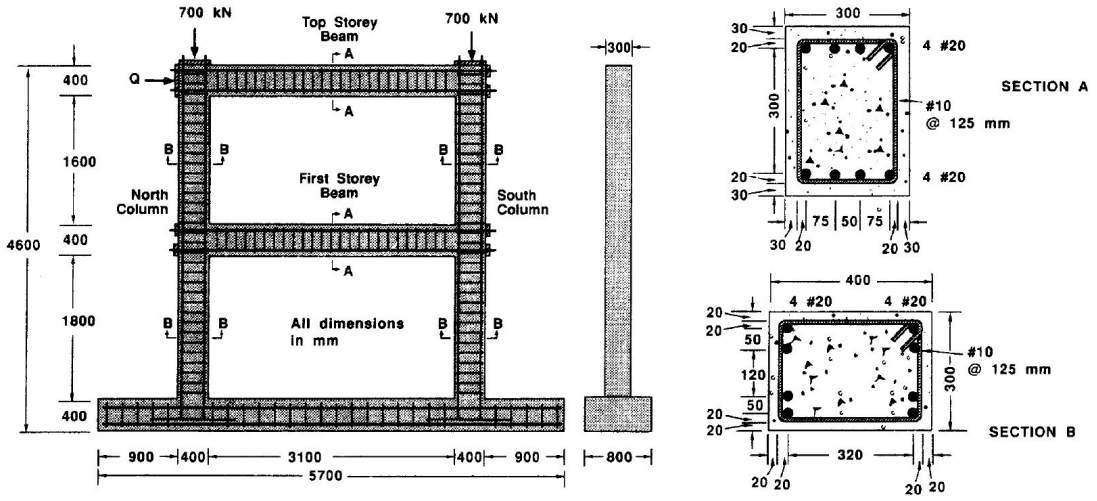

Figure 5.17: Two story RC frame: geometry and reinforcement details (Vecchio and Emara 1992).

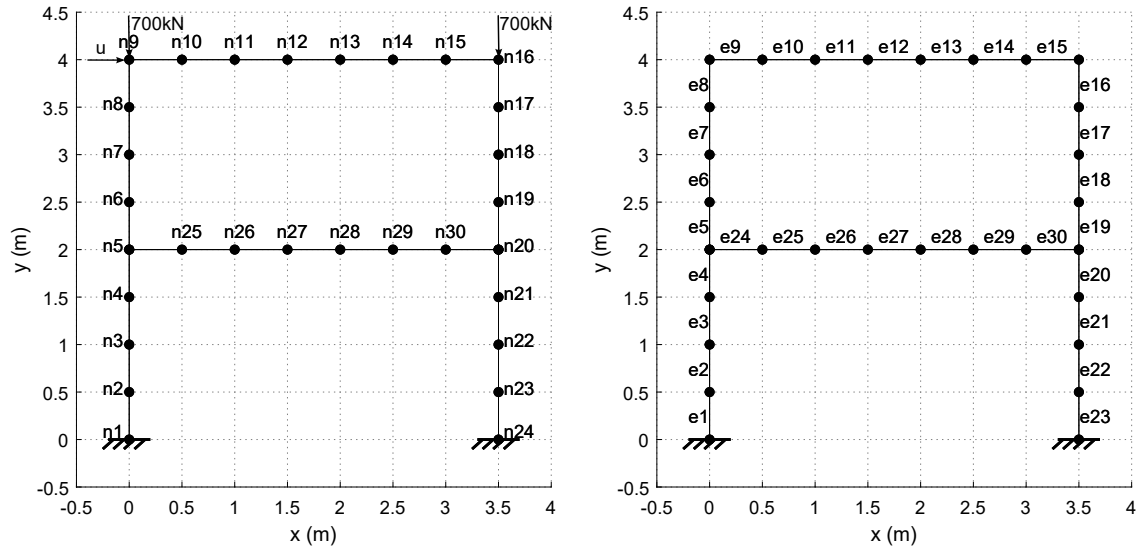

(a) nodes (b) elements

Figure 5.18: Two story RC frame: mesh and boundary conditions.

Numerical simulations are conducted for monotonic and cyclic (constant sign) lateral loads applied at the top of the frame, the latter to reproduce the experimental conditions. Equal constant axial loads are applied on top of the columns while lateral displacements are incrementally imposed at the top of the north column (displacement increments of $0.06mm$) (see Figure 5.17 and 5.18).

The macroelement calibrated parameters are given in Table 5.3.

Table 5.3: Macroelement parameters for the two story RC frame

Description	**Parameter**	**Value**	**SI Unit**
Linear elastic behavior			
Axial stiffness	K_x	3.92 e09	N
Shear stiffness	K_y	1.62 e09	N
Flexural stiffness	K_θ	5.67 e07	Nm^2
Axial elastic limit	r_{x0}	0.5	–
Shear elastic limit	r_{y0}	0.5	–
Flexural elastic limit	$r_{\theta 0}$	0.5	–
Standardization			
Maximum axial tensile force	$F^t_{x,_{max}}$	1.50 e06	N
Maximum axial compressive force	$F^c_{x,_{max}}$	−4.66 e06	N
Shear shift parameter	F^*_y	4.14 e05	N
Flexural shift parameter	M^*_θ	2.91 e05	Nm
Hardening evolution laws			
Axial rate of hardening	a_x	500	–
Shear rate of hardening	a_y	250	–
Flexural rate of hardening	a_θ	250	–
Stiffness degradation (cyclic loading of constant sign)			
Axial stiffness of steel	K^{steel}_x	4.84 e08	N
Shear stiffness of steel	K^{steel}_y	1.86 e08	N
Flexural stiffness of steel	K^{steel}_θ	1.09 e07	Nm^2
Cohesive model			
Concrete compressive strength	f_c	4.35	ksi
Steel yield limit	f_y	60.63	ksi
Normalized axial force	n_o	0.194	–
Normalized steel ratio	ρ	0.146	–
Depth of the section	d	0.40	m
Shear span ratio (beam & column)	L/d	8.75 & 5	–
Confinement ratio in percent	ρ_w	2.51%	–
Softening modulus	S	−3.97 e06	Nm
Softening modulus (ad hoc)	S	−3.97 e05	Nm

The numerical response is compared to the experimental one for monotonic and cyclic lateral loads in Figure 5.19 and Figure 5.21 respectively. The caclulation time for both these case studies was 10.5 hours.

Figure 5.19 shows that the macroelement successfully captures the peak of the response. The global numerical response is similar for the two choices of the softening modulus. Furthermore, in Figure 5.20, the global numerical response for $S = -7\%EI$ is plotted together with the contributions of the elements 8 and 16 (see Figure 5.18) until $0.3m$, at which there is lack of experimental data, only to better illustrate the behavior after the activation of the cohesive model for two elements, at late stage of the loading. It is shown that the cohesive model for the element 8 is activated when displacement becomes equal to $0.13m$, while the cohesive model for the element 16 is activated when displacement reaches the value of $0.19m$. Even though softening is not observed at the global response of Figure 5.19a there are elements that exhibit softening behavior.

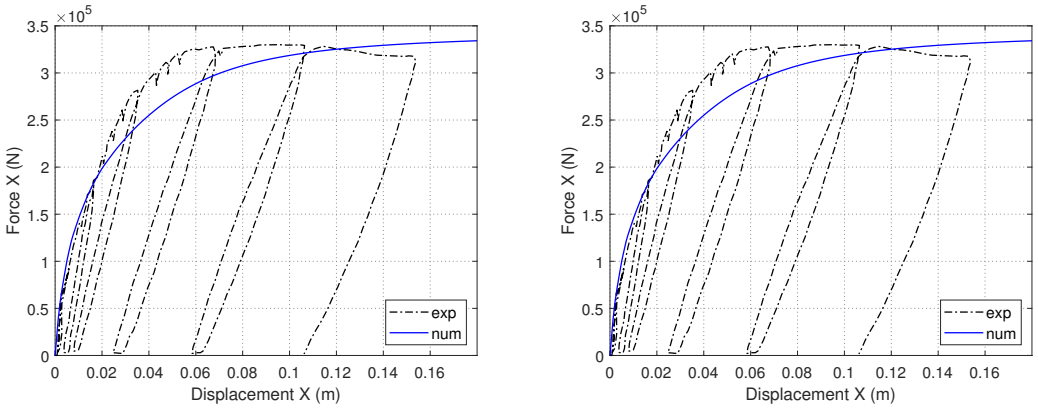

(a) $S = -7\%$EI (b) $S = -0.7\%$EI (ad hoc)

Figure 5.19: Two story RC frame: Numerical vs. experimental global response (monotonic loading).

Figure 5.21 shows that in this case (cyclic load without sign change), the macroelement is also able to accurately reproduce loading and unloading. Actually, the global response of the RC structure for severe loading is mainly controlled by the reinforcing steel. The modification of the stiffness components, such that they become equal to the reinforcement values when approaching failure, results to a realistic prediction of the cyclic response, as it was assumed in section 3.5.

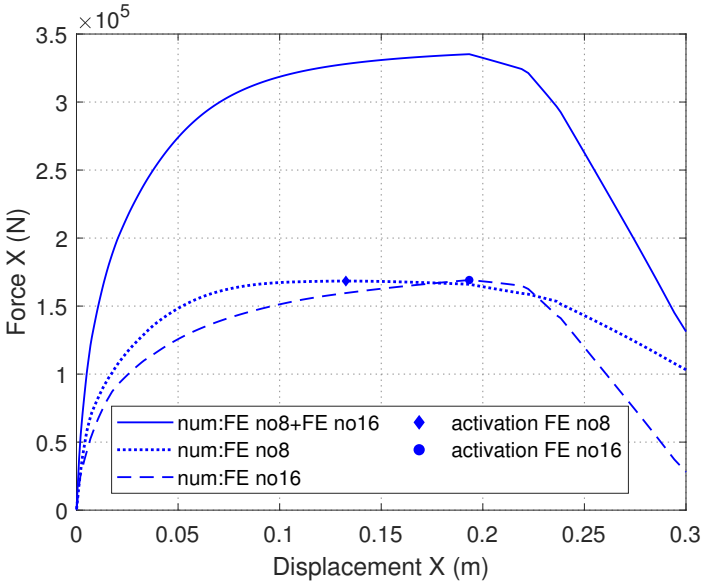

Figure 5.20: Two story RC frame: Numerical global response ($S = -7\%EI$): each element contribution (monotonic loading).

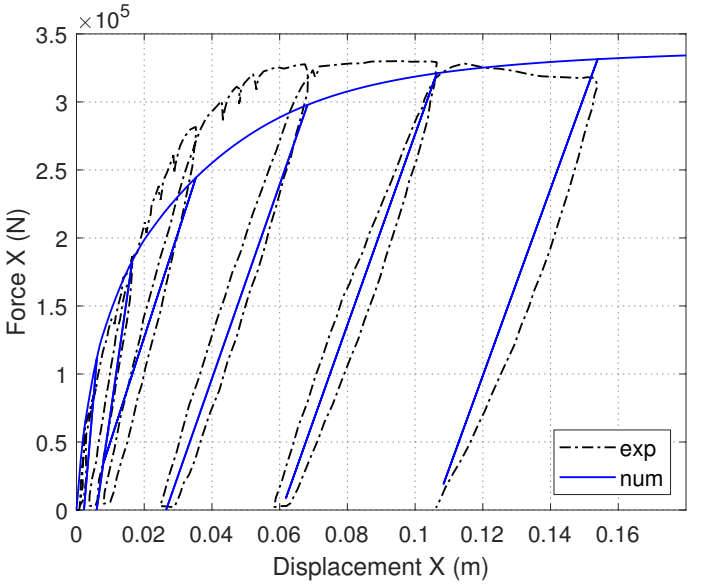

Figure 5.21: Two story RC frame: Numerical ($S = -7\%EI$) vs. experimental global response (cyclic loading with constant sign).

5.1.3 RC simply supported beam

A simply supported RC beam (Lebon 2011)

Lebon 2011 experimentally studied the intermidiate level beam as a part of a two story RC frame, during earthquake loading. During the experiment, pivot connections of the beam with the adjacent columns were assumed and thus the case study is a three-point bending test. The under study beam is sensitive only to a vertical earthquake loading and the experiment was conducted under a pseudodynamic condition i.e. without inertia and viscous effects. The geometry and reinforcing details of the beam are shown in Figure 5.22. The concrete cover is $0.01m$.

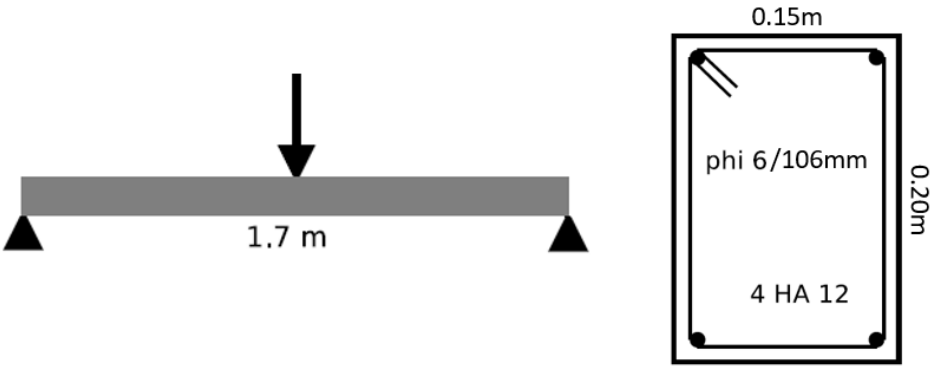

Figure 5.22: RC simply supported beam: geometry and reinforcement details (Lebon 2011).

The seismic loading is given by the vertical displacement time history. The imposed displacement versus time step curve is provided in Figure 5.23.

Four (4) Timoshenko beam finite elements of $0.425m$ length are used for the spatial discretisation. The vertical earthquake load is displacement controlled (displacement increments of $0.06mm$). In Figure 5.24, the mesh and the boundary conditions are presented.

The macroelement parameters are presented in Table 5.4 for this case study.

Table 5.4: Macroelement parameters for the RC simply supported beam

Description	**Parameter**	**Value**	**SI Unit**
Linear elastic behavior			
Axial stiffness	K_x	1.02 e09	N
Shear stiffness	K_y	4.21 e08	N
Flexural stiffness	K_θ	3.66 e06	Nm^2
Axial elastic limit	r_{x0}	0.7	–
Shear elastic limit	r_{y0}	0.7	–
Flexural elastic limit	$r_{\theta 0}$	0.7	–
Standardization			
Maximum axial tensile force	$F^t_{x,max}$	2.80 e05	N
Maximum axial compressive force	$F^c_{x,max}$	−1.13 e06	N
Shear shift parameter	F^*_y	8.67 e04	N
Flexural shift parameter	M^*_θ	3.86 e04	Nm
Hardening evolution laws			
Axial rate of hardening	a_x	500	–
Shear rate of hardening	a_y	250	–
Flexural rate of hardening	a_θ	250	–
Stiffness degradation (cyclic loading of alternate sign)			
Geometrical property of the rebars	c_1	0.3	–
Mechanical property of the steel	c_2	620	–
Cohesive model			
Concrete compressive strength	f_c	4.49	ksi
Steel yield limit	f_y	65.27	ksi
Normalized axial force	n_o	0.001	–
Normalized steel ratio	ρ	0.110	–
Depth of the section	d	0.20	m
Shear span ratio	L/d	4.25	–
Confinement ratio in percent	ρ_w	1.064%	–
Softening modulus	S	−2.56 e05	Nm
Softening modulus (ad hoc)	S	−2.56 e04	Nm

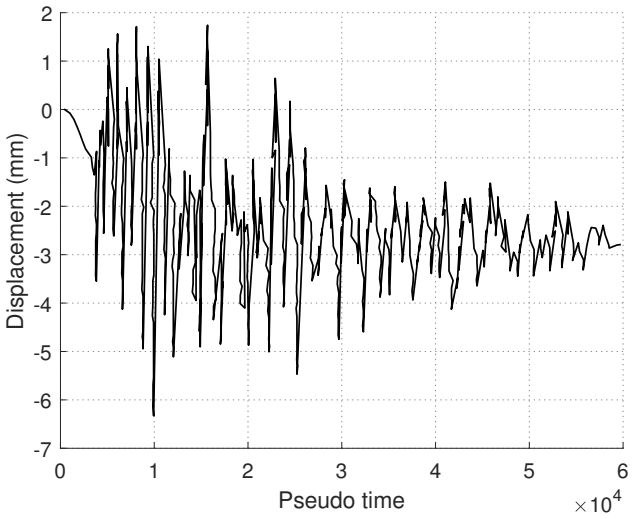

Figure 5.23: RC simply supported beam: Vertical displacement time history (Lebon 2011).

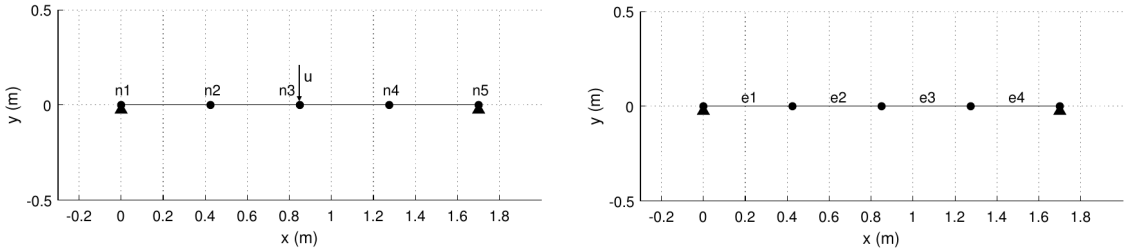

(a) nodes (b) elements

Figure 5.24: RC simply supported beam: mesh and boundary conditions.

Figure 5.25 compares the numerical response with the experimental data. The caclulation time for this simulation was 23 minutes. The cohesive model is not activated for this case study. Although the elastic phase is well captured, the macroelement at certain moments over/underestimates the response and a calibration procedure is necessary to achieve a more accurate response.

In order to improve the response of the macroelement, a different value is assigned to the stiffness degradation parameter $c1$, equal to 0.1. Figure 5.26 shows that by improving the unloading/reloading response, a better fit of the numerical response to the experimental curve is achieved at late stages of loading. The calculation time for this simulation was 12 minutes.

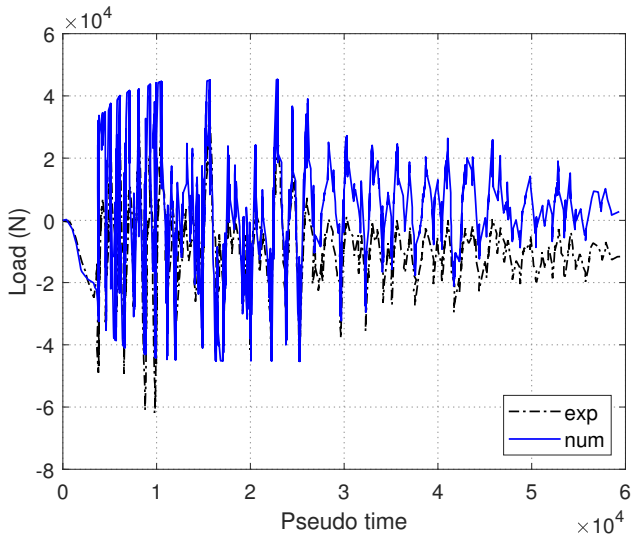

Figure 5.25: RC simply supported beam: Numerical vs. experimental load/time response.

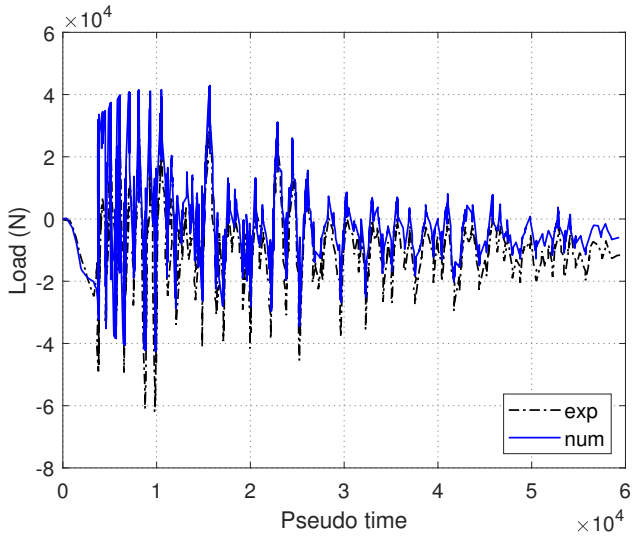

Figure 5.26: RC simply supported beam: Numerical (calibrated) vs. experimental load/time response.

5.2 Conclusions

The numerical performance of the novel macroelement has been tested considering different case studies. In all cases, the macroelement accurately captures the peak of the response and the initiation of the softening behavior. Under cyclic loading conditions of constant sign, the proposed modifications concerning the un/reloading modulus (sec-

tion 3.5) are efficient. When cyclic loading conditions of alternate sign are however imposed, the macroelement does not always provide satisfactory results, especially during the reloading stages. The proposed simplified calibration procedure of the softening modulus, at monotonic loadings or cyclic loads of constant sign gives more realistic predictions when the softening modulus is approximated as $S = -7\%\text{EI}$, while for cyclic loads of alternate sign, the ad hoc estimation of the softening modulus as $S = -0.7\%\text{EI}$ provides more accurate results.

Conclusions and perspectives

Conclusions

The purpose of this work was to provide the industrial partner with a simplified and robust numerical tool for predicting the response of reinforced concrete (RC) beams and columns under multiaxial loading conditions up to failure. The main features of the behavior of concrete and steel materials are described. At a structural level, the principal phenomena concerning the response during monotonic and cyclic loadings are explained.

The most common numerical approaches for simulating the response of RC elements are briefly presented by mentioning the advantages and disadvanatges of each method. Strain localization phenomenon is explained, as it appears during numerical simulations for materials that exhibit strain softening. The most popular remedies for localization problem and the resulting mesh dependency are presented.

The proposed numerical tool is a generalized Timoshenko beam finite element with linear independent shape functions. The advantages of such a choice rely on the reduced number of degrees of freedom, the consideration of shear strains and the fact that the sectional behavior is described by a unique homogeneous material, ensuring calculation speed. The reduced integartion technique of the elementary stiffness matrix is used, combined with one-point integration rule at the center of the element. Thus, the finite element is free of shear locking problem. However, the assumption of unique material cannot be directly applied to the case of RC structures as they are composed by different materials of concrete and steel. Therefore, one of the main objectives of this work was to deduce this behavior by numerical simulations.

Numerical simulations took place in a sufficiently accurate way via the finite element code Cast3M to deduce 3D interaction diagrams of a RC section in terms of axial force, shear force and in-plane bending moment. In particular, RC cantilever elements of symmetrical reinforcement were simulated until the peak of the response by imposing 3D loading combinations. 3D volumetric elements were used and all the components were geometrically modelled and their constitutive description was given in the 3D space as well. All the main features of concrete behavior were taken into account including asymmetry in uniaxial response, stiffness degradation, permanent strains in compression, unilateral

effect, strain softening in tension, strain hardening and softening in compression. Mesh objectivity was taken into account via a Hilleborg type approach concerning the tension softening behavior. The numerical model was firstly validated by simulations of experimentally studied by Bousias et al. cantilever columns. Subsequently, 3D interaction diagrams were numerically produced for sections of different reinforcement ratios and three characteristic states were identified: the first corresponding to the elastic domain of the section, the second to the elastic limit of the steel and the third to the peak values of the response. Analytical convex expressions were then computed for all the tested sections and for all the defined characteristic states.

These results offer two significant contributions: firstly, they can be directly exploitable by the engineers to provide an immediate result concerning the peak resistances of a RC symmetrically reinforced section and the intermediate state of the yielding of the steel rebars. Secondly, they can be used for the formulation of a generalized stress-resultant model describing the sectional behavior (macroelement) of a RC beam/column member, given the convexity of these expressions. Based on the latter advantageous possibility, a 3D macroelement was built within the plasticity framework to simulate the response until the peak. Three hardening laws of exponential type are used. The assymptotic character of these functions ensures that the failure surface cannot be interpenetrated by the loading surface. In addition to these, a method for calculating the algorithmic tangent modulus, by applying strain perturbations, was also proposed to improve the algorithmic efficiency and the calculation speed. The novelty of this macroelement is that it does not result from multi-scale analysis (see for example the recently developed model by Huguet et al. 2017) and it is coupling the three in-plane stress-resultant components, which cannot be found in other proposed global models such as the Takeda family models.

As for the response of RC frame elements from peak until failure, a kinematically enhanced formulation by strong discontinuity at the rotation field was adopted, representing the form of a plastic hinge. The developed macroelement was coupled to a global cohesive model, linking the cohesive moment to a rotation jump, similarly to a traction-separation law. The mathematical formulation of the adopted enhanced formulation was presented and a plastic softening law was selected for the constitutive description of the global cohesive model in order to account for permanent strains. For all the components of the macroelement, parameter identification procedures were discusssed and are mainly based on simplified methods to ensure user-oriented calibration of the model.

Numerical simulations took place to illustrate the performance of the proposed macroele-

ment. The results were compared to experimental ones. In a first place it was concluded that the macroelement accurately reproduces the peak of the response and it is sufficient to represent the behavior until the peak under monotonic and cyclic loading conditions of constant sign. For the latter loading conditions, the proposed modifications regarding the unloading stiffness are proved to be convenient. Nevertheless, when cyclic loading conditions of alternate sign are considered, the macroelement modeling is not satisfactory in all case studies and in some cases the reloading stage is not well represented.

Simplified approximations of the softening modulus were proposed. It has been shown that the estimation of the softening modulus as -7% of the initial flexural one provides satisfactory results for monotonic and cyclic loading histories of constant sign, while further reduction of the softening modulus, given as -0.7% of the initial flexural modulus results in more accurate results when cyclic loadings of alternate sign are considered.

Perspectives

There arise several perspectives from this work. Firstly, the influence of further investigating factors can be taken into account for the construction of failure envelopes. Such factors are steel strength, concrete compressive strength, consideration of non-perfect bonding between concrete and steel, ratio and position of the transversal reinforcement, section geometry and shape.

Other methodologies for the deduction of analytical convex expressions can be explored to reduce the degree of the failure surface, as surfaces of lower degree sush as ellipses are less troublesome in numerical integration algorithms.

The performance of the proposed macroelement can be improved during cyclic alternate loading conditions. For this, there are some possibilities concerning the framework within which the macroelement was built. Instead of classic plasticity, other approaches can be used such as generalized plasticity and bounding surface models (see for example the work of Pastor 1991 and Dafalias 1986, Dafalias and Herrmann 1986 respectively), used for modeling of soils.

A more precise methodology can be investigated for the identification of the softening modulus of the global cohesive model. This can be performed via multi-fiber simulations at a sectional level as it has been presented in the work of Pham et al. 2010 by adopting traction-separation laws for each fiber assigned to concrete and steel materials of the section.

Finally, the extension of the proposed macroelement formulation that takes into account the strain rate effect is another possibility in order to consider fast dynamic loads such as explosions. This can be achieved in a first place by the application of dynamic increase factors (DIF) at the failure surface coefficients, which is a common strategy adopted in the industry. For instance, El-Dakhakhni et al. 2009 constructed axial force–bending moment interaction diagrams for RC columns for different strain rates. Another more accurate possibility would be to repeat the whole numerical procedure for the construction of the interaction diagrams by adopting suitable constitutive laws for concrete and steel materials that consider the strain rate effect in their formulation and investigate the influence of the strain rate effect on the failure envelope and the intermidiate characteristic states.

ANNEX

A. Tests S2, S3, S4, S5, S7 and S9

Parameter	H_a		
Description	Kinematic hardening modulus		
	Reference value	**Calibration according to test S1**	**Best fit**
SI Unit	GPa	GPa	GPa
S2	2.3	20	14
S3	2.3	20	7
S4	2.3	20	7
S5	2.3	20	8
S7	2.3	20	10
S9	2.3	20	5

Table 5.5: RC columns: parametric study of the hardening modulus of the steel: tests S2, S3, S4, S5, S7 and S9.

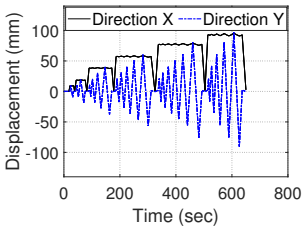

(a) Loading history

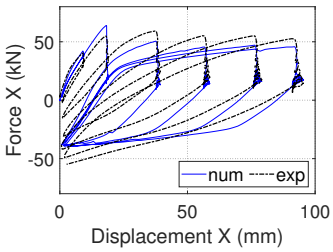

(b) Force-displacement, X direction

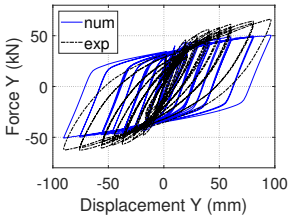

(c) Force-displacement, Y direction

Figure 5.27: Test S2: Numerical vs. experimental results: $H_a = 2.3GPa$.

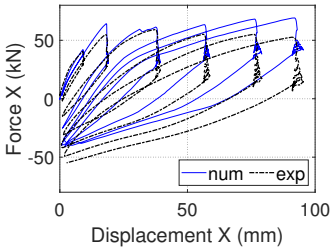

(a) Force-displacement, X direction

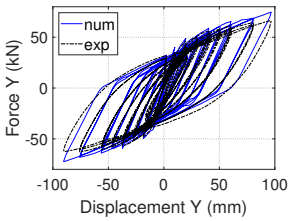

(b) Force-displacement, Y direction

Figure 5.28: Test S2: Numerical vs. experimental results: $H_a = 20GPa$.

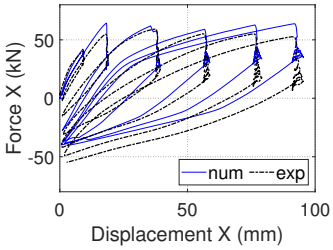

(a) Force-displacement, X direction

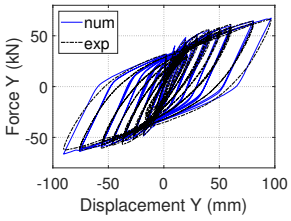

(b) Force-displacement, Y direction

Figure 5.29: Test S2: Numerical vs. experimental results: $H_a = 14GPa$.

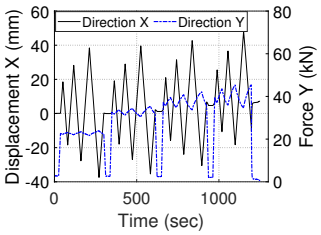

(a) Loading history

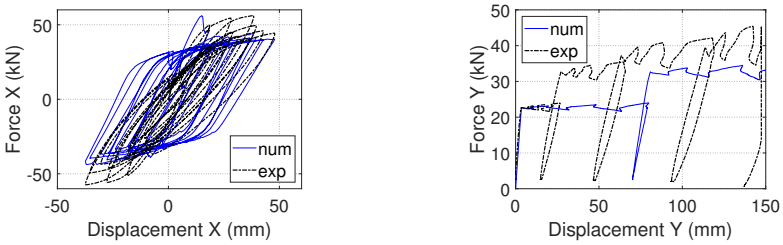

(b) Force-displacement, X direction (c) Force-displacement, Y direction

Figure 5.30: Test S3: Numerical vs. experimental results: $H_a = 2.3GPa$.

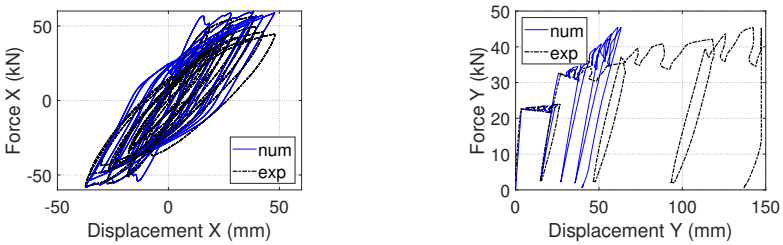

(a) Force-displacement, X direction (b) Force-displacement, Y direction

Figure 5.31: Test S3: Numerical vs. experimental results: $H_a = 20GPa$.

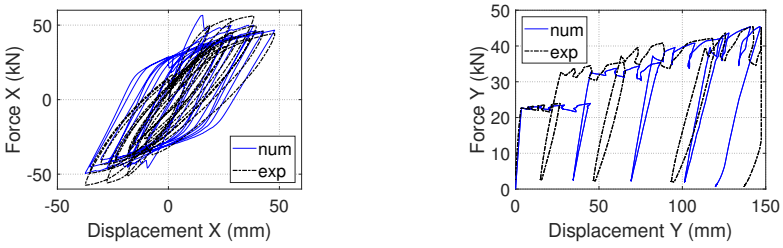

(a) Force-displacement, X direction (b) Force-displacement, Y direction

Figure 5.32: Test S3: Numerical vs. experimental results: $H_a = 7GPa$.

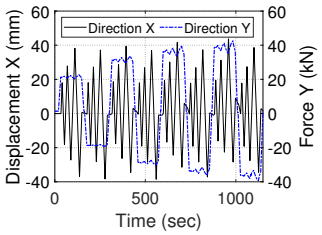

(a) Loading history

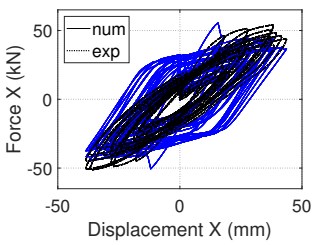

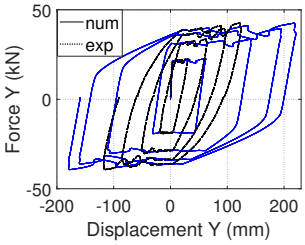

(b) Force-displacement, X direction (c) Force-displacement, Y direction

Figure 5.33: Test S4: Numerical vs. experimental results: $H_a = 2.3GPa$.

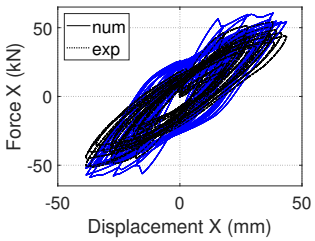

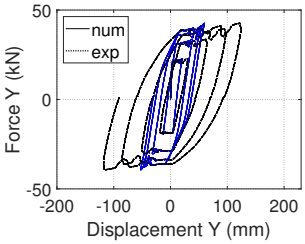

(a) Force-displacement, X direction (b) Force-displacement, Y direction

Figure 5.34: Test S4: Numerical vs. experimental results: $H_a = 20GPa$.

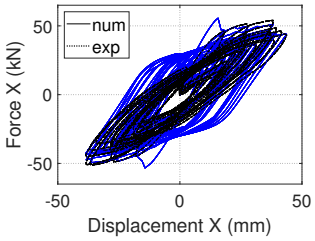

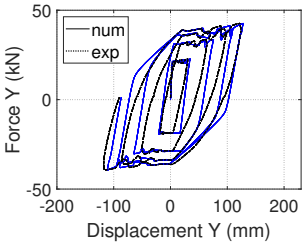

(a) Force-displacement, X direction (b) Force-displacement, Y direction

Figure 5.35: Test S4: Numerical vs. experimental results: $H_a = 7GPa$.

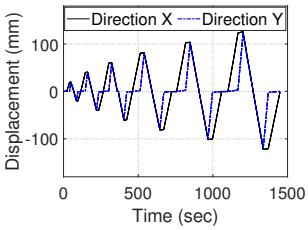

(a) Loading history

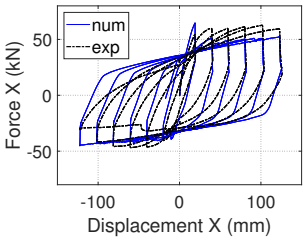

(b) Force-displacement, X direction

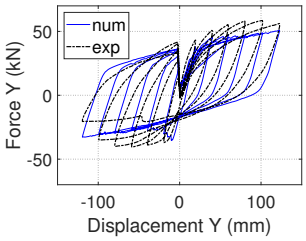

(c) Force-displacement, Y direction

Figure 5.36: Test S5: Numerical vs. experimental results: $H_a = 2.3GPa$.

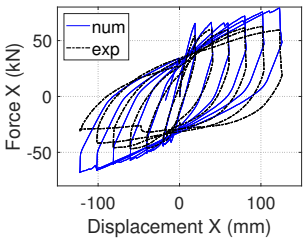

(a) Force-displacement, X direction

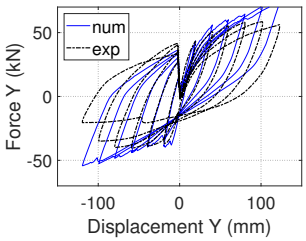

(b) Force-displacement, Y direction

Figure 5.37: Test S5: Numerical vs. experimental results: $H_a = 20GPa$.

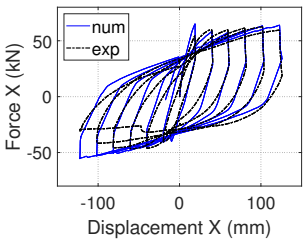

(a) Force-displacement, X direction

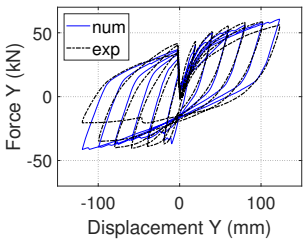

(b) Force-displacement, Y direction

Figure 5.38: Test S5: Numerical vs. experimental results: $H_a = 8GPa$.

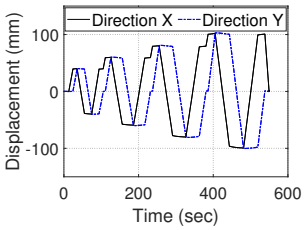

(a) Loading history

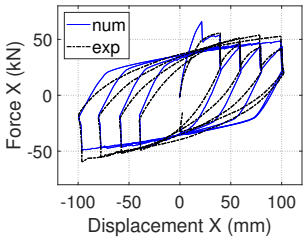

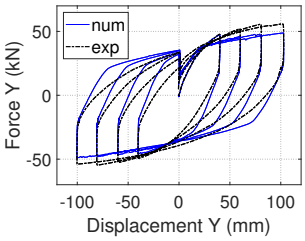

(b) Force-displacement, X direction (c) Force-displacement, Y direction

Figure 5.39: Test S7: Numerical vs. experimental results: $H_a = 2.3GPa$.

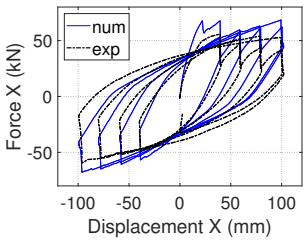

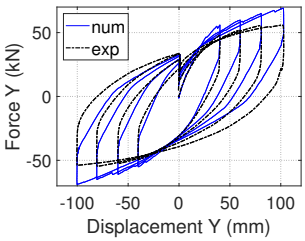

(a) Force-displacement, X direction (b) Force-displacement, Y direction

Figure 5.40: Test S7: Numerical vs. experimental results: $H_a = 20GPa$.

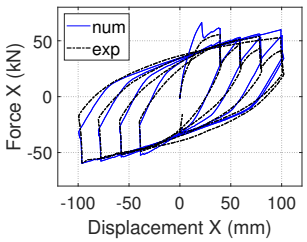

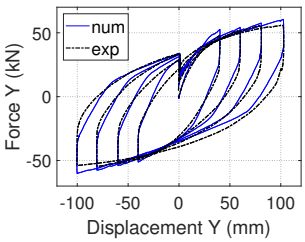

(a) Force-displacement, X direction (b) Force-displacement, Y direction

Figure 5.41: Test S7: Numerical vs. experimental results: $H_a = 10GPa$.

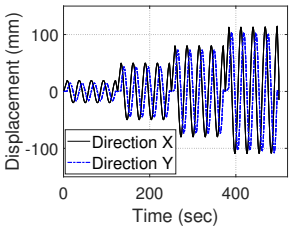

(a) Loading history

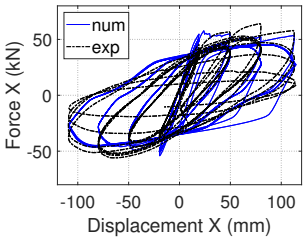

(b) Force-displacement, X direction

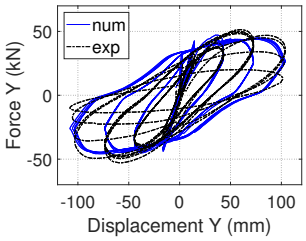

(c) Force-displacement, Y direction

Figure 5.42: Test S9: Numerical vs. experimental results: $H_a = 2.3GPa$.

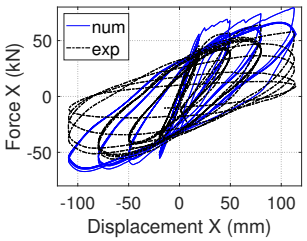

(a) Force-displacement, X direction

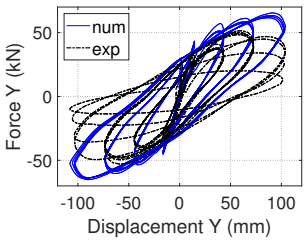

(b) Force-displacement, Y direction

Figure 5.43: Test S9: Numerical vs. experimental results: $H_a = 20GPa$.

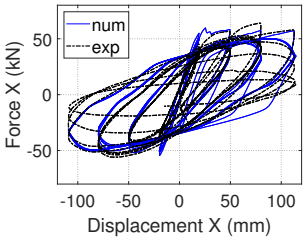

(a) Force-displacement, X direction

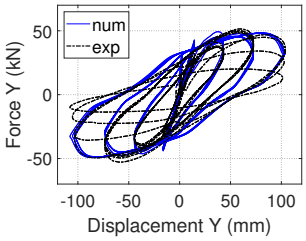

(b) Force-displacement, Y direction

Figure 5.44: Test S9: Numerical vs. experimental results: $H_a = 5GPa$.

B. M1, M2 and M4 sections

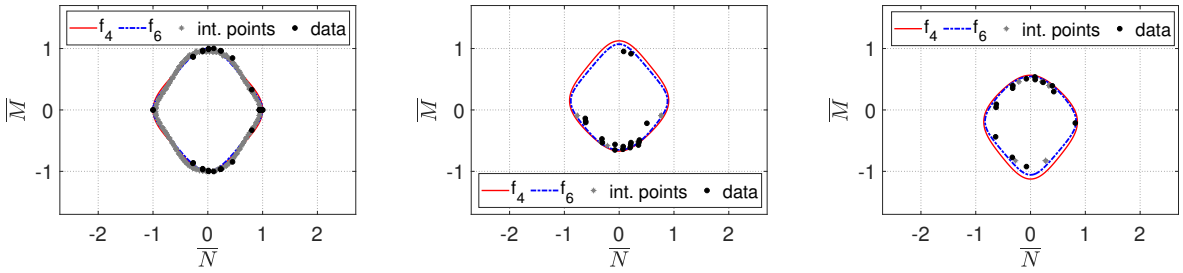

(a) $\bar{V}$=0 (b) $\bar{V}$=0.4 (c) $\bar{V}$=-0.5

Figure 5.45: M1 section: Moment - axial force interaction diagrams obtained by polynomials f_4, f_6 compared to data by numerical simulations and interpolated points.

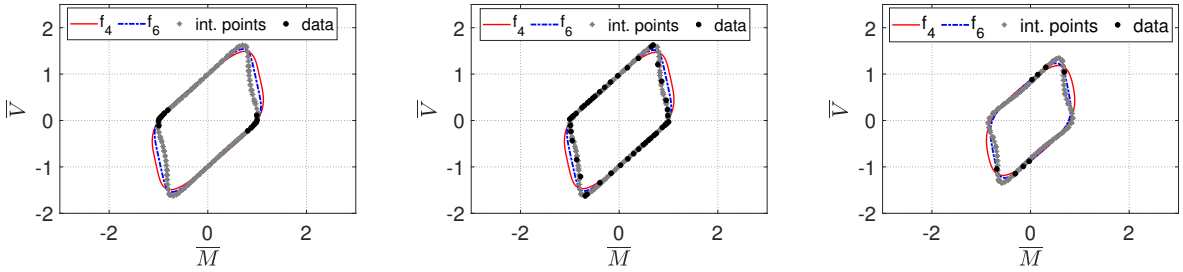

(a) $\bar{N}$=0 (b) $\bar{N}$=0.1 (c) $\bar{N}$=-0.4

Figure 5.46: M1 section: Moment - shear force interaction diagrams obtained by polynomials f_4, f_6 compared to data by numerical simulations and interpolated points.

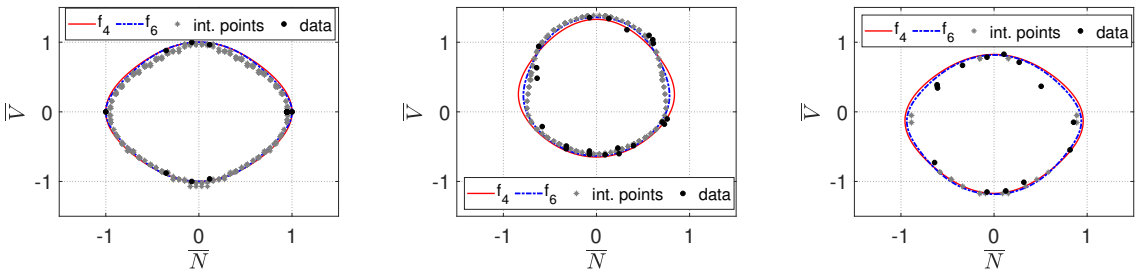

(a) $\bar{M}$=0 (b) $\bar{M}$=0.4 (c) $\bar{M}$=-0.2

Figure 5.47: M1 section: Axial force - shear force interaction diagrams obtained by polynomials f_4, f_6 compared to data by numerical simulations and interpolated points.

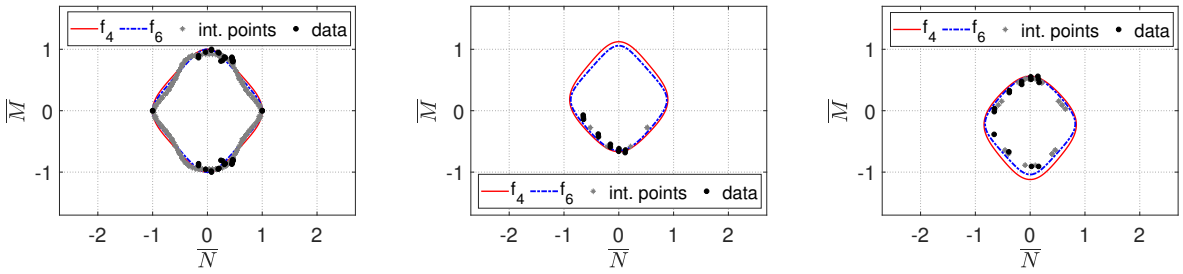

(a) $\bar{V}$=0 (b) $\bar{V}$=0.4 (c) $\bar{V}$=-0.5

Figure 5.48: M2 section: Moment - axial force interaction diagrams obtained by polynomials f_4, f_6 compared to data by numerical simulations and interpolated points.

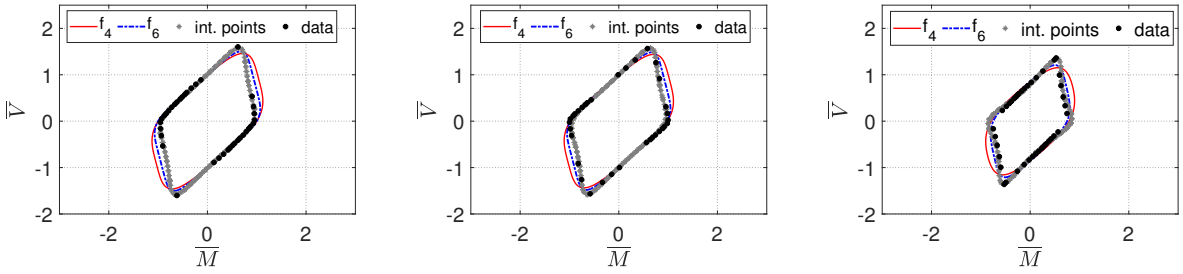

(a) $\bar{N}$=0 (b) $\bar{N}$=0.1 (c) $\bar{N}$=-0.4

Figure 5.49: M2 section: Moment - shear force interaction diagrams obtained by polynomials f_4, f_6 compared to data by numerical simulations and interpolated points.

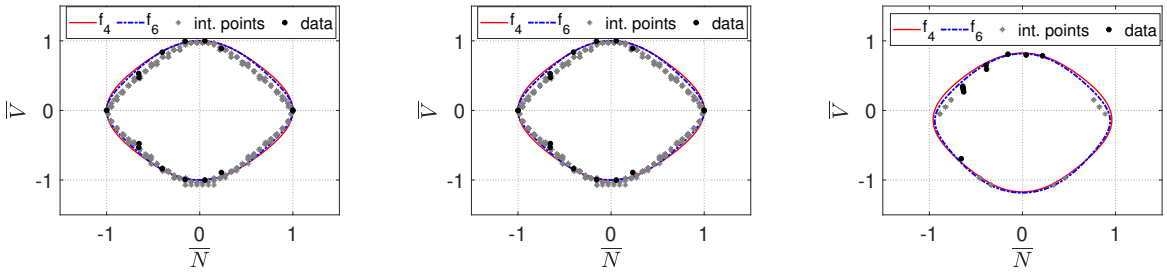

(a) $\bar{M}$=0 (b) $\bar{M}$=0.4 (c) $\bar{M}$=-0.2

Figure 5.50: M2 section: Axial force - shear force interaction diagrams obtained by polynomials f_4, f_6 compared to data by numerical simulations and interpolated points.

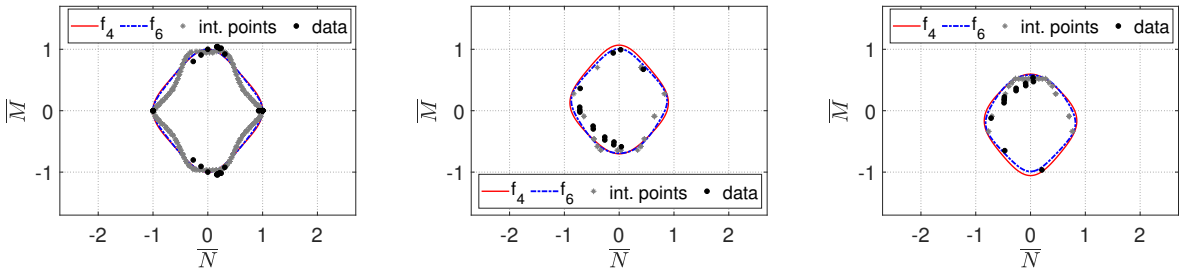

(a) $\bar{V}$=0 (b) $\bar{V}$=0.4 (c) $\bar{V}$=-0.5

Figure 5.51: M4 section: Moment - axial force interaction diagrams obtained by polynomials f_4, f_6 compared to data by numerical simulations and interpolated points.

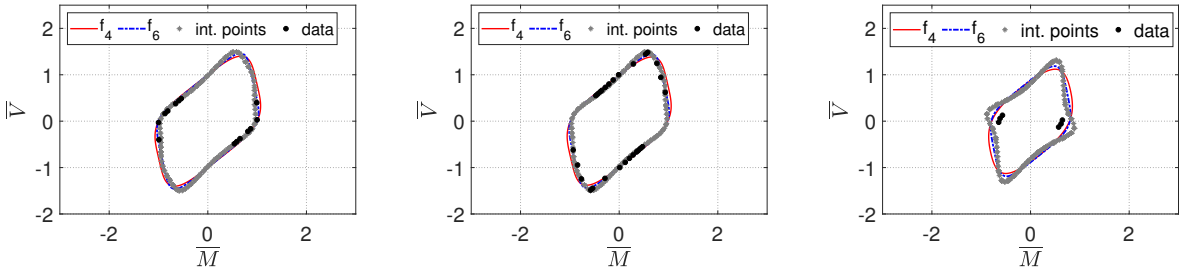

(a) $\bar{N}$=0 (b) $\bar{N}$=0.1 (c) $\bar{N}$-=0.4

Figure 5.52: M4 section: Moment - shear force interaction diagrams obtained by polynomials f_4, f_6 compared to data by numerical simulations and interpolated points.

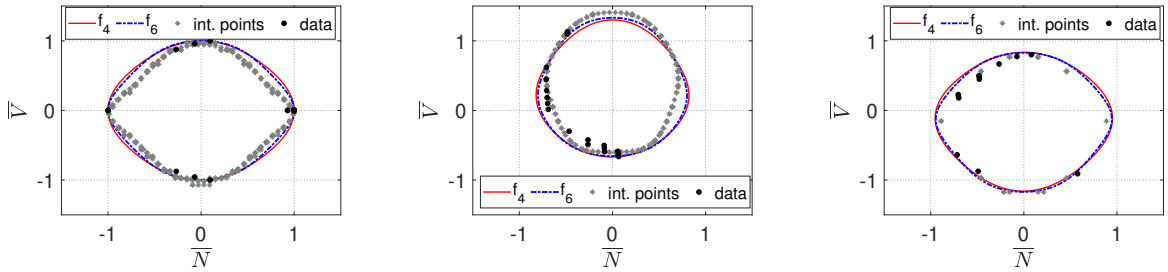

(a) $\bar{M}$=0 (b) $\bar{M}$=0.4 (c) $\bar{M}$=-0.2

Figure 5.53: M4 section: Axial force - shear force interaction diagrams obtained by polynomials f_4, f_6 compared to data by numerical simulations and interpolated points.

BIBLIOGRAPHY

Armero, F. and D. Ehrlich (2004). "An analysis of strain localization and wave propagation in plastic models of beams at failure". In: *Computer Methods in Applied Mechanics and Engineering* 193.30-32, pp. 3129–3171 (cit. on p. 109).

Armero, F. and D. Ehrlich (2006). "Numerical modeling of softening hinges in thin Euler–Bernoulli beams". In: *Computers & Structures* 84.10-11, pp. 641–656 (cit. on p. 109).

Balmer, G. G. (1949). "Shearing strength of concrete under high triaxial stress-computation of Mohr's envelope as a curve". In: *Structural Research Laboratory Report, United States Department of the Interior, Bureau of Reclamation*, No–SP (cit. on p. 16).

Barenblatt, G. I. (1959). "The formation of equilibrium cracks during brittle fracture. General ideas and hypotheses. Axially-symmetric cracks". In: *Journal of applied mathematics and mechanics* 23.3, pp. 622–636 (cit. on p. 38).

Barenblatt, G. I. (1962). "The mathematical theory of equilibrium cracks in brittle fracture". In: *Advances in applied mechanics* 7, pp. 55–129 (cit. on pp. 36, 38).

Barnichon, J.-D. (1998). "Finite element modelling in structural and petroleum geology". PhD thesis. Université de Liège (cit. on p. 106).

Bathe, K.-J. (2006). *Finite element procedures*. Klaus-Jurgen Bathe (cit. on p. 30).

Bauschinger, J. (1879). *Ueber die Quercontraction und-Dilatation bei der Längenausdehnung und-Zusammendrückung prismatischer Körper* (cit. on p. 20).

Bažant, Z. P. and T. B. Belytschko (1985). "Wave propagation in a strain-softening bar: exact solution". In: *Journal of Engineering Mechanics* 111.3, pp. 381–389 (cit. on p. 32).

Bažant, Z. P. and F.-B. Lin (1988a). "Non-local yield limit degradation". In: *International Journal for Numerical Methods in Engineering* 26.8, pp. 1805–1823 (cit. on p. 34).

Bažant, Z. P. and F.-B. Lin (1988b). "Nonlocal smeared cracking model for concrete fracture". In: *Journal of structural Engineering* 114.11, pp. 2493–2510 (cit. on p. 34).

Bažant, Z. P. and B. H. Oh (1983). "Crack band theory for fracture of concrete". In: *Matériaux et construction* 16.3, pp. 155–177 (cit. on pp. 34, 47).

Bažant, Z. P. and J. Ožbolt (1990). "Nonlocal microplane model for fracture, damage, and size effect in structures". In: *Journal of Engineering Mechanics* 116.11, pp. 2485–2505 (cit. on p. 34).

Bažant, Z. P. and G. Pijaudier-Cabot (1989). "Measurement of characteristic length of nonlocal continuum". In: *Journal of Engineering Mechanics* 115.4, pp. 755–767 (cit. on p. 34).

Belytschko, T., J. Fish, and B. E. Engelmann (1988). "A finite element with embedded localization zones". In: *Computer methods in applied mechanics and engineering* 70.1, pp. 59–89 (cit. on p. 36).

Benouniche, S. (1979). "Modélisation de l'endommagement du béton par microfissuration en compression". PhD thesis. Thèse, Université de Paris VI (cit. on p. 14).

Bischoff, P. H. and S. Perry (1991). "Compressive behaviour of concrete at high strain rates". In: *Materials and structures* 24.6, pp. 425–450 (cit. on pp. 18, 25).

Bischoff, P. H. and S. H. Perry (1995). "Impact behavior of plain concrete loaded in uniaxial compression". In: *Journal of engineering mechanics* 121.6, pp. 685–693 (cit. on p. 17).

Bitar, I., N. Benkemoun, P. Kotronis, and S. Grange (2019). "A multifiber Timoshenko beam with embedded discontinuities". In: *Engineering Fracture Mechanics* 214, pp. 339–364 (cit. on pp. 31, 111).

Bitar, I., S. Grange, P. Kotronis, and N. Benkemoun (2018a). "A comparison of displacement-based Timoshenko multi-fiber beams finite element formulations and elasto-plastic applications". In: *European Journal of Environmental and Civil Engineering* 22.4, pp. 464–490 (cit. on p. 90).

Bitar, I., P. Kotronis, N. Benkemoun, and S. Grange (2018b). "A generalized Timoshenko beam with embedded rotation discontinuity". In: *Finite Elements in Analysis and Design* 150, pp. 34–50 (cit. on pp. 31, 111, 122, 138).

Borja, R. I. (2013). *Plasticity*. Vol. 2. Springer (cit. on p. 20).

Bousias, S. N., G. Verzeletti, M. N. Fardis, and E. Gutierrez (1995). "Load-path effects in column biaxial bending with axial force". In: *Journal of Engineering Mechanics* 121.5, pp. 596–605 (cit. on pp. 48, 55, 57, 125, 127).

Bresler, B. and K. S. Pister (1958). "Strength of concrete under combined stresses". In: *Journal Proceedings*. Vol. 55. 9, pp. 321–345 (cit. on p. 14).

Bui, N., M. Ngo, M. Nikolic, D. Brancherie, and A. Ibrahimbegovic (2014). "Enriched Timoshenko beam finite element for modeling bending and shear failure of reinforced

concrete frames". In: *Computers & Structures* 143, pp. 9–18 (cit. on pp. 31, 110, 115, 138).

Cadoni, E. and D. Forni (2015). "Strain rate effects on reinforcing steels in tension". In: *EPJ Web of Conferences*. Vol. 94. EDP Sciences, p. 01004 (cit. on p. 21).

Caillerie, D., P. Kotronis, and R. Cybulski (2015). "A Timoshenko finite element straight beam with internal degrees of freedom". In: *International Journal for Numerical and Analytical Methods in Geomechanics* 39.16, pp. 1753–1773 (cit. on pp. 90, 111).

Caliò, I., M. Marletta, and B. Pantò (2012). "A new discrete element model for the evaluation of the seismic behaviour of unreinforced masonry buildings". In: *Engineering Structures* 40, pp. 327–338 (cit. on p. 85).

Camacho, G. and M. Ortiz (1996). "Computational modeling of impact damage in brittle materials". In: *International Journal of Solids and Structures* 33, pp. 2899–2938 (cit. on p. 39).

Camanho, P. P., C. G. Davila, and M. De Moura (2003). "Numerical simulation of mixed-mode progressive delamination in composite materials". In: *Journal of composite materials* 37.16, pp. 1415–1438 (cit. on p. 37).

Carpinteri, A., M. Corrado, G. Goso, and M. Paggi (2012). "Size-scale effects on interaction diagrams for reinforced concrete columns". In: *Construction and Building Materials* 27.1, pp. 271–279 (cit. on p. 27).

Cast3M (2019). *Description of the finite element code Cast3M.* `http://www-cast3m.cea.fr` (cit. on pp. 31, 41, 90).

CEN (2004). "Eurocode 2: Design of concrete structures: Part 1-1: General rules and rules for buildings, EN 1992-1-1." In: *Brussels: European Committee for Standardization* (cit. on pp. 26, 60, 97, 108).

Chambon, R., D. Caillerie, and T. Matsuchima (2001). "Plastic continuum with microstructure, local second gradient theories for geomaterials: localization studies". In: *International journal of solids and structures* 38.46-47, pp. 8503–8527 (cit. on p. 35).

Charlier, R. (1987). "Approche unifiée de quelques probèmes non linéaires de mécanique des milieux continus par la méthode des éléments finis." PhD thesis. Université de Liège (cit. on p. 106).

Chatzigogos, C., A. Pecker, and J. Salencon (2009). "Macroelement modeling of shallow foundations". In: *Soil Dynamics and Earthquake Engineering* 29.5, pp. 765–781 (cit. on p. 83).

Chen, L., W. Wen, and H. Cui (2012). "Yielding description for a Ni3Al based intermetallic alloy". In: *Materials & Design* 41, pp. 192–197 (cit. on p. 19).

Chen, W.-F. (2007). *Plasticity in reinforced concrete*. J. Ross Publishing (cit. on pp. 13, 14, 16).

Collin, F. (2003). "Couplages thermo-hydro-mécaniques dans les sols et les roches tendres partiellement saturés". PhD thesis. Université de Liège (cit. on p. 106).

Corn, S. (1998). "Simplification de modèles éléments finis de structures à comportement dynamique de poutre". PhD thesis. UFR des sciences et techniques de l'université Franche-Comté (cit. on p. 91).

Cosserat, E. (1909). *Théorie des corps déformables*. Librairie Scientifique A. Hermann et Fils (cit. on p. 35).

Cremer, C., A. Pecker, and L. Davenne (2000). "Elaboration of a SSI Macro-Element with Uplift of Shallow Foundation". In: *Implications Of Recent Earthquakes On Seismic Risk*. World Scientific, pp. 127–138 (cit. on p. 83).

Cremer, C., A. Pecker, and L. Davenne (2001). "Cyclic macro-element for soil–structure interaction: material and geometrical non-linearities". In: *International Journal for Numerical and Analytical Methods in Geomechanics* 25.13, pp. 1257–1284 (cit. on p. 92).

Dafalias, Y. F. (1986). "Bounding surface plasticity. I: Mathematical foundation and hypoplasticity". In: *Journal of engineering mechanics* 112.9, pp. 966–987 (cit. on p. 151).

Dafalias, Y. F. and L. R. Herrmann (1986). "Bounding surface plasticity. II: Application to isotropic cohesive soils". In: *Journal of Engineering Mechanics* 112.12, pp. 1263–1291 (cit. on p. 151).

El-Dakhakhni, W., W. Mekky, and S. Changiz-Rezaei (2009). "Vulnerability screening and capacity assessment of reinforced concrete columns subjected to blast". In: *Journal of performance of constructed facilities* 23.5, pp. 353–365 (cit. on p. 152).

Daudeville, L. and Y. Malécot (2011). "Concrete structures under impact". In: *European Journal of Environmental and Civil Engineering* 15.sup1, pp. 101–140 (cit. on p. 17).

Davenne, L. and C. Brenet (1998). *Macro-éléments de poutres en béton armé*. Tech. rep. Rapport interne LMT - Cachan, num. 210, juin (cit. on p. 84).

Davis, E. (1945). "Yielding and fracture of medium-carbon steel under combined stress". In: (cit. on p. 18).

Desprez, C., J. Mazars, P. Kotronis, and P. Paultre (2013). "Damage model for FRP-confined concrete columns under cyclic loading". In: *Engineering Structures* 48, pp. 519–531 (cit. on p. 31).

Desprez, C., P. Kotronis, and J. Mazars (2015). "Seismic vulnerability assessment of a RC structure before and after FRP retrofitting". In: *Bulletin of Earthquake Engineering* 13.2, pp. 539–564 (cit. on p. 31).

Donea, J. and L. G. Lamain (1987). "A modified representation of transverse shear in C0 quadrilateral plate elements". In: *Computer Methods in Applied Mechanics and Engineering* 63.2, pp. 183–207 (cit. on p. 90).

Doulgeroglou, A.-A., P. Kotronis, G. Sciarra, and C. Bouillon (2022). "3D interaction diagrams for symmetrically reinforced concrete square sections with various reinforcement ratios". In: *Engineering Structures* 262, p. 114272 (cit. on p. 81).

Dugdale, D. S. (1960). "Yielding of steel sheets containing slits". In: *Journal of the Mechanics and Physics of Solids* 8.2, pp. 100–104 (cit. on pp. 36, 38).

Dvorkin, E. N., A. M. Cuitiño, and G. Gioia (1990). "Finite elements with displacement interpolated embedded localization lines insensitive to mesh size and distortions". In: *International journal for numerical methods in engineering* 30.3, pp. 541–564 (cit. on p. 33).

Ehrlich, D. and F. Armero (2005). "Finite element methods for the analysis of softening plastic hinges in beams and frames". In: *Computational Mechanics* 35.4, pp. 237–264 (cit. on pp. 109, 111, 114, 122).

Elachachi, S. M. (1992). "Sur l'elaboration d'une methode simplifiee d'analyse des structures de genie civil par macro-elements adaptes aux constructions composites et endommageables". PhD thesis. Paris 6 (cit. on pp. 27, 84).

Faccioli, E., M. Vanini, and R. Paolucci (1999). *TRISEE: 3D site effects and soil-foundation interaction in earthquake and vibration risk evaluation*. European commission. Directorate-general 12. Science, research and development (cit. on p. 61).

Faria, R. (1994). "Avaliação do comportamento sísmico de barragens de betão através de um modelo de dano contínuo". PhD thesis. Faculdade de Engenharia da Universidade do Porto (cit. on pp. 44, 52).

Faria, R., J. Oliver, and M. Cervera (1998). "A strain-based plastic viscous-damage model for massive concrete structures". In: *International journal of solids and structures* 35.14, pp. 1533–1558 (cit. on pp. 42, 44, 45, 51).

Fléjou, J.-L. (2018). “Relations de comportement non linéaires 1D, Technical Report”. In: *Code Aster, EDF R & D* (cit. on pp. 103, 108).

Föppl, A. (1899). “Reports from the Laboratory for Engineering Mechanics (Mitteilungen aus dem Mechanisch Technischen Laboratorium der Technischen Hochschule München)”. In: *Technische Hochschule München* 27, pp. 1–30 (cit. on p. 14).

Germain, P. (1973). “The method of virtual power in continuum mechanics. Part 2: Microstructure”. In: *SIAM Journal on Applied Mathematics* 25.3, pp. 556–575 (cit. on p. 33).

Geubelle, P. H. and J. S. Baylor (1998). “Impact-induced delamination of composites: a 2D simulation”. In: *Composites Part B: Engineering* 29.5, pp. 589–602 (cit. on p. 39).

Gopalaratnam, V., W. Gerstle, J. Isenberg, and S. Mindess (1996). “State-of-the-art report on dynamic fracture”. In: *ACI Committee* 446 (cit. on p. 17).

Grange, S., P. Kotronis, and J. Mazars (2008). “A macro-element for a circular foundation to simulate 3D soil–structure interaction”. In: *International Journal for Numerical and Analytical Methods in Geomechanics* 32.10, pp. 1205–1227 (cit. on pp. 61, 92).

Grange, S. (2008). “Modélisation simplifiée 3D de l’interaction sol-structure: application au génie parasismique.” PhD thesis. Institut National Polytechnique de Grenoble-INPG (cit. on p. 83).

Grange, S., L. Botrugno, P. Kotronis, and C. Tamagnini (2011). “The effects of soil–structure interaction on a reinforced concrete viaduct”. In: *Earthquake Engineering & Structural Dynamics* 40.1, pp. 93–105 (cit. on p. 31).

Grange, S., P. Kotronis, and J. Mazars (2009a). “A macro-element to simulate 3D soil–structure interaction considering plasticity and uplift”. In: *International Journal of Solids and Structures* 46.20, pp. 3651–3663 (cit. on p. 83).

Grange, S., P. Kotronis, and J. Mazars (2009b). “Numerical modelling of the seismic behaviour of a 7-story building: NEES benchmark”. In: *Materials and structures* 42.10, pp. 1433–1442 (cit. on p. 31).

Green, S. and S. Swanson (1973). *Static constitutive relations for concrete*. Tech. rep. TERRA TEK INC SALT LAKE CITY UT (cit. on p. 45).

Gregori, J. N., P. M. Sosa, M. F. Prada, and F. C. Filippou (2007). “A 3D numerical model for reinforced and prestressed concrete elements subjected to combined axial, bending, shear and torsion loading”. In: *Engineering Structures* 29.12, pp. 3404–3419 (cit. on p. 28).

Guedes, J., P. Pegon, and A. V. Pinto (1994). "A Fibre/Timoshenko beam element in Castem 2000". In: *Special publication Nr. I.94.31, Applied Mechanics Unit, Institute for Safety Technology, Joint Research Centre, Commission of the European Communities, I-21020 ISPRA (VA), Italy* (cit. on pp. 31, 87–89).

Gutierrez, E., G. Magonette, and G. Verzeletti (1993). "Experimental studies of loading rate effects on reinforced concrete columns". In: *Journal of Engineering Mechanics* 119.5, pp. 887–904 (cit. on pp. 48, 49, 126).

Haselton, C. B. (2006). "Assessing seismic collapse safety of modern reinforced concrete moment frame buildings". PhD thesis. Stanford University (cit. on p. 120).

Hemsas, M., S. M. Elachachi, and D. Breysse (2009). "Modélisation par macroéléments du comportement non linéaire des voiles en béton armé". In: *European Journal of Environmental and Civil Engineering* 13.5, pp. 615–640 (cit. on p. 85).

Heo, Y., G. W. Zhang, S. K. Kunnath, and Y. Xiao (2009). "Modeling cyclic behavior of reinforcing steel: Relevance in seismic response analysis of reinforced concrete structures". In: *Key Engineering Materials*. Vol. 400. Trans Tech Publ, pp. 301–309 (cit. on p. 21).

Hillerborg, A., M. Modéer, and P.-E. Petersson (1976). "Analysis of crack formation and crack growth in concrete by means of fracture mechanics and finite elements". In: *Cement and Concrete Research* 6.6, pp. 773–781 (cit. on pp. 34, 43, 47).

Hsu, T. T., F. O. Slate, G. M. Sturman, and G. Winter (1963). "Microcracking of plain concrete and the shape of the stress-strain curve". In: *Journal Proceedings*. Vol. 60. 2, pp. 209–224 (cit. on p. 14).

Hughes, B. and G. Chapman (1966). "The complete stress-strain curve for concrete in direct tension". In: *Matls & Structures, Res & Testing/Fr/* (cit. on p. 14).

Huguet, M., S. Erlicher, P. Kotronis, and F. Voldoire (2017). "Stress resultant nonlinear constitutive model for cracked reinforced concrete panels". In: *Engineering Fracture Mechanics* 176, pp. 375–405 (cit. on p. 150).

Imran, I. and S. J. Pantazopoulou (1996). "Experimental study of plain concrete under triaxial stress". In: *ACI Materials Journal-American Concrete Institute* 93.6, pp. 589–601 (cit. on p. 16).

Jin, Z., Z.-Y. Yin, P. Kotronis, Z. Li, and C. Tamagnini (2019). "A hypoplastic macroelement model for a caisson foundation in sand under monotonic and cyclic loadings". In: *Marine Structures* 66, pp. 16–26 (cit. on p. 83).

Jirasek, M. (1998). “Nonlocal models for damage and fracture: comparison of approaches”. In: *International Journal of Solids and Structures* 35.31-32, pp. 4133–4145 (cit. on p. 34).

Jirásek, M. and T. Zimmermann (1997). “Rotating crack model with transition to scalar damage: I. Local formulation, II. Nonlocal formulation and adaptivity”. In: *LSC Internal Rep. No. 97* 1 (cit. on p. 34).

Jirásek, M. (2002). “Objective modeling of strain localization”. In: *Revue française de génie civil* 6.6, pp. 1119–1132 (cit. on p. 36).

Jirásek, M. and M. Bauer (2012). “Numerical aspects of the crack band approach”. In: *Computers & structures* 110, pp. 60–78 (cit. on p. 47).

Jukić, M., B. Brank, and A. Ibrahimbegovic (2014). “Failure analysis of reinforced concrete frames by beam finite element that combines damage, plasticity and embedded discontinuity”. In: *Engineering structures* 75, pp. 507–527 (cit. on pp. 109, 138).

Jukić, M., B. Brank, and A. Ibrahimbegović (2013). “Embedded discontinuity finite element formulation for failure analysis of planar reinforced concrete beams and frames”. In: *Engineering Structures* 50, pp. 115–125 (cit. on pp. 31, 109).

Jukiić, M. (2013). “Finite elements for modeling of localized failure in reinforced concrete”. PhD thesis. École normale supérieure de Cachan-ENS Cachan; Univerza v Ljubljani. Fakulteta za gradbeništvo in geodezijo (cit. on p. 109).

Kœchlin, P. (2007). “Modèle de comportement membrane-flexion et critère de perforation pour l’analyse de structures minces en béton armé sous choc mou”. In: *These de doctorat, Ecole Polytechnique* (cit. on p. 26).

Koechlin, P., S. Andrieux, A. Millard, and S. Potapov (2008). “Failure criterion for reinforced concrete beams and plates subjected to membrane force, bending and shear”. In: *European Journal of Mechanics-A/Solids* 27.6, pp. 1161–1183 (cit. on p. 26).

Kotronis, P. and J. Mazars (2005). “Simplified modelling strategies to simulate the dynamic behaviour of R/C walls”. In: *Journal of earthquake engineering* 9.02, pp. 285–306 (cit. on p. 31).

Kotsovos, M. D. and J. B. Newman (1977). “Behavior of concrete under multiaxial stress”. In: *Journal Proceedings*. Vol. 74. 9, pp. 443–446 (cit. on pp. 14, 16).

Kunnath, S. K., Y. Heo, and J. F. Mohle (2009). “Nonlinear uniaxial material model for reinforcing steel bars”. In: *Journal of Structural Engineering* 135.4, pp. 335–343 (cit. on p. 20).

Kupfer, H., H. K. Hilsdorf, and H. Rusch (1969). “Behavior of concrete under biaxial stresses”. In: *ACI Structural Journal* 66.8, pp. 656–666 (cit. on pp. 43, 44, 46).

Kupfer, H. B. and K. H. Gerstle (1973). “Behavior of concrete under biaxial stresses”. In: *Journal of the engineering mechanics division* 99.4, pp. 853–866 (cit. on pp. 14, 15).

Lebon, G. (2011). “Analyse de l’endommagement des structures de génie civil: techniques de sous-structuration hybride couplées à un modèle d’endommagement anisotrope”. PhD thesis. École normale supérieure de Cachan-ENS Cachan (cit. on pp. 143, 145).

Lessells, J. and C. MacGregor (1940). “Combined stress experiments on a nickel-chrome-molybdenum steel”. In: *Journal of the Franklin Institute* 230.2, pp. 163–181 (cit. on p. 18).

Li, Q. and F. Ansari (1999). “Mechanics of damage and constitutive relationships for high-strength concrete in triaxial compression”. In: *Journal of engineering mechanics* 125.1, pp. 1–10 (cit. on p. 16).

Li, Z., P. Kotronis, and S. Escoffier (2014). “Numerical study of the 3D failure envelope of a single pile in sand”. In: *Computers and Geotechnics* 62, pp. 11–26 (cit. on p. 83).

Li, Z., P. Kotronis, S. Escoffier, and C. Tamagnini (2016). “A hypoplastic macroelement for single vertical piles in sand subject to three-dimensional loading conditions”. In: *Acta Geotechnica* 11.2, pp. 373–390 (cit. on p. 83).

Li, Z., P. Kotronis, S. Escoffier, and C. Tamagnini (2018). “A hypoplastic macroelement formulation for single batter piles in sand”. In: *International Journal for Numerical and Analytical Methods in Geomechanics* 42.12, pp. 1346–1365 (cit. on p. 83).

Liger (2016). *Liger Supercomputer*. `https://supercomputing.ec-nantes.fr/liger` (cit. on p. 81).

Llau, A. (2016). “Méthodes de simulation du comportement mécanique non linéaire des grandes structures en béton armé et précontraint: condensation adaptative en contexte aléatoire et représentation des hétérogénéités”. PhD thesis. Université Grenoble Alpes (ComUE) (cit. on p. 51).

Lofberg, J. (2004). “YALMIP: A toolbox for modeling and optimization in MATLAB”. In: *2004 IEEE international conference on robotics and automation (IEEE Cat. No. 04CH37508)*. IEEE, pp. 284–289 (cit. on p. 68).

Mai, V.-C., T.-C. Nguyen, and C.-B. Dao (2020). “Numerical simulation of ultra-high-performance fiber-reinforced concrete frame structure under fire action”. In: *Asian Journal of Civil Engineering* 21.5, pp. 797–804 (cit. on p. 29).

Malvar, L. J., C. A. Ross, et al. (1998). “Review of strain rate effects for concrete in tension”. In: *ACI Materials Journal* 95, pp. 735–739 (cit. on p. 19).

Marin, J. and L. Hu (1956). “Biaxial plastic stress-strain relations of a mild steel for variable stress ratios”. In: *Transactions of the American Society of Mechanical Engineers* 78.3, pp. 499–508 (cit. on p. 18).

Matallah, M. and C. La Borderie (2009). “Inelasticity–damage-based model for numerical modeling of concrete cracking”. In: *Engineering Fracture Mechanics* 76.8, pp. 1087–1108 (cit. on p. 119).

Maxey, W. (1986). “Y/T significance in line pipe”. In: *Proceedings of the 7th Symposium on Line Pipe Research, Houston, Texas*, pp. 91–918 (cit. on p. 18).

Mazars, J. (1984). “Application de la mécanique de l’endommagement au comportement non linéaire et à la rupture du béton de structure”. In: *THESE DE DOCTEUR ES SCIENCES PRESENTEE A L’UNIVERSITE PIERRE ET MARIE CURIE-PARIS 6* (cit. on p. 42).

Mazars, J., P. Kotronis, F. Ragueneau, and G. Casaux (2006). “Using multifiber beams to account for shear and torsion: Applications to concrete structural elements”. In: *Computer Methods in Applied Mechanics and Engineering* 195.52, pp. 7264–7281 (cit. on p. 31).

McHenry, D. and J. Karni (1958). “Strength of concrete under combined tensile and compressive stress”. In: *Journal Proceedings*. Vol. 54. 4, pp. 829–839 (cit. on p. 14).

Melo, J., S. Afshan, T. Rossetto, and H. Varum (2019). “Experimental investigation of cyclic response of stainless steel reinforced concrete columns”. In: *SECED 2019 Conference on Earthquake and Civil Engineering Dynamics* (cit. on p. 132).

Menegotto, M. and P. Pinto (1973). “Method of analysis for cyclically loaded reinforced concrete plane frames including changes in geometry and non-elastic of elements under combined normal force and bending”. In: *Proceedings, IABSE symposium* (cit. on pp. 20, 102, 130).

Needleman, A. (1990a). “An analysis of decohesion along an imperfect interface”. In: *Non-linear fracture*. Springer, pp. 21–40 (cit. on p. 38).

Needleman, A. (1990b). “An analysis of tensile decohesion along an interface”. In: *Journal of the Mechanics and Physics of Solids* 38.3, pp. 289–324 (cit. on p. 38).

Needleman, A. (1987). “A continuum model for void nucleation by inclusion debonding”. In: (cit. on p. 38).

Nguyen, T.-A. (2019). “Development of an enhanced finite element model for reinforced concrete memebers subjected to combined shear-bending-torsion actions”. PhD thesis. INSA Rennes (cit. on pp. 27, 28).

Nova, R. and L. Montrasio (1991). “Settlements of shallow foundations on sand”. In: *Géotechnique* 41.2, pp. 243–256 (cit. on pp. 83, 87).

Oliver, J. (2000). “On the discrete constitutive models induced by strong discontinuity kinematics and continuum constitutive equations”. In: *International journal of solids and structures* 37.48-50, pp. 7207–7229 (cit. on p. 36).

Ožbolt, J. and Z. P. Bažant (1996). “Numerical smeared fracture analysis: Nonlocal microcrack interaction approach”. In: *International Journal for Numerical Methods in Engineering* 39.4, pp. 635–661 (cit. on p. 34).

Pantò, B., E. Raka, F. Cannizzaro, G. Camata, S. Caddemi, E. Spacone, and I. Caliò (2015). “Numerical macro-modeling of unreinforced masonry structures: a critical appraisal”. In: *Proceedings of the Fifteenth International Conference on Civil, Structural and Environmental Engineering Computing* (cit. on pp. 85, 86).

Park, Y.-J., A. H. Ang, and Y. K. Wen (1987). “Damage-limiting aseismic design of buildings”. In: *Earthquake spectra* 3.1, pp. 1–26 (cit. on p. 120).

Pastor, M. (1991). “Modelling of anisotropic sand behaviour”. In: *Computers and Geotechnics* 11.3, pp. 173–208 (cit. on p. 151).

Pegon, P. (1994). “A Timoshenko simple beam element in Castem 2000, Special publication Nr. I. 94.04. Italy: Applied Mechanics Unit”. In: *Institute for Safety Technology, Joint Research Centre, Commission of the European Communities, I-21020 ISPRA (VA)* (cit. on pp. 87–90).

Petersson, P.-E. (1981). *Crack growth and development of fracture zones in plain concrete and similar materials*. Tech. rep. Lund Inst. of Tech.(Sweden). Div. of Building Materials (cit. on p. 14).

Pham, B., D. Brancherie, L. Davenne, and A. Ibrahimbegovic (2013). “Stress-resultant models for ultimate load design of reinforced concrete frames and multi-scale parameter estimates”. In: *Computational Mechanics* 51.3, pp. 347–360 (cit. on pp. 31, 109, 119, 138).

Pham, B.-H., L. Davenne, D. Brancherie, and A. Ibrahimbegovic (2010). “Stress resultant model for ultimate load design of reinforced-concrete frames: combined axial force and bending moment”. In: *Computers and Concrete* 7.4, pp. 303–315 (cit. on pp. 31, 109, 119, 120, 151).

Pijaudier-Cabot, G. and Z. P. Bažant (1987). “Nonlocal damage theory”. In: *Journal of engineering mechanics* 113.10, pp. 1512–1533 (cit. on pp. 34, 42).

Prevost, J.-H. (1980). “ANISOTROPIC UNDRAINED STRESS-STRAIN BEHAVIOUR OF CLAYS-CLOSURE”. In: *Journal of Geotechnical and Geoenvironmental Engineering* 106.ASCE 13942 (cit. on p. 92).

Rahal, K. N. (2000a). “Shear Strength of Reinforced Concrete: Part 1-Membrane Elements Subjected to Pure Shear”. In: *ACI Structural Journal* 97.1, pp. 86–93 (cit. on p. 27).

Rahal, K. N. (2000b). “Shear strength of reinforced concrete: Part II—Beams subjected to shear, bending moment, and axial load”. In: *Structural Journal* 97.2, pp. 219–224 (cit. on pp. 27, 97, 108).

Raka, E., E. Spacone, V. Sepe, and G. Camata (2015). “Advanced frame element for seismic analysis of masonry structures: model formulation and validation”. In: *Earthquake Engineering & Structural Dynamics* 44.14, pp. 2489–2506 (cit. on p. 85).

Ramtani, S. (1990). “Contribution à la modélisation du comportement multiaxial du béton endommagé avec description du caractère unilatéral”. PhD thesis. Paris 6 (cit. on pp. 14, 17).

Rice, J. R. and J.-S. Wang (1989). “Embrittlement of interfaces by solute segregation”. In: *Materials Science and Engineering: A* 107, pp. 23–40 (cit. on p. 38).

Richard, B. (2010). “Modélisation d’éléments de structure en béton armé dégradés par corrosion: la problématique de l’interface acier/béton en présence de corrosion”. PhD thesis. Université Paris-Est (cit. on p. 60).

Richard, B., F. Ragueneau, C. Cremona, and L. Adelaide (2010). “Isotropic continuum damage mechanics for concrete under cyclic loading: Stiffness recovery, inelastic strains and frictional sliding”. In: *Engineering Fracture Mechanics* 77.8, pp. 1203–1223 (cit. on pp. 35, 42).

Richart, F. E., A. Brandtzæg, and R. L. Brown (1928). *A study of the failure of concrete under combined compressive stresses*. Tech. rep. University of Illinois at Urbana Champaign, College of Engineering ... (cit. on p. 16).

Ros, M. and A. Eichinger (1929). “Versuche zur klaerung der frage der bruchefahr III, mettalle, eidgenoss”. In: *Mat prüf Versuchsanstalt Industriell Bauwerk Geerbe. Diskussionsbericht* 34, pp. 3–59 (cit. on p. 18).

Rossi, P., J. G. Van Mier, F. Toutlemonde, F. Le Maou, and C. Boulay (1994). “Effect of loading rate on the strength of concrete subjected to uniaxial tension”. In: *Materials and structures* 27.5, pp. 260–264 (cit. on p. 17).

Rouquand, A., C. Pontiroli, and J. Mazars (2007). "Concrete structures under severe loading: a strategy to model the response for a large range of dynamic loads". In: *Fracture Mechanics of Concrete and Concrete Structures: Proceedings of FraMCoS* 6 (cit. on p. 17).

Sakai, J. and K. Kawashima (2000). *Effect of varying axial loads including a constant tension on seismic performance of reinforced concrete bridge columns*. Tokyo Institute of Technology (cit. on p. 25).

Salençon, J. (1983). *Calcul à la rupture et analyse limite*. Presses de l'Ecole Nationale des Ponts et Chaussées, Paris (cit. on p. 26).

Scordelis, A. C. (1984). "Computer models for nonlinear analysis of reinforced and prestressed concrete structures". In: *PCI JOURNAL* 29.6, pp. 116–135 (cit. on p. 31).

Shet, C. and N. Chandra (2002). "Analysis of energy balance when using cohesive zone models to simulate fracture processes". In: *J. Eng. Mater. Technol.* 124.4, pp. 440–450 (cit. on pp. 37–39).

Simo, J. C. and T. J. Hughes (2006). *Computational inelasticity*. Vol. 7. Springer Science & Business Media (cit. on p. 94).

Spacone, E., F. C. Filippou, and F. F. Taucer (1996a). "Fibre beam–column model for non-linear analysis of R/C frames: Part I. Formulation". In: *Earthquake Engineering & Structural Dynamics* 25.7, pp. 711–725 (cit. on p. 31).

Spacone, E., F. C. Filippou, and F. F. Taucer (1996b). "Fibre beam–column model for non-linear analysis of R/C frames: part II. Applications". In: *Earthquake engineering & structural dynamics* 25.7, pp. 727–742 (cit. on p. 31).

Strömberg, L. and M. Ristinmaa (1996). "FE-formulation of a nonlocal plasticity theory". In: *Computer methods in applied mechanics and engineering* 136.1-2, pp. 127–144 (cit. on p. 34).

Sturm, J. F. (1999). "Using SeDuMi 1.02, a MATLAB toolbox for optimization over symmetric cones". In: *Optimization Methods and Software* 11.1-4, pp. 625–653 (cit. on p. 68).

Suryasentana, S., H. Burd, B. Byrne, and A. Shonberg (2019). "A systematic framework for formulating convex failure envelopes in multiple loading dimensions". In: *Géotechnique* 70.4 (cit. on pp. 68, 69).

Tajiri, S., H. Shiohara, and F. Kusuhara (2006). "A new macroelement of reinforced concrete beam column joint for elasto-plastic plane frame analysis". In: *Proc. 8th. national conf. earthquake engineering*. Citeseer (cit. on p. 84).

Terrien, M. (1980). “Emission acoustique et" comportement mecanique post-critique" d’un beton sollicite en traction”. In: *BULL LIAISON LAB PONTS CHAUSS* 105 (cit. on p. 14).

Tresca, H. (1864). “Memoire sur l’écoulement des solides à de forte pressions”. In: *Acad. Sci. Paris* 2.1, p. 59 (cit. on p. 19).

Tvergaard, V. (1990). “Effect of fibre debonding in a whisker-reinforced metal”. In: *Materials science and engineering: A* 125.2, pp. 203–213 (cit. on p. 39).

Tvergaard, V. and J. W. Hutchinson (1992). “The relation between crack growth resistance and fracture process parameters in elastic-plastic solids”. In: *Journal of the Mechanics and Physics of Solids* 40.6, pp. 1377–1397 (cit. on p. 39).

Tvergaard, V. and J. W. Hutchinson (1993). “The influence of plasticity on mixed mode interface toughness”. In: *Journal of the Mechanics and Physics of Solids* 41.6, pp. 1119–1135 (cit. on p. 37).

Vecchio, F. J. and M. P. Collins (1986). “The modified compression-field theory for reinforced concrete elements subjected to shear.” In: *ACI J.* 83.2, pp. 219–231 (cit. on p. 27).

Vecchio, F. J. and M. P. Collins (1988). “Predicting the response of reinforced concrete beams subjected to shear using modified compression field theory”. In: *ACI Structural Journal* 85.3, pp. 258–268 (cit. on p. 27).

Vecchio, F. J. and M. B. Emara (1992). “Shear deformations in reinforced concrete frames”. In: *ACI Structural journal* 89.1, pp. 46–56 (cit. on pp. 138, 139).

Wästlund, G. (1937). *New evidence regarding the basic strength properties of concrete*. JPRS (cit. on p. 14).

Wells, G. N. and L. Sluys (2001). “A new method for modelling cohesive cracks using finite elements”. In: *International Journal for numerical methods in engineering* 50.12, pp. 2667–2682 (cit. on p. 36).

Wells, G. and L. Sluys (2000). “Application of embedded discontinuities for softening solids”. In: *Engineering fracture mechanics* 65.2-3, pp. 263–281 (cit. on p. 36).

Xu, S.-Y. and J. Zhang (2011). “Hysteretic shear–flexure interaction model of reinforced concrete columns for seismic response assessment of bridges”. In: *Earthquake Engineering & Structural Dynamics* 40.3, pp. 315–337 (cit. on p. 25).

Xu, X.-P. and A. Needleman (1993). “Void nucleation by inclusion debonding in a crystal matrix”. In: *Modelling and Simulation in Materials Science and engineering* 1.2, p. 111 (cit. on p. 39).

Xu, X.-P. and A. Needleman (1994). “Numerical simulations of fast crack growth in brittle solids”. In: *Journal of the Mechanics and Physics of Solids* 42.9, pp. 1397–1434 (cit. on p. 37).

Titre : Nouveau macroélément pour l'évaluation de la vulnérabilité des bâtiments en béton armé de type poteaux-poutres soumis à des chargements dynamiques sévères

Mot clés : Béton armé ; FEM ; Diagrammes d'interaction ; Poutre Timoshenko ; E-FEM ; Discontinuité forte.

Résumé : Cette thèse est réalisée en collaboration avec Ecole Centrale de Nantes et GroupeESSOR (*thèse CIFRE*). L'objectif principal est de développer un outil simplifié, basé sur le concept du macroélément, la théorie des poutres et la Méthode des Eléments Finis Intégrés (E-FEM), pour étudier numériquement la vulnérabilité des structures en Béton Armé (BA) de type poteaux-poutres soumises à des chargements dynamiques sévères et leur comportement jusqu'à la rupture. Un modèle aux éléments finis en 3D est d'abord établi et des lois de comportement appropriées sont adoptées. Des simulations numériques sont effectuées, en considérant plusieurs combinaisons de chargement en 3D en termes de force axiale, force du cisaillement et moment fléchissant, afin d'identifier des états caractéristiques de la réponse de la section de la poutre. Des diagrammes d'interaction en 3D pour des sections carrées en BA avec des armatures positionnées symétriquement sont obtenus et un modèle de comportement simplifié en forces généralisées est implémenté dans un élément fini poutre Timoshenko. Le comportement adoucissant jusqu'à la rupture est finalement reproduit par le couplage du modèle continu généralisé à un modèle cohésif, qui décrit la réponse en termes de force généralisée-saut de déplacement généralisé, avec l'E-FEM. Des comparaisons aux résultats expérimentaux démontrent la performance de nouveau macroélément, qui en étant simple d'utilisation et rapide, est approprié pour des applications d'ingénierie.

Title: A novel macroelement to assess the vulnerability of reinforced concrete frame structures under severe dynamic loadings

Keywords: Reinforced concrete; FEM; Interaction diagrams; Timoshenko beam; E-FEM; Strong Discontinuity.

Abstract: This thesis has been carried out in collaboration with Ecole Centrale Nantes and GroupeESSOR (*thèse CIFRE*). The main objective is to develop a simplified tool, based on the macroelement concept, beam theory and the Embedded Finite Element Method (E-FEM), to numerically study the vulnerability of Reinforced Concrete (RC) frame structures subjected to severe dynamic loads and their behavior till failure. A 3D finite element model of a RC structural element is first built and suitable constitutive laws are adopted. Numerical simulations, considering various 3D loading combinations of axial, shear and flexural loads, are carried out to identify characteristic states of the beam sectional response. 3D interaction diagrams for symmetrically reinforced concrete square sections with various reinforcement ratios are obtained and a simplified stress-resultant constitutive model is implemented in a Timoshenko beam finite element. The softening behavior till failure is finally reproduced by coupling the continuous stress-resultant model to a cohesive model, which describes the response in terms of generalized force-generalized displacement jumps, within E-FEM. Comparisons with experimental results show the performance of the novel macroelement that being simple and computationally fast is suitable for engineering design purposes.